

THE USE OF INTERMEDIATE ASSAYS TO PROPEL LEAD COMPOUNDS INTO
CLINICAL TRIALS

A Dissertation

by

THOMAS C. SNAVELY

Submitted to the Graduate and Professional School of
Texas A&M University
in partial fulfillment of the requirements for the degree of

DOCTOR OF PHILOSOPHY

Chair of Committee,	A. Joshua Wand
Committee Members,	Thomas Meek
	Geoffrey Kapler
	Michael Polymenis
Head of Department,	A. Joshua Wand

December 2021

Major Subject: Biochemistry

Copyright 2021 Thomas C. Snavely

ABSTRACT

Technology is continually improved to overcome particular obstacles and then often proves useful in an array of applications. Biological understanding of both human physiology and the disease of interest allows for new approaches to be developed. In the case of *Mycobacterium tuberculosis* (*Mtb*), the pathogen has become extremely drug resistant, requiring new therapies, combination therapies, that are targeted at newly discovered vulnerabilities. Cancer, a leading cause of death, requires sophisticated therapies that are based on a better understanding of the biology behind such a diverse disease. Cancers that are inherently resistant to standard therapies, and those that result in relapse, require new treatment options to provide patients with a better chance of survival and improved quality of life. Other hereditary diseases, such as Menkes disease, are rare but result in an extremely poor quality of life as well as early death and have no effective therapy.

Genetic and physiological characterization, as well as subsequent target protein examination when applicable, provide insight into possible approaches for effective therapy. Advancements in treating other diseases, or failures in the case of Menkes, often provide useful information applicable to other diseases as well. As new reporter systems are developed for characterization or disease therapy, they also may provide the information necessary to overcome hurdles experienced when working with other, even completely different diseases.

Any particular assay or therapy will have limitations in throughput and information gained. As assays get more complex, the throughput decreases proportionally. In this text are three examples employing a base understanding of disease vulnerabilities, along with modern investigative tools to develop an efficacy assay that will provide evidence that a particular therapy warrants further development or that future research should focus on alternative therapies. This work focuses on developing and employing assays that maximize throughput to minimize the chance that limited resources will prevent an effective therapy from progressing into clinical trials.

DEDICATION

This dissertation is dedicated to my friends and family who helped encourage me to succeed in furthering my education after separating from the United States Navy.

ACKNOWLEDGEMENTS

I would like to thank my current committee as well as my mentors at Texas A&M, specifically, Dr. Larry Dangott, Dr. Vishal Gohil, Dr. Andres Holzenburg, Dr. Craig Kaplan, Dr. Paul Lindahl, Dr. Kim Loesch, Dr. James Sacchetti, Dr. James Smith, Dr. Deeann Wallis, and Dr. Robert Watson. I would also like to thank the technicians who have worked with me, specifically Andres Silva.

CONTRIBUTORS AND FUNDING SOURCES

Contributors: A. Joshua Wand, Michael Polymenis, Thomas Meek, and Geoffrey Kapler. For collaboration on the Menkes mouse experiments: Dr. Liam Guthrie and Andres Silva. For design and performance of the non-murine model experiments: Vishal Gohil, Shivatheja Soma, and Mohammad Zulkiflli. Greg Robertson at Colorado State University provided the *Mtb* infected mouse data. All other work conducted for the dissertation was completed by Thomas C. Snaveley independently.

Funding: All funding for the projects in this dissertation was provided by the laboratory of Dr. James Sacchettini.

NOMENCLATURE

ABSL	Animal Biosafety Level
AhR	Aryl Hydrocarbon Receptor
AREs	Antioxidant Response Elements
ATCC	American Type Culture Collection
BSL	Biosafety Level
C.F.U.	Colony Forming Units
CCCP	Carbonyl Cyanide 3-Chlorophenylhydrazone
CcO	Cytochrome C Oxidase
CHOP	Cyclophosphamide, Doxorubicin, Vincristine, and Prednisone
CROs	Contract Research Organizations
Cu	Copper
EMB	Ethambutol
ES	Elesclomol
FDA	Food and Drug Administration
FT	Fractionated Therapy
GFP	Green Fluorescent Protein
GoI	Gene of Interest
gy	Gray - A unit of radiation energy exposure.
HDF	Human Dermal Fibroblasts
HIV	Human Immunodeficiency Virus
HTS	High-Throughput Screening

IC ₅₀	Inhibitory Concentration to Cause 50% Inhibition
ICP	Inductively Coupled Plasma
INZ	Isoniazid
Keap1	Kelch-Like ECH-Associated Protein 1
KO	Knockout
LC-MS	Liquid chromatography–mass spectrometry
LoF	Loss of Function
MDR	Multi-Drug Resistant
mo-br	mottled-brindled
MoA	Mechanism of Action
MOI	Multiplicity of Infection
Mtb	Mycobacterium tuberculosis
N	Neutons
NIH	National Institutes of Health
NPP	Methyl 3-(4-Nitrophenyl) Propiolate
Nrf2	Nuclear Factor Erythroid 2-Related Factor 2
NSCLC	Non-Small Cell Lung Cancer
OADC	Oleic Acid, Albumin, Dextrose, and Catalase
OCR	Oxygen Consumption Rate
OD	Optical Density
Pan	Pantothenate
Penn/Strep	Penicillin and Streptomycin

PLA	Polyacetic Acid
PMA	Phorbol 12-Myristate 13-Acetate
RBT	Rifabutin
RD1	Region of Difference 1
ROS	Reactive Oxygen Species
RPM	Rotations Per Minute
RT	Radiation Therapy
SAR	Structure Activity Relationship
siRNA	Short Interfering RNAs
SIV	Simian Immunodeficiency Virus
SQ	Subcutaneous
Tet	Tetracycline
TnSeq	Transposon Insertion Sequencing
UPR	Unfolded Protein Response
WT	Wild-Type
x g	Times Gravity
XDR	Extremely Drug Resistant

TABLE OF CONTENTS

	Page
ABSTRACT	ii
DEDICATION	iv
ACKNOWLEDGEMENTS	v
CONTRIBUTORS AND FUNDING SOURCES	vi
NOMENCLATURE	vii
TABLE OF CONTENTS	x
LIST OF FIGURES	xiv
LIST OF TABLES	xvi
CHAPTER I INTRODUCTION	1
Developing New Models by Utilizing Technological Advances	1
Model Complexity Often Models Disease Complexity	2
Using Cell Culture as a Model for Systemic Disease	3
Infected Cell Models of Pathogenic Diseases	4
Systemic Disease Requiring Systemic Modeling	6
Choosing the Best Model	8
REFERENCES	10
CHAPTER II TREATMENT OF RADIATION RESISTANT CANCERS WITH NOVEL RIFAMYCIN COMBINATION THERAPY	12
INTRODUCTION	12
Development of Drug Resistant Cancer: A Public Health Concern	12
Need for New Chemotherapies and Combination Therapies	13
Rifabutin as a Starting Point	15
Role of Antioxidant Response Elements	18
A Diverse Panel of Cell Lines to Characterize RTI-79	19
Synergy	20
Radiation Therapy for Cancer	21
Fractionated Dose Therapy	22

Hypothesis.....	23
MATERIALS AND METHODS.....	23
Cancer Cell Lines.....	23
Reagents.....	24
qRT-PCR of AREs.....	24
Radiation Therapy Treatment.....	25
RESULTS.....	26
DISCUSSION.....	29
REFERENCES.....	32
CHAPTER III ELESCLOMOL ALLEVIATES MENKES PATHOLOGY AND MORTALITY IN A MOUSE MODEL BY ESCORTING CU TO CUPROENZYMES IN CELLS.....	48
ABSTRACT.....	48
INTRODUCTION.....	49
Effective Copper Transportation is Vital for Viable Nervous System Development.....	49
MATERIALS AND METHODS.....	52
Reagents.....	52
Synthesis of elesclomol-Cu ²⁺ Complex.....	52
Synthesis of copper histidine complex.....	53
In vivo pharmacokinetics and toxicological assessment of elesclomol & elesclomol-Cu ²⁺	53
Brain elesclomol-Cu ²⁺ exposure.....	55
LC-MS quantification of elesclomol & elesclomol-Cu ²⁺ in plasma and brain.....	55
Cardiac CTR1 knockout mice.....	57
Mottled-brindled mice.....	57
Administration of elesclomol to cardiac Ctr1 knockout mice.....	58
Administration of elesclomol, elesclomol-Cu ²⁺ , and copper histidine to mo-br mice.....	59
Locomotor function.....	61
Biochemistry.....	64
ATP7A knockout B16 melanoma cells.....	65
Statistical analysis and software.....	67
RESULTS.....	67
ES restores mitochondrial function in Ctr1 Knockout H9c2 Cells and Mice.....	67
ES Alone Does Not Rescue Mottled-Brindled Mice.....	69
ES-Cu ²⁺ Complex Rescues mottled-brindled Mice.....	69
Neuromotor Assessment of ES-Cu ²⁺ Rescue.....	71
Brain Histology and Biochemical Markers of ES-Cu ²⁺ Therapy.....	72
Identification of elesclomol as a potential therapeutic agent.....	73
Chemical properties and mechanism.....	74

Tolerability and pharmacokinetics of elesclomol	75
Tolerability and pharmacokinetics of elesclomol-Cu ²⁺ complex	75
ES restores mitochondrial function in Ctr1 Knockout H9c2 Cells and Mice	76
ES Alone Does Not Rescue Mottled-Brindled Mice	78
ES- Cu ²⁺ Complex Rescues mottled-brindled Mice	79
Neuromotor Assessment of ES-Cu ²⁺ Rescue	80
Brain Histology and Biochemical Markers of ES-Cu ²⁺ Therapy	81
DISCUSSION	82
Significance in Treating Human Disease and Impending Effective Menkes Therapy	84
ACKNOWLEDGMENTS	86
REFERENCES	88
CHAPTER IV TESTING OF NOVEL COMPOUNDS AGAINST MYCOBACTERIUM TUBERCULOSIS INFECTED	126
INTRODUCTION	126
Treating Tuberculosis Infection	126
Tuberculosis Biosafety Level	127
Methods to determine Anti-Tubercular Efficacy	130
Luciferase Assays Using Auto-luminescence	133
Improving Mtb High-Throughput Screening from Semi-Quantitative to Quantitative	135
Cytostatic vs Cytotoxic	135
The Benefit of Intracellular Screens Prior to Animal Studies	138
MATERIALS AND METHODS	138
Generating the Luciferase Tuberculosis Strain (mc ² 7000-Lux)	138
THP-1 Drug Efficacy Assay (mCherry and Lux)	139
Reagents	141
Z'-Factor Calculation	142
RESULTS	143
Legacy Fluorescence Based High-Throughput Screening	143
Real-Time Metabolism Reporting Using Luminescence	144
Time Versus Precision	146
The Necessity of Intermediate Assays	147
DISCUSSION	148
REFERENCES	151
CHAPTER V CONCLUSIONS	165
Using the Appropriate Model to Determine Efficacy in Combination Cancer Therapies	165
Advancing Drug Discovery to Mammalian Models	167
Using Tissue Culture as a Surrogate for Animal Infection Models	168

In Conclusion	169
---------------------	-----

LIST OF FIGURES

	Page
Figure II-1: RTI-79 Structure.....	39
Figure II-2: HDF - RT in Combination with RTI-79.....	40
Figure II-3: MCF-7 RT in Combination with RTI-79	41
Figure II-4: A549 RT in Combination with RTI-79	43
Figure II-5: RTI-79 Dose Response.....	44
Figure II-6: DU-145 RT in Combination with RTI-79.....	45
Figure II-7: PC-3 RT in Combination with RTI-79.....	46
Figure II-8: Fractionated Radiation Therapy in Combination with RTI-79.	47
Figure III-1: Effects of ES treatment in cardiac <i>Ctrl</i> KO mice.....	93
Figure III-2: Effects of ES-Cu ²⁺ treatment in <i>mo-br</i> mice.	95
Figure III-3: Neuromotor tests of 10 week old mice.	97
Figure III-4: Neuropathology of 2 and 10 week old mice.	98
Figure III-5: ES-Cu ²⁺ rescues biochemical phenotypes in 2 and 10 week old <i>mo-br</i> <i>mice</i>	99
Figure III-6 (S1): Effects of ES treatment on OCR and relative ATP levels in <i>Ctrl</i> KO H9c2 cardiac cells.....	102
Figure III-7 (S2): ES 0.5% Methocel™ pharmacokinetics (PK).....	103
Figure III-8 (S3): Effects of ES treatment in cardiac <i>Ctrl</i> KO mice.	104
Figure III-9 (S4): Effects of ES treatment on SOD1 levels in cardiac <i>Ctrl</i> KO mice.	106
Figure III-10 (S5): Brain ES exposure.....	107
Figure III-11 (S6): Captisol® ES-Cu ²⁺ phase solubility.....	108
Figure III-12 (S7): ES-Cu ²⁺ 20% Captisol® pharmacokinetics (PK).....	109

Figure III-13 (S8): Effects of ES-Cu ²⁺ treatment in <i>mo-br</i> mice.	110
Figure III-14 (S9): Histological examination of 2 and 10 week livers.	112
Figure III-15 (S10): Additional neuropathology in 2 week old mice.	113
Figure III-16 (S11): Additional neuropathology in 10 week old mice.	115
Figure III-17 (S12): Heart biochemistry <i>mo-br</i> mice.	116
Figure III-18 (S13): Effects of ES treatment on SOD1 levels in <i>mo-br</i> mice.	118
Figure IV-1: Screen of Characterized Compounds with an mCherry Reporter.....	155
Figure IV-2: Comparing Reporter Cell Lines.....	156
Figure IV-3: Z' factor Analysis.	157
Figure IV-4: Luciferase Assay Validation.....	158
Figure IV-5: Mc ² -7000-Lux Intracellular Assay Variability.....	159
Figure IV-6: Optimizing Exposure Length.....	160
Figure IV-7: The Necessity of Intermediate Assays.....	161
Figure IV-8: Compound Series Evaluation.....	162
Figure IV-9: Murine Efficacy.	163
Figure IV-10: Using the Optimized Assay.	164

LIST OF TABLES

	Page
Table II-1: Prostate Cancer mRNA Levels	38
Table II-2: A549 qRT-PCR.	42
Table III-1: Treatment Regime and 10 week survival in the <i>mottled-brindled</i> mouse.	101
Table III-2 (S1): Elesclomol tolerability in adult C57BL/6 females.	119
Table III-3 (S2): Elesclomol tolerability in adult C57BL/6 females.	120
Table III-4 (S3): CBC of 10 week old C57BL/6 and <i>mo-br</i> mice.	121
Table III-5 (S4): Serum chemistries of 10 week old C57BL/6 and <i>mo-br</i> mice.	122
Table III-6 (S5): Gait parameters at 10 week assessment in WT and <i>mo-br</i> males. .	123
Table III-7 (S6): Body, brain, and heart weights at 2 & 10 week necropsy.	124
Table III-8 (S7): Thymus, lungs, kidney, liver, and spleen weights at 2 & 10 week necropsy	125

CHAPTER I

INTRODUCTION

Developing New Models by Utilizing Technological Advances

Technology, specifically medical and scientific tools, is advancing quickly and removes many barriers to research, our ability to treat human disease is primarily limited by our creativity. Advancements in spectroscopy, genomic sequencing, and reagents have all made deep biological discovery widely available. Fundamental capabilities including cheap and accurate custom DNA strand synthesis (primers), extensive DNA and RNA sequencing, protein structure determination, small interfering RNA (siRNA) production, restriction enzymes and polymerases, genetic cloning, and bacterial expression, have all made research that wasn't possible, or was extremely low throughput, commonplace.

Now that enzyme manipulation and sequencing information are used, or are a foundation for daily laboratory research, scientists have the ability to more completely understand the enzyme, pathogen, or genetic aspect that their research focuses on. Current technological advancements mainly fall into 2 categories: enhancing throughput using new approaches and automation as well as significantly increasing the breadth of information collected.

Throughput can be increased by using an auto sampler or multiple plate incubation and loading systems as well as decreasing reaction size and volumes. Enzyme reactions and cellular assays can be conducted on a substantially smaller scale. Both liquid handling systems and plate readers have increased capability with 96-well plates being standard,

then 384-well plates, and now 1536-well plates, facilitating a 16-fold increase in the number of samples possible from the same size plate. While pooling samples is not a new technique, samples involving sequencing as part of the data collection process can be barcoded to allow pooling of essentially an unlimited number of samples. Automation includes using liquid handling systems such as CyBio Vario, Integra Voyager, Eppendorf Epmotion, and Formulatrix Mantis tipless pipetting robots that take the place of manual pipetting.

The breadth of information collected is amplified by cost effective deep sequencing when DNA or RNA is involved. Current techniques such as Transposon Insertion Sequencing (TnSeq), are able to differentiate between mutations or inhibition in different parts of a protein's code [1-4]. Mass spectroscopy can be used to identify protein levels and metabolites. Fluorescent reporters can provide temporal tracking, levels, and locations of the reporter's target. Advancements in flow cytometry allow the examination of multiple factors, limited only by the fluorescence reporters used, and analyzed for individual cells as opposed to a bulk readout. This provides a more informative range of responses at the cellular level that doesn't suffer from the pitfalls of averaging bulk readouts that assumes all cells are responding similarly.

Model Complexity Often Models Disease Complexity

The simplest model capable of assessing the important aspects of a particular disease, is generally the best to use to identify treatments worthy of advancing towards human clinical trials. Time to results and cost are two major factors influencing many

experimental decisions. A genetic disease, such as cancer, may be reproduced by culturing a biopsy and is the most commonly used approach for testing new cancer therapies prior to moving onto animal models. Other diseases such as Tuberculosis benefits from, and Menkes disease requires, more complex models.

Sometimes, as with Menkes disease, the disease can be replicated through genetic manipulation. This include yeast knockout (KO) strains, and modified human cell lines. Genetic modification can be to cells in culture, or to an embryo for in vivo modeling, mice in the case of Menkes. Ironically, predicting efficacy for an extremely complex cancer can often be conducted in culture, while a disease caused by a single mutation, such as Menkes, requires in vivo modeling to determine if systemic Cu^{2+} transport has been restored to homeostasis. In vivo modeling examines the visible phenotype being restored to normal presentation and lifespan being extended significantly, if not all the way to normal length. Considerations for determining the most appropriate disease model for testing novel therapies is described below.

Using Cell Culture as a Model for Systemic Disease

With human cancer, a particular compound will be administered in a way, or prepared in such a way (e.g. liposomes/Doxil) that the cancerous cells will be exposed to the drug, ideally targeted over healthy cells. An in vivo model will be used to characterize the metabolism of the molecule and its safety profile. As far as a particular type of cancer, different therapies and biological characterization can be performed on cultured cells. While development and treatment of human cancer therapies will ultimately lead to testing

in an animal model, be it murine, canine, or otherwise, a compound series can be tested and structure activity relationship (SAR) can be performed with tissue culture. Some SAR is conducted using an identified protein target in vitro.

The majority of cancer therapy development can be conducted on cultured cells. Much of the biological response to cancer's genetic mutations is contained within the cell and doesn't require a systemic model. These statements apply to traditional chemotherapy. Newer immunotherapy strategies require the ability to look at the response of the particular cancer, but also the host immune response between multiple type of cells and must be studied together, requiring a systemic model [5]. Models of co-culturing multiple cell types are possible, but depend on the disease being tested to determine the extent that the model resembles natural systemic response[6].

An important aspect necessary for more complete context, is that more complex diseases can sometimes be tested and treated in simple models. Alzheimer's disease results in misfolding forming plaques on neurons and hindering mental fitness[7]. Despite the fact that the disease presents as extracellular plaques on neurons, yeast genes necessary to combat plaque formation allow modeling human Alzheimer's disease plaque formation intracellularly in yeast [5].

Infected Cell Models of Pathogenic Diseases

Some types of diseases, particularly those that involve a pathogen, be it a virus, protozoans, or bacteria, will require a more complex model, earlier in the drug development process. Currently, work on an inhibitor for a COVID-19 protein can be

conducted in a relaxed biosafety environment, and once sufficient binding and inhibition is exhibited against the protein, the best compounds are tested against a human cell infection model in a higher containment environment. The same goes for Mycobacterium tuberculosis (*Mtb*) research.

Assuming that a protein target is identified early on, either through an essentiality screen (e.g. TnSeq)[3] or through fragment screening, the screening will go through 3 or 4 distinct stages. First, a compound series will be screened against a target protein using a binding determination. The compounds showing the best potential are then tested against *Mtb* in liquid culture or on agar plates. This allows for highly specific testing under a very controlled set of conditions including growth media (e.g. carbon source effects). This type of assay can be used to perform SAR studies to modify the compound for increased stability and efficacy.

The molecules showing the best potential will then be tested in an infection model. As I will show later on in this text, testing against human cells infected with *Mtb* is both timely and financially beneficial to getting a new drug into clinical trials. Increasing the number of compounds that can be screened, decreasing the time to results, and being able to differentiate between analogs in a compound series all lower cost and time required to select a lead compound.

Human cells infected with *Mtb* represent the *in vivo* population of *Mtb* not contained in tubercles. Although efficacy in this model doesn't guarantee *in vivo* efficacy, a lack of efficacy in this intracellular screen makes it highly unlikely that the compound of interest will show efficacy *in vivo*. Ultimately, if the compound continues to show

efficacy and a high therapeutic window, the concentration required for efficacy being significantly below toxic doses, through increasingly complex models, it will end up being tested on one or more animal models for safety and efficacy prior to human clinical trials.

A pathogen will require an infection model earlier on if developing a new therapy. In a scenario where a drug is being repurposed, impacts on the drug on human cells is likely already characterized. A novel compound passing through the cytosol of human cells to kill the intracellular bacteria will need to be tested for impact from drug pumps, either pumping drugs out or pumping drugs in, creating high intracellular concentrations[8]. It may also be that human cells metabolize the new drug into an inactive molecule before it can work on inhibiting the pathogen. Tuberculosis specifically, has a further level of complication called caseum. Instead of tuberculosis being either intracellular or systemically free floating, it also forms granulomas of dead macrophage shells and other white blood cells with viable *Mtb* on the inside [9]. In the same way that nutrients are cut-off inside caseum, many drugs lack clearance as well, due to limited vascularization [9].

Systemic Disease Requiring Systemic Modeling

Menkes disease is a copper transport disease resulting from a mutation in the gene *ATP7A*. *ATP7A* is a copper transporting protein that exports copper from the cytosol into systemic circulation. The fact that Menkes disease can be modeled by a mutation of *ATP7A* in a murine model does not indicate that the same mutation in a murine cell line will replicate the disease because Menkes is tissue specific. Being tissue specific in and of

itself doesn't necessarily preclude cellular models from being informative models. In the case of Menkes, Cu^{2+} is sequestered in the gastrointestinal tract, but needs to be trafficked to those parts of the system that are Cu^{2+} deficient, with penetration of the blood brain barrier being critical.

Phenotypes typical of Menkes, such as gray kinky hairs and abnormal coat coloring, cannot be observed using just tissue culture. Despite tissue culture being useful for looking at a compound's ability to cross membranes, a systemic model is necessary to show that the Cu^{2+} transporting molecule will compensate for Cu^{2+} sequestered in the intestines, and restore copper homeostasis in deficient tissues as opposed to increasing Cu^{2+} in circulation but not intracellularly. The carrier molecule must have sufficient Cu^{2+} binding to carry it to the appropriate tissue but not so strong as to prevent release into deficient tissue.

Menkes, in contrast to cancer, with both being genetic diseases, is hereditary while cancer is developed *de novo*. These 2 diseases require very different experimental approaches. Menkes mechanism of action (MoA) is to sequester copper brought in through digestion in the intestines and prevent distribution systemically. This leads to the visible phenotypes as well as a lifespan of two weeks. Even though the cause of Menkes, mutated *ATP7A*, is known, the proposed treatment functions by bypassing the body's normal transport and homeostasis. This abstract approach, creating a novel Cu^{2+} transport system, must be tested *in vivo* to determine efficacy. When treating cancer, the treatment is dealing directly with cells and their individual biology as opposed to Menkes having systemic distribution problems.

Choosing the Best Model

The three diseases examined described below include genetic, acquired and hereditary diseases, as well as a pathogenic disease. They exhibit the range of model complexity necessary once a general therapy or compound series has been identified using binding studies, enzyme assays or other *in vitro* characterization. There is rarely an ideal model for any disease, especially as a new therapy is being developed. Ethically and financially, experiments using live animals should be limited as much as possible[10]. Time is money and an animal study takes more of both compared to precursor, non-*in vivo* experiments[10]. An intracellular *Mtb* model will take less than a week to generate efficacy data, while a murine infection will take months to acquire data. Menkes has the important metric of lifespan, therefore final data will take over a year to determine the full extent on prolongation of lifespan despite success being realized every day after 14 days that an affected male mouse lives.

Although not used as often, higher order species research should be avoided if at all possible[11]. If an experiment can be conducted on zebrafish, it would be unethical to use a Rhesus Macaque monkey instead[11]. With a disease such as Menkes, a systemic model is required for efficacy testing. With a pathogen such as TB, when the target is known, research can use a series of model escalations as development progresses; protein, to pathogen, to human cells infected with the pathogen and human cell safety profiling, to animal models, to human clinical trials.

An additional layer of complexity regarding ethical treatment is found in the selection of affected animals to be used[10]. In some cases, such as with Menkes, that the lifespan is too short and the natural occurrence is too low, therefore, those mice must be grown in a colony to provide pups for efficacy testing. Chickens spontaneously develop ovarian cancer in 35% of a cohort as they age [12]. Dogs can be recruited that have developed Duchenne muscular dystrophy naturally instead of intentionally breeding them to limiting euthanizing dogs that could have otherwise been useful for finding a cure [13]. Testing novel combination therapies for cancer can be tested on naturally occurring canine cases.

REFERENCES

1. Rock, J.M., et al., *Programmable transcriptional repression in mycobacteria using an orthogonal CRISPR interference platform*. Nature Microbiology, 2017. **2**(4): p. 16274.
2. Lau, C.-H. and Y. Suh, *In vivo genome editing in animals using AAV-CRISPR system: applications to translational research of human disease*. F1000Research, 2017. **6**: p. 2153-2153.
3. Griffin, J.E., et al., *High-resolution phenotypic profiling defines genes essential for mycobacterial growth and cholesterol catabolism*. PLoS Pathog, 2011. **7**(9): p. e1002251.
4. Zhang, Y.J., et al., *Global assessment of genomic regions required for growth in Mycobacterium tuberculosis*. PLoS Pathog, 2012. **8**(9): p. e1002946.
5. Rescigno, M., F. Avogadri, and G. Curigliano, *Challenges and prospects of immunotherapy as cancer treatment*. Biochimica et Biophysica Acta (BBA) - Reviews on Cancer, 2007. **1776**(1): p. 108-123.
6. Brown, J.L., et al., *Biofilm-stimulated epithelium modulates the inflammatory responses in co-cultured immune cells*. Scientific reports, 2019. **9**(1): p. 1-14.
7. Drachman, D.A., *The amyloid hypothesis, time to move on: Amyloid is the downstream result, not cause, of Alzheimer's disease*. Alzheimer's & Dementia, 2014. **10**(3): p. 372-380.

8. El-Banna, T., et al., *Modulation of antibiotic efficacy against Klebsiella pneumoniae by antihistaminic drugs*. J Med Microb Diagn, 2016. **5**(225): p. 2161-0703.10002.
9. Sarathy, J.P., et al., *Prediction of Drug Penetration in Tuberculosis Lesions*. ACS Infectious Diseases, 2016. **2**(8): p. 552-563.
10. Freires, I.A., et al., *Alternative animal and non-animal models for drug discovery and development: bonus or burden?* Pharmaceutical research, 2017. **34**(4): p. 681-686.
11. Neuhaus, C.P., *Ethical issues when modelling brain disorders in non-human primates*. Journal of Medical Ethics, 2018. **44**(5): p. 323-327.
12. Hawkrige, A.M., *The chicken model of spontaneous ovarian cancer*. PROTEOMICS–Clinical Applications, 2014. **8**(9-10): p. 689-699.
13. Kornegay, J.N., et al., *Canine models of Duchenne muscular dystrophy and their use in therapeutic strategies*. Mammalian Genome, 2012. **23**(1): p. 85-108.

CHAPTER II
TREATMENT OF RADIATION RESISTANT CANCERS WITH NOVEL
RIFAMYCIN COMBINATION THERAPY

INTRODUCTION

Development of Drug Resistant Cancer: A Public Health Concern

Cancer is the second leading cause of death in the United States [1]. Cancer contributes 12% of global mortality [2]. Dependent on the type of cancer, roughly half of cancers aren't detected until later stages [3]. Therapy for advanced cancers hasn't significantly improved in 2 decades [3]. Compared to the previous 3 years, cancer cases have gone down 20%-40% depending on type of cancer [4]. On the surface that seems positive, but unfortunately it is likely that due to COVID-19 less in-person healthcare and testing was conducted [4]. Ultimately this will lead to a significant increase in cases once a more normal medical system is in place after further combating COVID-19. Not only will there be a spike in detected cases, but due to the delay in diagnosis, the extent of disease progression will be higher than pre-2020 levels.

To the extent poor diagnosis rates of cancer during COVID-19 will translate to resistant cancers is yet to be seen. Seventy percent of cancer mortality in low or middle income countries is due to improper diagnosis or inadequate treatment [5]. This lowered health care quality status is comparable to the United States due to the impacts of COVID-19 on the healthcare system. An international review of over 200,000 patients found that those with both COVID-19 and cancer are 2.54 times more likely to die. Exacerbation

fluctuated between cancer types and showed no vulnerability to one type of therapy versus another[6]. Partial or incomplete treatment contributes to drug resistant cancer, which then leads to relapse if not death.

Issues of drug resistance are not communicable, and therefore have a different set of concerns than drug resistant pathogens. One example of resistance forming pathogens is Tuberculosis, where drug resistance has become so serious that there are multiple categories of resistance. With a cancer patient who is not sensitive to the standard of care, an alternative to palliative care is necessary. In the case of ovarian cancer, 70%-80% of treatment is ineffective the first time, and sadly the majority of patients have an incurable relapse [7].

For cancer patients, time and quality of life are two important factors. Untreated malignant cancer will continue to grow until it is not possible to be treated. Many patients have severe side effects from radiation therapy (RT) and chemotherapy so ineffective treatment works against both the patient's time and quality of life.

Need for New Chemotherapies and Combination Therapies

As cancer develops in the patient, cancerous cells will develop increasing amounts of genetic variation. In the same way that resistant bacteria survive treatment and then flourish when there is less "crowding" in the host after selection, a particular strain of cancer may respond similarly [8]. The major difference is that resistant bacteria can be passed to other individuals. Cancer develops *de novo* in a person and must also develop drug resistance *de novo*.

The fact that cancer develops *de novo* should not minimize the impact that genetic predisposition has on developing cancer and the ability to design therapies for it. There are currently 59 genes listed by the American College of Medical Genetics and Genomics as requiring medical intervention [9]. Genetic screening gives individuals the knowledge to minimize exposure to things that may exacerbate the likelihood of developing cancer. The individual can then also conduct frequent screening to catch cancer as early as possible. Due to the increased likelihood of developing that specific cancer, it warrants frequent monitoring for early detection, to providing early stage treatment and increased survival [3].

As noted above in regards to ovarian cancer, relapse is significant, and treatment of a relapse does not have favorable outcomes. Chemotherapy, RT, and resection (surgical removal) are the three major classes of cancer treatment. There is no one size fits all approach, and most cancer therapies have significant side effects. Effectively treating aggressive and drug resistant cancers will likely require multiple types of treatment. According to the National Institute of Health (NIH), while some people will only receive 1 type of treatment, most people will get 2 or more therapies[10]. A compound which selectively targets cancer cells during chemotherapy or RT, while reducing the dosage of the primary therapy required, will minimize harmful side effects and improve patient health versus only using the primary therapy at a higher concentration.

Chemotherapy, doxorubicin for this paper unless otherwise noted, is harmful systemically, but targeted therapies are reducing unintended exposure [2]. Modern targeted therapies currently fall into one of two classes. One class is the encapsulation of

a broad spectrum chemotherapeutic targeted to the site of the cancer cells, limiting exposure to healthy tissue [2]. The second class is synthetic compounds or antibodies that biologically block cancer proliferation cell cycles [2].

Only localized regions will be damaged with modern RT. About 50% of cancer patients will receive RT at some time during their treatment [11]. Both treatments have side effects but lowering the dosage will decrease harm to the patient. Whether the secondary, booster compound is acting in synergy with the standard of care, or just increasing reactive oxygen species (ROS) levels to a toxic level, both mechanisms of action are positive towards treating cancer while simultaneously minimizing damage to healthy cells. Reactive oxygen species, including super oxide which can form hydroxyl radicals and hydrogen peroxide, can then go on to interact with and damage proteins, lipids, and DNA they come into contact with, are formed as a byproduct of reduction of other molecules or by interaction of high energy radiation [12-14]. Doxorubicin, RT and, RTI-79 all generate ROS [14, 15]. The abnormal regulation of metabolism due to the Warburg effect, an increase in glycolysis despite a functional electron transport chain, further contributes to an inability of cancer cells to properly maintain homeostasis and respond to the elevated ROS found under cancerous growth conditions [15, 16].

Rifabutin as a Starting Point

RTI-79 is the product of a development process starting with rifabutin and modified by medicinal chemists in the Sacchetti Lab (Figure 1). At the beginning of this project, the goal was to identify a means for sensitizing drug resistant cancer. ROS have

been identified to cause death in cancerous cells [17]. With cancer being the number 2 cause of death [1] and resistant cancer being more lethal [3], stagnant therapy for decades validates that therapy for resistant cancers is out of date.

MYC is a cell cycle regulator associated with leukemia and lymphoma [18]. MYC mutations are found in 10-15% diffuse large B cell lymphoma (DLBCLs) [18]. Double Hit lymphomas have mutant *MYC* and *BCL2* and/or *BCL6* with very high resistance to their standard of care and have high relapse [18, 19].

After identifying resistant lymphoma as the target, development of a novel compound began. CHOP (cyclophosphamide, doxorubicin, vincristine, and prednisone) is the standard of care for lymphoma. CRL-2631 cells were used to screen CHOP in combination with almost 50,000 molecules including the NIH Clinical Collection. At this point, rifabutin was identified as synergistic with CHOP in CRL-2631 (Sacchettini Lab Data/Unpublished).

CRL-2631 was treated with rounds of dox exposure to create the resistant cell line G3 [20]. Rifabutin analogs were tested with dox against G3 cells and provided for the basis of SAR studies using medicinal chemistry. The development led to RTI-79, which when tested in a combination therapy with dox against G3 cells lowered the IC_{50} of dox by 7-fold (Sacchettini lab data/Unpublished).

RTI-79 has shown efficacy in a variety chemotherapy combinations (Sacchettini lab data, Unpublished). RTI-79 redox cycles to produce high levels of ROS in as little as 2 minutes in G3 cells, producing 12-fold increase in superoxide and doubling the hydrogen peroxide concentration ((Sacchettini Lab Data/Unpublished). This leads to several

impacts including unfolded protein response (UPR), ubiquitination of Nrf2 leading to degradation, and mitochondrial fission (Maxwell lab. Unpublished).

Five double- or triple- hit DLBCL cell lines (WSU-FSCCL, SU-DHL-6, SU-DHL10, OCI-Ly19, and SU-DHL-4) that were all resistant to CHOP, became sensitive in the presence of RTI-79 (Unpublished historical lab data). ROS can induce mutation in mitochondrial DNA [12]. With ROS upregulating the cell's antioxidant response, it can also trigger cell death [12]. Antioxidants are critical in managing tumor suppression and likewise, mutations in nuclear factor erythroid 2-related factor 2 (Nrf2) and kelch-like ECH-associated protein 1 (Keap1), with Nrf2, regulated by Keap1, regulating the cellular antioxidant response [12].

ROS can activate caspase mediated cell death in under an hour [12]. Monoclonal antibodies and enzyme inhibitors have been identified to cause elevated ROS which leads to apoptosis [12]. A similar impact was identified where chemotherapy and radiotherapy cause apoptosis through ROS production [12]. ROS, H_2O_2 specifically, can trigger autophagy [12]. As mentioned above, RTI-79 doubles H_2O_2 levels immediately in resistant B lymphoma. ROS additionally can cause necrosis or cell death through p53 [12].

Finally, in drug resistant cells with upregulated efflux pumps, a depletion of NADH to NAD inhibits ATP Synthase and produces more ROS [12]. Research using ROS to treat cancer is not novel. A relatively simple compound methyl 3-(4-nitrophenyl) propionate (NPP) shows preference for causing cancerous cells to go through apoptosis [21]. Sensitivity was observed on tumors with high basal ROS combined with a low capacity for additional ROS[21]. Mutations in p53 or intentional p53 knockdown, show

enhanced NPP sensitivity [21]. This study and type of molecule tested both support the hypothesis that RTI-79 has a significant impact through ROS generation.

Role of Antioxidant Response Elements

While cells normally produce ROS while making ATP via the electron transport chain, there are pathways in place to produce antioxidants to minimize damage to tissues. In cancer cell lines, antioxidants can be upregulated to handle ROS from RT or dox. For the identified resistant cancer cell lines, a therapy or combination therapy that is able to produce ROS and inhibit antioxidant response elements (AREs) should be able to push resistant cancer lines past any manageable stress levels and towards death [22].

When it comes to ARE upregulation, aryl hydrocarbon receptor (AhR) and Nrf2 are two of the main antioxidant response transcription factors [23]. Not only are Nrf2 and AhR important antioxidant transcription factors, but they also regulate each other [23]. AhR has been identified binding the Nrf2 promoter as well as siRNA inhibition of AhR resulting in Nrf2 downregulation [23]. Likewise it was also determined that Nrf2 binds to the promoter of AhR [24]. The cross talk between these two transcription factors helps facilitate effective cellular stress response to ROS.

Nrf2 is typically stored in the cytoplasm bound to Keap1 [25]. Keap1 releases Nrf2 under a variety of cellular stresses, but in this case it is ROS which triggers the release [25]. Nrf2 can then translocate into the nucleus and upregulate AREs, including AhR. Cytosolic AhR will be activated by one of its many ligands and then translocate into the nucleolus to upregulate AREs, including Nrf2 [24]. In prior work on this project, using

drug resistant ovarian cancer, western blot data showed that Nrf2 was degraded in the presence of 10uM RTI-79.

A Diverse Panel of Cell Lines to Characterize RTI-79

Prostate cancer is very common in males with 1.3 million new cases globally per year [26]. DU-145 and PC-3 are both commonly used prostate cancer lines with DU-145 having wild-type (WT) p53 [26]. On the other hand, PC-3 is p53 null [26]. Both cell lines are androgen insensitive [26]. Tumor suppression control is regulated intracellularly by p53 causing apoptosis in toxic stress situations [27]. DU-145 has historically exhibited resistance to RT with a 20gy dose only causing 45% reduction in viability [28]. PC-3 is much more radiation sensitive, roughly 10x, and 2gy causes 50% reduction in viability [29].

MCF-7 is human breast adenocarcinoma tissue. Breast cancer is often treated with a combination of RT and chemotherapy, or resection to help prevent high, 40%, relapse rates [30]. With 2gy and 4gy doses of RT lowering viability by 20% and 30% respectively [30]. MCF-7 isn't particularly resistant to any treatment, however, preventing relapse is a major concern and drives the use of diverse therapeutic combinations [30]. Combination chemotherapy and RT that induce ROS have shown inhibition of MCF-7 growth [31].

A549 is a non-small cell lung cancer (NSCLC). If cultured in a hypoxic state, A549 will upregulate SM22 α which increases resistance to chemotherapy and RT [13]. Contradictory research shows SM22 α as a tumor suppressor [13]. In a normally functioning cells, Keap1 retains Nrf2 in the cytoplasm and NSCLC lines are enriched for

Keap1 mutations [32]. Dysfunctional Keap1 allows Nrf2 to heavily upregulate AREs, and providing resistance to many therapies including RT [32]. Tumors that have Keap1 or Nrf2 mutations are likely to have relapse after RT [32]. Keap1 can ubiquitinate Nrf2 to tag it for degradation or release it to translocate into the nucleus [33]. Keap1 mutations are found in 19% of lung cancer and promote upregulation of AREs by Nrf2 [33]. Initially, this upregulation will provide a less toxic environment for the cancer to rapidly grow [33].

Human dermal fibroblasts (HDF) are from either adult or infant male foreskin, in this case infant. HDF are primary cells with a limited number of passages, but a normal biology, unlike cancerous cells of any issue type. HDF are used as a surrogate for healthy human tissue in experiments such as cytotoxicity studies prior to metabolic animal studies. In the case of RT, HDF are used to examine the predicted impacts of a particular treatment on the tumor's surrounding tissue. In the context of RT, HDF can be used to examine the impact of a novel combination therapy on healthy tissue.

Synergy

Synergy is generally defined as the outcome of two simultaneous treatments being greater than the sum of the individual treatments [34]. By being able to use a synergistic combination therapy, assuming of course that the side effects were not increased proportionally, the therapy can then use lower doses of the therapy to improve the outcome of the patient. Although high levels of synergy are ideal, the fact that RTI-79 is typically effective at treating cancer with levels non-toxic to healthy tissue allows its use even if efficacy can't be certain due to the plethora of cancers and our level of knowledge about

them. While there is a chance of no added improvement, RTI-79 will still be non-toxic to healthy tissue. There is likely a chance for additive effects if not synergistic effects in cancer cells.

RTI-79 is known to undergo oxidation and reduction cycling with NAD⁺ and NADH from the electron transport chain[12], similar to dox, and produce ROS while also causing temporary mitochondrial fissure (Sacchettini Lab Data Unpublished). In normal cells, the addition of ROS would lead to an upregulation of AREs, such as superoxide dismutase and glutathione reductase, by Nrf2 and AhR, but that response is confounded by the Warburg Effect in cancerous cells[12]. Individual cell lines will vary both in their basal ROS levels as well as their ability to upregulate AREs and manage the damage from RTI-79 and RT/chemotherapy.

ROS is only one part of the impact from these therapies. The reduced expression of genes ROS response pathways, AREs, limits the cell's ability to respond to ROS and exacerbates the impact. While talking about synergy it is important not to forget that there are thresholds independent of synergy[12]. ROS can be raised to a level so toxic that cells will not survive, and this may be accomplished with a combination that shows no synergy. Alternatively, when a drug that is non-toxic on its own is able to enhance another therapy, there is synergy.

Radiation Therapy for Cancer

The American Cancer Society recognizes the early 1900s as the time when radiation was discovered to be effective against tumors. RT has changed in recent years,

even if the radiation part stays the same, the advancement in other technologies allows them to be used with RT for great efficacy [35]. This includes immunotherapies and targeted delivery. Hundreds of thousands of people will receive RT each year and by maximizing our understanding of the cancer, better combination therapies can be developed and finely tuned doses of radiation can be used to minimize exposure and damage to surrounding healthy tissues.

The Linear Quadratic Model, or the α/β ratio, is used to determine the appropriate dosing to use [36]. Different cell lines will have different α/β ratios, which are determined experimentally[11]. Healthy cells will have a low ratio and be able to repair faster than cancerous cells [11]. If the ratio is high, the cells respond to lower doses with a more linear kill curve. If the ratio is low, the kill response is more of a sigmoidal curve with minimal death at low doses but a more drastic impact at higher doses. By capitalizing on the ability of healthy cells to handle small doses better than cancerous cells led to fractionated radiation therapy.

Fractionated Dose Therapy

Fractionated therapy (FT) breaks the RT up into frequent smaller doses. Healthy cells can repair DNA damage more from smaller doses than already stressed cancer cells can, making FT a feasible way to deliver RT with enhanced selectivity [37, 38]. Healthy cells have a low α/β ratio, determined experimentally[38]. A balance between fractionated doses and a single dose must be established as exposing cells, even to low power radiation, for long periods will lead to serious side effects [38]. Prostate cancer has been found to

have a low α/β ratio, indicating that prostate cancer should be particularly sensitive to FT while healthy tissue is not [39]. A retroactive study of thousands of patients with bone metastases who received RT found a significant improvement in outcome for those treated with FT [40]. A single fractionated dose typically needs to be greater than 5gy for fractionated dosing to make a difference [41].

Hypothesis

Cells experiencing an abnormal resistance to their standard of care can sometimes be treated by inhibition of antioxidant response elements (AREs) such as AhR and Nrf-2. Cell lines that do show ARE inhibition are likely to synergize with RTI-79 and their standard of care. Between synergy with RTI-79 and the use of a fractionated dosing regimen, cancers which may have not responded to RT, or require high levels of radiation exposure, can now be treated while maximizing safety to the patient and simultaneously effectively treating the tumor.

MATERIALS AND METHODS

Cancer Cell Lines

A pair consisting of DU-145 and PC-3 human prostate cancer lines was used as a clinically relevant model for cancer that would be typically treated with radiation therapy [42, 43]. DU-145 is resistant to both RTI-79 and RT. RTI-79 does not produce sensitivity in PC-3. Primary human dermal fibroblasts (HDF) were used to test treatment selectivity and provide a non-cancerous line for comparison. A549 lung epithelial tissue is insensitive

to RTI-79. MCF-7 breast cancer models a non-RTI-79 sensitive, but highly RT sensitive line. All cells were maintained in standard flasks at 37C with 5% CO₂. Cells were passed twice weekly with 0.5% trypsin.

Reagents

RPMI or DMEM media was used for tissue culture with 10% FBS and 100U penn/strep. RTI-79 is generated in-house. Doxorubicin is from Ava Chem.

Cells are cultured in sterile 75cm² or 175cm² flasks, passed using centrifugation at 1600 rpm for 6 minutes for suspension cells and GIBCO 0.05% Trypsin-EDTA (Fisher Scientific) to release adherent cells.

Plates were read for luminescence or fluorescence using a BMG Clariostar plate reader.

Resazurin sodium salt was purchased from Sigma-Aldrich and is dissolved in water.

qRT-PCR of AREs

Quantitative Real-Time Polymerase Chain Reaction was used to determine the minimal number of amplification cycles required for detectable signal, relative to mRNA levels and normalized to GAPDH. RNA was extracted from a pellet of 1-2 million cells stored at -80C until extraction. Extraction was carried out using Qiagen RNeasy Plus Mini Kits. PCR was performed in a BioRad CFX96 using either Quantabio or Azura 1-step qPCR mix with SYBR green real-time detection. 20uL Reactions were used. All primers were designed using recommended primers by Primer3.

Radiation Therapy Treatment

Cells were seeded 1 day prior to the first round of RT with RTI-79 being added 1 hour in advance and then being maintained on the cells unless otherwise noted. Cells were covered once drug was added prior to being irradiated and were stored in a Styrofoam container to minimize temperature shifts. The cells were sealed for 60-90 minutes and then unsealed when being returned to an incubator at 37C with 5% CO₂.

An Accuray TomoTherapy Hi-Art running software version 5.1.4. was used to irradiate cells 360 degrees around the sample to provide equal and focused exposure. The sample format is 2 96-well plates in a 3D-printed, PLA box with 10mm walls and 100 percent infill. This process ensures that the selected tumor area is given the desired dose while minimizing the harm to adjacent non-cancerous cells. Although the instrument is capable of applying a radiation gradient across the plate, each plate was given a uniform radiation dosage with outside wells excluded and 6 replicates.

Cells were irradiated with a dose of 0, 4, or 8 gray (gy), a measurement of the energy of the radiation dose, with 8gy being a large dose. For fractionated therapy, the cells were given 8gy in a single dose or ten doses of 2gy or 3gy, Monday-Friday for a total dose of 20gy and 30gy respectively. The fractionated dosing therapy was designed to mimic actual clinical treatment.

Cells were grown for 8 days after RT then 4ng/well of Resazurin was added to each well and read for fluorescence the following day. Plates were read for fluorescence in a BMG Clariostar plate reader. All data is normalized to control wells which received

only 0.5% DMSO, but without drug or radiation, but still sealed and transported with the corresponding cell plates.

RESULTS

A prostate cancer cell line was identified that had an inverse relationship for radiation therapy (RT) efficacy and synergy with a novel combination therapy. Other similarly behaving sensitive and resistant pairs of a particular type of cancer cell lines that are treated with chemotherapy versus RT have also been identified (data not shown). For a given cancer cell line, PC-3 in this example, cell lines not affected by a combination of RTI-79 and the standard of care, the typical therapy used for that type of cancer, both ROS producing treatments, show that their AhR and Nrf-2 pathways are upregulated (Table 1). Alternatively, cell lines showing synergy with RT and RTI-79, such as DU-145, often show a downregulation of the AhR and Nrf-2 pathways by 24 hours (Table 1).

To assess the impact of RT and/or RTI-79 on the following cell lines, the growth of the cell line after treatment is compared to the growth of the same cell line treated with 0.5% DMSO only. HDF, is used as an example of normal healthy tissue, and showed the expected response to 4gy (low) and 8gy (high) doses of RT, and were relatively unaffected by RTI-79 (Figure 2). Performing a student's t-test resulted a value of 1.8 and not significant at $p < 0.05$ confidence interval. HDF are not cancerous and have a normally functioning ROS response, so a lack of synergy with and lack of toxicity from RTI-79 supports the hypothesis.

MCF-7 is a breast cancer cell line that exhibits sensitivity towards both RTI-79 and RT (Figure 3). It was as expected then, that synergy would not exist in this cell line, and it was not observed. Synergy is expected in scenarios where resistance to RT or chemotherapy is observed because they have upregulated cellular responses to the therapy and have a lowered capacity to respond to additional stress. It should be noted though, that a safe (to normal healthy cells) dose of RTI-79 allows the same killing of the tumor at half the dosage of radiation, although this is not the most significant effect of RTI-79. It's useful regardless and exhibits that although RTI-79 may not be a magic bullet, it does safely contribute to controlling the tumor and lowering the required dose the patient must be exposed to. In the case of MCF-7, 20uM RTI-79 showed higher killing alone, than did 4gy RT.

On the opposite end of the spectrum is the lung epithelial cancer cell line A549, which has moderate resistance to both therapies (Figure 4) despite the fact that AREs are downregulated by dox and dox combination with RTI-79 (Figure 5). In spite of attempted downregulation of Nrf2, the fact that A549 has a mutant Keap1 explains why A549 is resistant to RTI-79 and RT despite transcription influence. RTI-79 does contribute up to 20% killing at 20uM in combination with 8gy radiation (Figure 4). Again, in a cell line where high levels of synergy are not observed, RTI-79 still provides a non-toxic boost to RT. In a cell line such as A549, 8gy+ would be necessary for death regardless of RTI-79, but a 20% boost from RTI-79 still helps protect healthy tissues. Due to the high dosage required despite combination with RTI-79, the combination could also limit the number

of treatments or used in combination with fractionated dosing to provide the best possible outcome for the patient.

DU-145 is resistant to both RTI-79 (Figure 5) and radiation (Figure 6). PC-3 is highly variable to both RTI-79 (Figure 5) and radiation (Figure 6). RTI-79 shows no killing of DU-145 up to 20uM while the same concentration on PC-3 causes 80% inhibition. When PC-3 is also treated with radiation, the effects of RTI-79 are no longer apparent (Figure 6). The fact that RTI-79 is causing a major upregulation of AREs could explain its lack of synergy to combination therapy (Table 1).

Despite DU-145 being resistant to RT and RTI-79, it shows synergy in combination (Figure 7). Even at 8gy (the highest single radiation dose given in these experiments), killing is less than 20%. In combination of RTI-79 and RT, an IC_{50} is surpassed by 20uM RTI-79 with 8gy or a 20gy fractionated dose regimen. 8gy is still a large dose to administer.

For oncological RT, the use of a fractionated dose has historically been established to cause more harm to cancerous cells, while healthy cells can perform a significant amount of DNA repair in between doses[41]. By using a much safer 2gy fractionated dose M-F for two weeks (10 doses), a reduction in growth equivalent to a single 8gy dose was achieved (Figure 8). The 2gy fractionated dose had no killing in the absence of RTI-79 and reduces harm to non-cancerous cells. The impact of DU-145 is the most pronounced observed in this study. As stated earlier, DU-145 has 55% viability after a 20gy dose, a dose that would be devastating to most tissues [41]. By using 2gy fractionated dosing with

RTI-79 a cancer as aggressive and resistant as DU-145 can still be effectively treated without massive damage to the surrounding tissues.

DISCUSSION

Even if a particular cancer doesn't see an appreciable synergy between the standard of care and RTI-79, RTI-79 has shown a range of effects on different cell lines ranging from no effect to significant inhibition, such as MCF-7, which exhibited over 50% killing at concentrations not toxic to healthy cells, defined here as 20uM against tissue culture. While it has been observed through qRT-PCR and western blot (Data from Maxwell lab, unpublished) that Nrf2 and AhR are inhibited to less than half of the untreated transcript level for DU-145, or in reduced Nrf2 protein levels in other cell lines. Sometimes a lack of efficacy from RTI-79 and RT therapy correlates with upregulation of Nrf2 and AhR. With nearly 50% of cancer having already started to spread at the time of detection, and survival rates around 35% down to <5% for more advanced cancers, novel treatments have the opportunity to save hundreds of thousands of lives [3].

The complete mechanism of action of RTI-79 seems to have a more complex interaction than just the Nrf2 and AhR pathways. There could also be a conditional state, currently unidentified, that impacts Nrf2 and AhR significantly as well. In other cell lines showing significant synergy with RTI-79 and dox, also show Nrf2 and AhR upregulation (Data not published). It was also observed that RTI-79 and RT combination lost synergy when RTI-79 was not maintained on the cells. This correlates with pharmacokinetic data and *in vivo* studies will have daily dosing of RTI-79. Rifabutin and RTI-79 are nearly

identical in structure (Figure 1) and very close to the rifimycins. While these analogs are broad spectrum antibiotics against bacterial RNA polymerase, research has shown that rifabutin and rifamycin have significant and opposing effects on the AhR pathway [44]. Attempts to replicate these results and characterize RTI-79 seem currently influenced and variable based on some currently unidentified parameter. The variation varies from inducing to inhibiting, preventing any conclusions.

Despite some unanswered questions as far as being able to predict which cancers, and to what degree, will respond the approach to treatment seems clear. A dual path approach is needed to fully characterize, and most effectively use, RTI-79 to treat a variety of cancers. While the biology is to be further elucidated, efficacy studies in animal models should show if the efficacy in tissue culture translates to systemic treatment. Studies are taking place in a canine model that are very favorable towards the hypothesis that RTI analogs can extend the lifespan and efficacy of chemotherapy (study not complete). The most impactful result from this series of experiments is that cancers, even as resistant as DU-145 can achieve the 8gy plus RTI-79 level of inhibition while only requiring relatively safe 2gy doses on a 2 week schedule.

While the combination therapy of RT and RTI-79 was ineffective against A549 lung epithelial cancer, it was likewise non-toxic to primary HDF cells. Although not all cancers will respond as favorably as DU-145, MCF-7 breast cancer exhibits an alternative effective scenario where both modalities effectively treat MCF-7 on their own, and additively together. As research continues at a biochemical level, further spontaneous and

xenograft animal models will provide data necessary to progress this treatment to clinical trials.

REFERENCES

1. Statistics, N.C.f.H., National Vital Statistics Reports, in National Vital Statistics System. 2021. p. <http://www.cdc.gov/nchs/deaths.htm>.
2. Arora, E., H. Verma, and A. Niranjana, Review on Targeted Cancer Therapy. *Journal of Critical Reviews*, 2020. 7(10): p. 1204-1208.
3. Etzioni, R., et al., The case for early detection. *Nature reviews cancer*, 2003. 3(4): p. 243-252.
4. Kempf, E., et al., New cancer cases at the time of SARS-Cov2 pandemic and related public health policies: A persistent and concerning decrease long after the end of the national lockdown. *European Journal of Cancer*, 2021. 150: p. 260-267.
5. More, M.P., et al., Recent advances in phytochemical based Nano-formulation for drug resistant Cancer. *Medicine in Drug Discovery*, 2021: p. 100082.
6. Venkatesulu, B.P., et al., A Systematic Review and Meta-Analysis of Cancer Patients Affected by a Novel Coronavirus. *JNCI Cancer Spectrum*, 2021. 5(2).
7. Ledermann, J.A. and R.S. Kristeleit, Optimal treatment for relapsing ovarian cancer. *Annals of Oncology*, 2010. 21: p. vii218-vii222.
8. Zhu, X., et al., Cancer evolution: A means by which tumors evade treatment. *Biomedicine & Pharmacotherapy*, 2021. 133: p. 111016.
9. Nambot, S., et al., Incidental findings in a series of 2500 gene panel tests for a genetic predisposition to cancer: Results and impact on patients. *European Journal of Medical Genetics*, 2021. 64(5): p. 104196.

10. Institute, N.C. Types of Cancer Treatment. 2021.
11. Baskar, R., et al., Cancer and radiation therapy: current advances and future directions. *International journal of medical sciences*, 2012. 9(3): p. 193.
12. Perillo, B., et al., ROS in cancer therapy: The bright side of the moon. *Experimental & Molecular Medicine*, 2020. 52(2): p. 192-203.
13. Kim, T.R., et al., Hypoxia-induced SM22 α in A549 cells activates the IGF1R/PI3K/Akt pathway, conferring cellular resistance against chemo- and radiation therapy. *FEBS Letters*, 2012. 586(4): p. 303-309.
14. Kim, S.J., H.S. Kim, and Y.R. Seo, Understanding of ROS-Inducing Strategy in Anticancer Therapy. *Oxidative Medicine and Cellular Longevity*, 2019. 2019: p. 5381692.
15. Liberti, M.V. and J.W. Locasale, The Warburg Effect: How Does it Benefit Cancer Cells? *Trends in Biochemical Sciences*, 2016. 41(3): p. 211-218.
16. Vaupel, P. and G. Multhoff, Revisiting the Warburg effect: historical dogma versus current understanding. *The Journal of Physiology*, 2021. 599(6): p. 1745-1757.
17. Chang, H.W., et al., p53-dependent glutamine usage determines susceptibility to oxidative stress in radioresistant head and neck cancer cells. *Cellular Signalling*, 2021. 77: p. 109820.
18. Cho, Y.A., et al., MYC single-hit large B-cell lymphoma: clinicopathologic difference from MYC-negative large B-cell lymphoma and MYC double-hit/triple-hit lymphoma. *Human Pathology*, 2021. 113: p. 9-19.

19. Lindsley, R.C. and A.S. LaCasce, Biology of double-hit B cell lymphomas. *Current opinion in hematology*, 2012. 19(4): p. 299.
20. Maxwell, S.A., et al., 14-3-3 ζ mediates resistance of diffuse large B cell lymphoma to an anthracycline-based chemotherapeutic regimen. *Journal of Biological Chemistry*, 2009. 284(33): p. 22379-22389.
21. Sun, X., et al., Selective induction of tumor cell apoptosis by a novel P450-mediated reactive oxygen species (ROS) inducer methyl 3-(4-nitrophenyl) propiolate. *Journal of Biological Chemistry*, 2013. 288(13): p. 8826-8837.
22. Madesh, M. and G.r. Hajnóczy, VDAC-dependent permeabilization of the outer mitochondrial membrane by superoxide induces rapid and massive cytochrome c release. *Journal of Cell Biology*, 2001. 155(6): p. 1003-1016.
23. Miao, W., et al., Transcriptional regulation of NF-E2 p45-related factor (NRF2) expression by the aryl hydrocarbon receptor-xenobiotic response element signaling pathway: direct cross-talk between phase I and II drug-metabolizing enzymes. *Journal of Biological Chemistry*, 2005. 280(21): p. 20340-20348.
24. Shin, S., et al., NRF2 Modulates Aryl Hydrocarbon Receptor Signaling: Influence on Adipogenesis. *Molecular and Cellular Biology*, 2007. 27(20): p. 7188-7197.
25. Kensler, T.W., N. Wakabayashi, and S. Biswal, Cell survival responses to environmental stresses via the Keap1-Nrf2-ARE pathway. *Annu. Rev. Pharmacol. Toxicol.*, 2007. 47: p. 89-116.
26. Zhang, Z.-H., et al., ROS-mediated genotoxic stress is involved in NaAsO₂-induced cell cycle arrest, stemness enhancement and chemoresistance of prostate

- cancer cells in a p53-independent manner. *Ecotoxicology and Environmental Safety*, 2021. 208: p. 111436.
27. Merlin, J.P.J., et al., Role of Dietary Antioxidants in p53-Mediated Cancer Chemoprevention and Tumor Suppression. *Oxidative Medicine and Cellular Longevity*, 2021. 2021: p. 9924328.
 28. Vucic, V., et al., Effects of gamma-radiation on cell growth, cycle arrest, death, and superoxide dismutase expression by DU 145 human prostate cancer cells. *Brazilian journal of medical and biological research*, 2006. 39: p. 227-236.
 29. Chendil, D., et al., Curcumin confers radiosensitizing effect in prostate cancer cell line PC-3. *Oncogene*, 2004. 23(8): p. 1599-1607.
 30. Hadi, F., et al., Combinatorial effects of radiofrequency hyperthermia and radiotherapy in the presence of magneto-plasmonic nanoparticles on MCF-7 breast cancer cells. *Journal of Cellular Physiology*, 2019. 234(11): p. 20028-20035.
 31. Alkarakooly, Z., et al., Metabolic reprogramming by Dichloroacetic acid potentiates photodynamic therapy of human breast adenocarcinoma MCF-7 cells. *PLOS ONE*, 2018. 13(10): p. e0206182.
 32. Sitthideatphaiboon, P., et al., STK11/LKB1 mutations in NSCLC are associated with KEAP1/NRF2-dependent radiotherapy resistance targetable by glutaminase inhibition. *Clinical Cancer Research*, 2021. 27(6): p. 1720-1733.
 33. Ohta, T., et al., Loss of Keap1 Function Activates Nrf2 and Provides Advantages for Lung Cancer Cell Growth. *Cancer Research*, 2008. 68(5): p. 1303.

34. Torella, J.P., R. Chait, and R. Kishony, Optimal Drug Synergy in Antimicrobial Treatments. *PLOS Computational Biology*, 2010. 6(6): p. e1000796.
35. Yagoda, A. and D. Petrylak, Cytotoxic chemotherapy for advanced hormone-resistant prostate cancer. *Cancer*, 1993. 71(S3): p. 1098-1109.
36. McMahon, S.J., The linear quadratic model: usage, interpretation and challenges. *Physics in Medicine & Biology*, 2018. 64(1): p. 01TR01.
37. Van Leeuwen, C., et al., The alfa and beta of tumours: a review of parameters of the linear-quadratic model, derived from clinical radiotherapy studies. *Radiation oncology*, 2018. 13(1): p. 1-11.
38. Fowler, J.F., Biological Factors Influencing Optimum Fractionation in Radiation Therapy. *Acta Oncologica*, 2001. 40(6): p. 712-717.
39. Widmark, A., et al., Ultra-hypofractionated versus conventionally fractionated radiotherapy for prostate cancer: 5-year outcomes of the HYPO-RT-PC randomised, non-inferiority, phase 3 trial. *The Lancet*, 2019. 394(10196): p. 385-395.
40. Rich, S.E., et al., Update of the systematic review of palliative radiation therapy fractionation for bone metastases. *Radiotherapy and Oncology*, 2018. 126(3): p. 547-557.
41. Logani, S., et al., Single-Dose Compared With Fractionated-Dose Radiation of the OM431 Choroidal Melanoma Cell Line. *American Journal of Ophthalmology*, 1995. 120(4): p. 506-510.

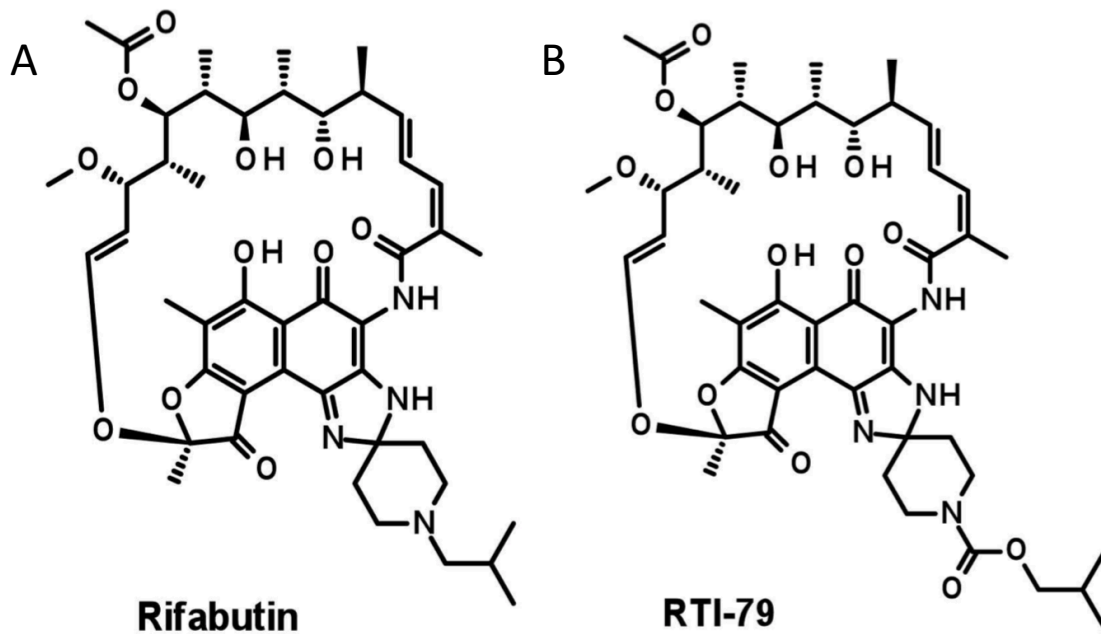
42. Murthy, V., et al., Prostate-only versus whole-pelvic radiation therapy in high-risk and very high-risk prostate cancer (POP-RT): Outcomes from phase III randomized controlled trial. *Journal of Clinical Oncology*, 2021. 39(11): p. 1234-1242.
43. Stolzenbach, L.F., et al., External beam radiation therapy improves survival in low-volume metastatic prostate cancer patients: a North American population-based study. *Prostate Cancer and Prostatic Diseases*, 2021. 24(1): p. 253-260.
44. Puyskens, A., et al., Aryl Hydrocarbon Receptor Modulation by Tuberculosis Drugs Impairs Host Defense and Treatment Outcomes. *Cell Host & Microbe*, 2020. 27(2): p. 238-248.e7.

Table II-1: Prostate Cancer mRNA Levels

		Nrf2	AhR
PC-3	RTI-79 10uM - 24 hr	163.19	5024.65
	Dox 2uM - 24hr	1.06	0.88
	Dox 2uM + RTI-79 10uM - 24 hr	2.58	4.66
DU-145	RTI-79 10uM - 24 hr	0.31	0.03
	Dox 2uM - 24hr	0.43	0.45
	Dox 2uM + RTI-79 10uM - 24 hr	0.48	0.05

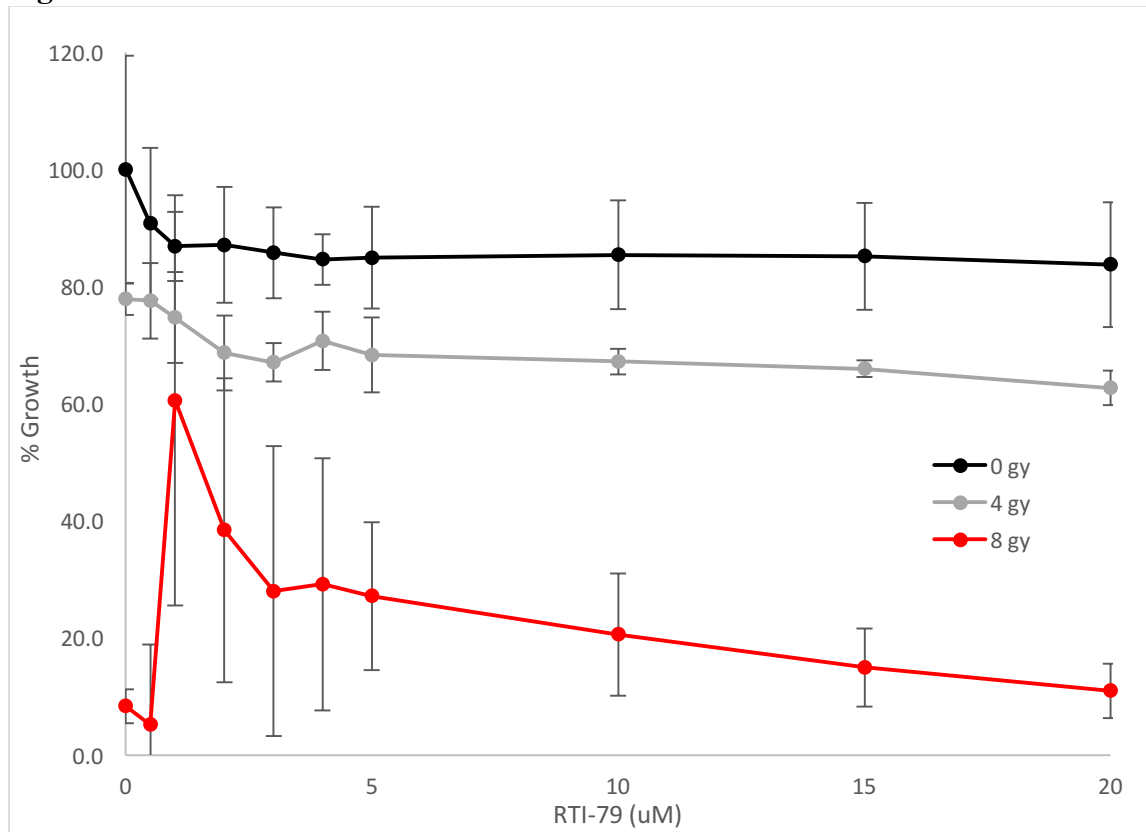
PC-3 and DU-145 cells adhered in a flask, were treated for 24 hours with the listed conditions and a constant 0.5% DMSO. Results are displayed as fold change compared to DMSO only and normalized to GAPDH levels, N=1.

Figure II-1: RTI-79 Structure.



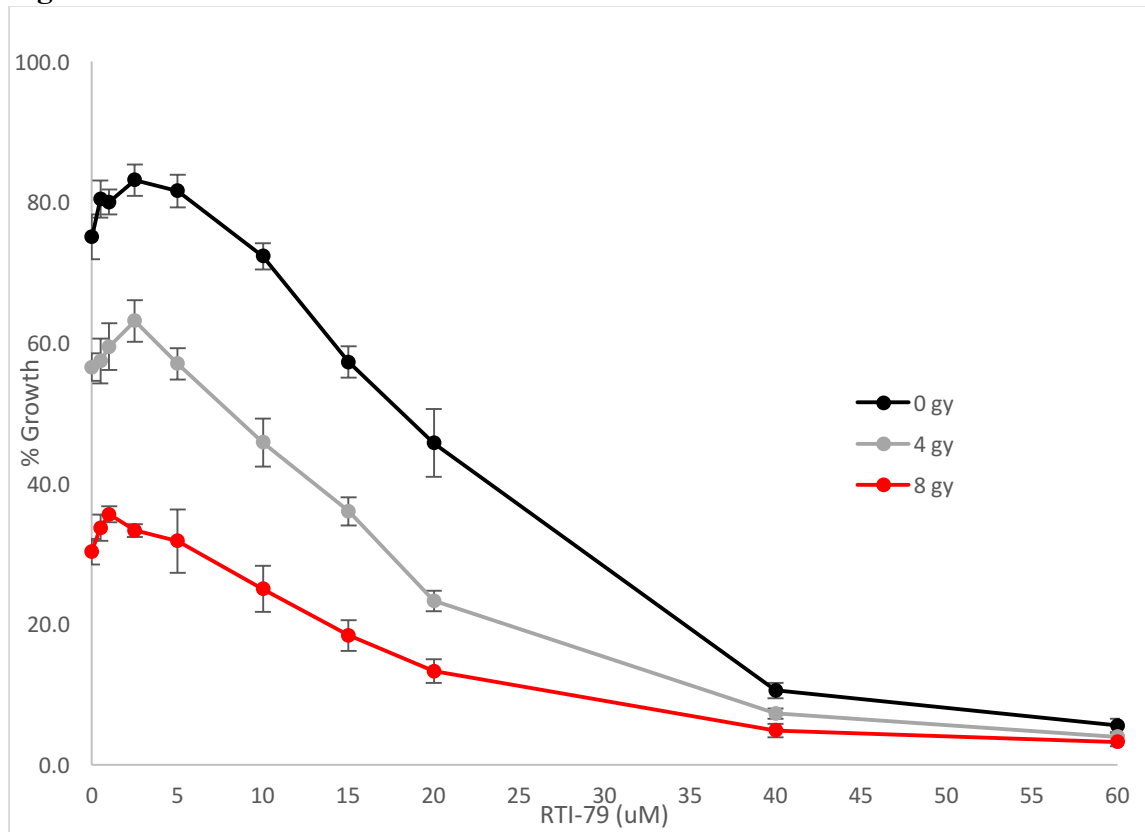
The chemical structure of (A) the antibacterial RNAP inhibitor, rifabutin and (B) RTI-79.

Figure II-2: HDF - RT in Combination with RTI-79.



HDF cells were treated using the standard RT protocol listed in methods at the doses of 0gy, 4gy, and 8gy with a range of RTI-79 up to 20 μM , exposed for 1 hour prior to radiation therapy, with an N=6, using 4ng Resazurin per well at day 8 and read on day 9 post radiation. Error bars represent 1 standard deviation. HDF cells are a surrogate for healthy tissues surrounding the tumor that will be irradiated as a result, albeit at lower levels than the tumor.

Figure II-3: MCF-7 RT in Combination with RTI-79



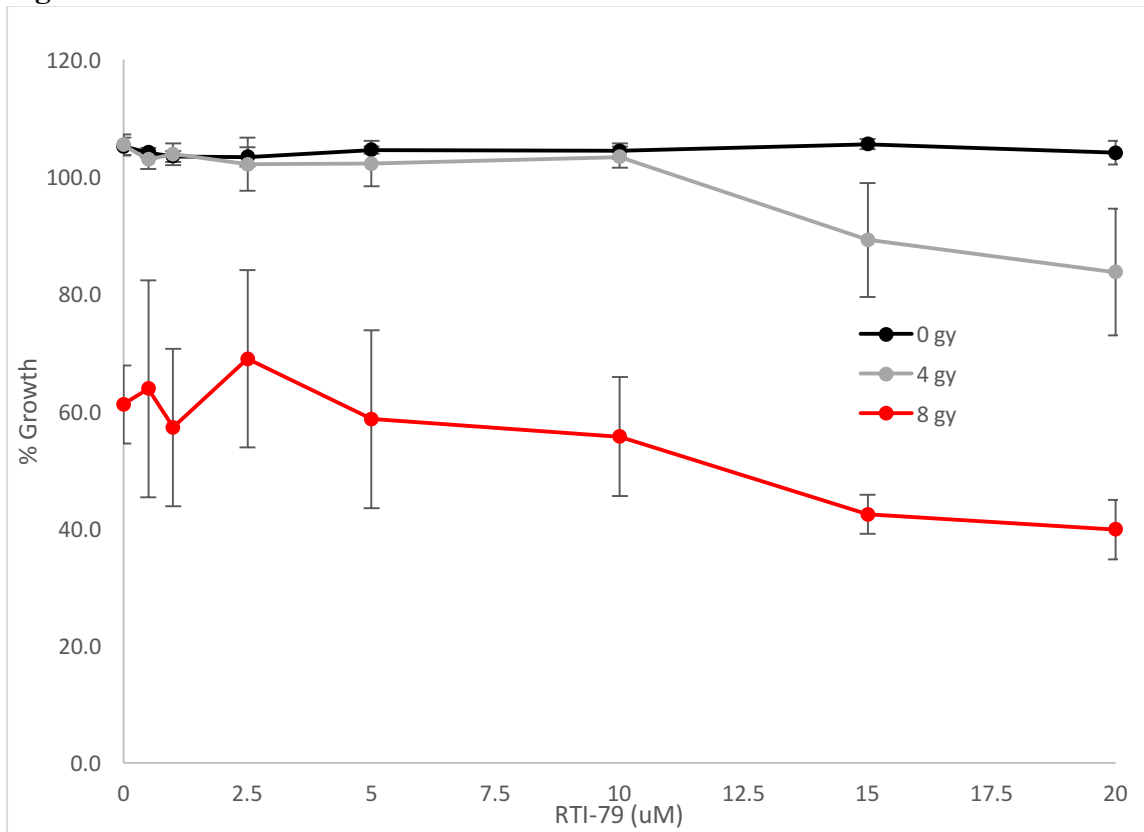
MCF-7 cells were treated using the standard RT protocol listed in methods at the doses of 0gy, 4gy, and 8gy with a range of RTI-79 up to 20uM, exposed for 1 hour prior to radiation therapy, with an N=6, read using 4ng Resazurin per well on day 8 and read on day 9. Error bars represent 1 standard deviation. 20uM is the highest “safe” dose to be considered therapeutically useful. MCF-7 cells experiences sensitivity to both RT and RTI-79, with 20uM RTI-79 causing a 54% reduction in growth alone. The combinatorial effects are less than the additive effect of each treatment individually, but still effective. 4gy plus RTI-79 (20uM) has the same reduction in growth as 8gy alone.

Table II-2: A549 qRT-PCR.

		Nrf2	AhR
A549	RTI-79 10uM - 24 hr	0.95	2.30
	Dox 2uM - 24hr	0.31	0.27
	Dox 2uM + RTI-79 10uM - 24 hr	0.01	N.D.

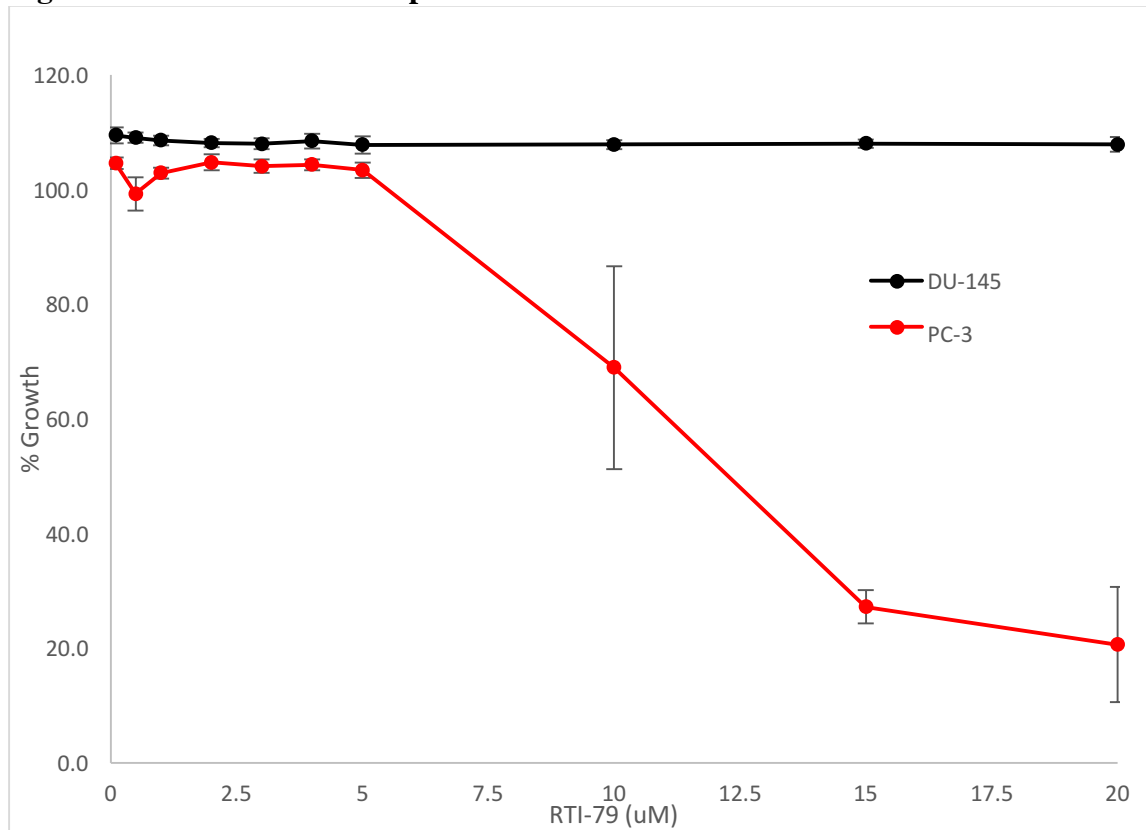
A549 cells adhered in a flask, were treated for 24 hours with the listed conditions and a constant 0.5% DMSO. Results are displayed as fold change compared to DMSO only and normalized to GAPDH, N=1

Figure II-4: A549 RT in Combination with RTI-79



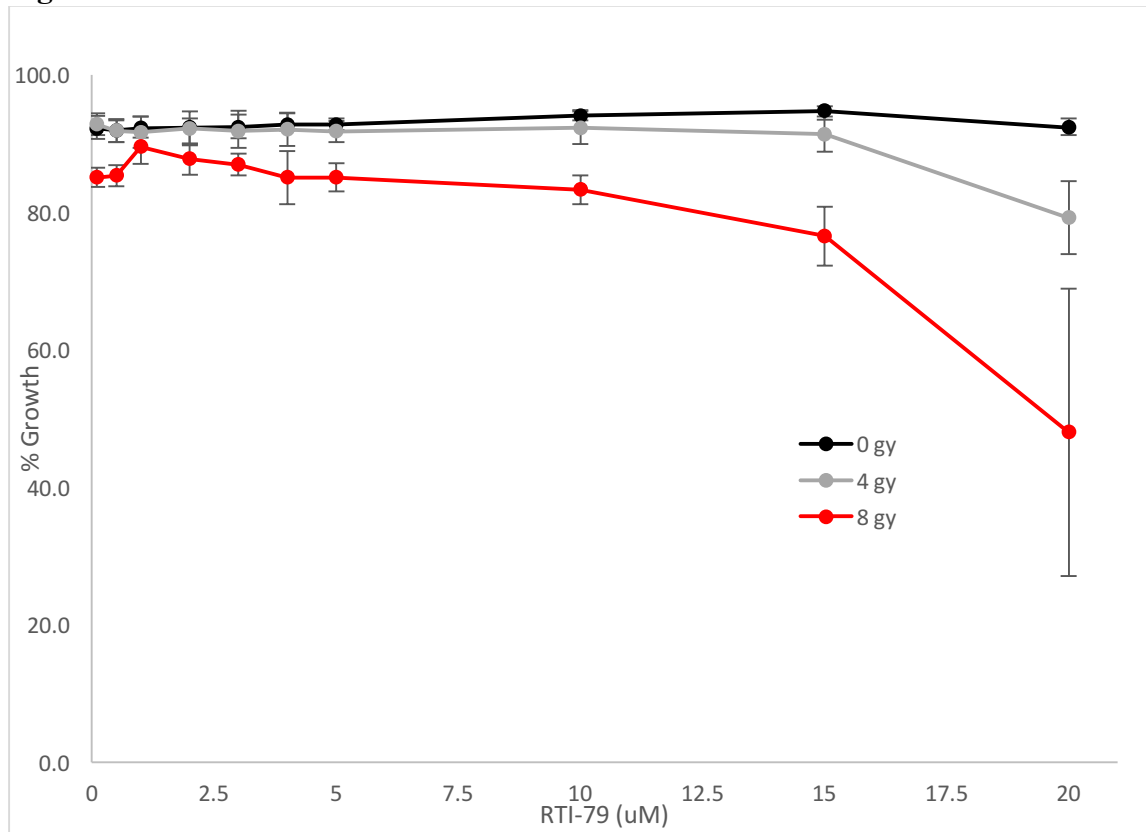
A549 cells were treated using the standard RT protocol listed in methods at the doses of 0gy, 4gy, and 8gy with a range of RTI-79 up to 20uM, with an N=6, using 4ng Resazurin per well on day 8 and read on day 9. Error bars represent 1 standard deviation. 20uM is the highest “safe” dose to be considered therapeutically useful. RTI-79 alone is non-toxic to A549 cells although it was capable of adding a 20% reduction in growth at 20uM in combination compared to RT (4gy or 8gy) alone.

Figure II-5: RTI-79 Dose Response.



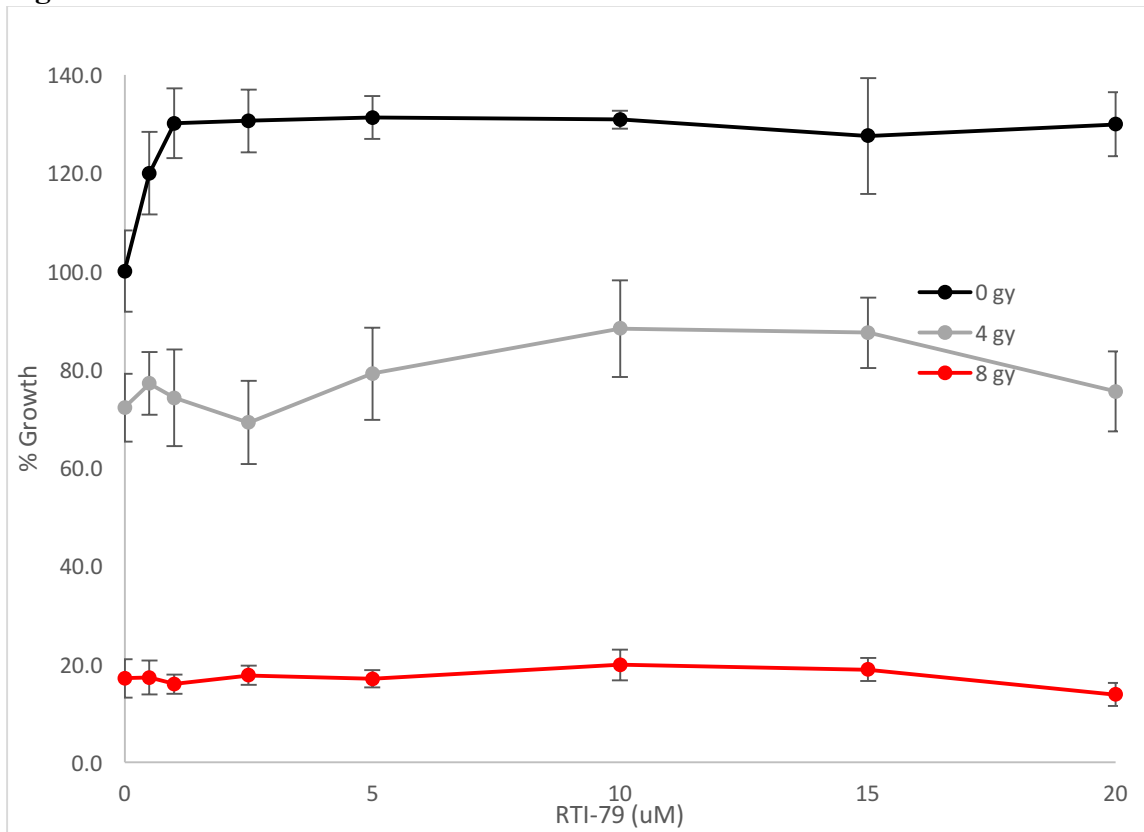
DU-145 and PC-3 cells were both exposed to a range of RTI-79. DU-145 cells showed no sensitivity and PC-3 cells indicated a high sensitivity, however, all future experiments showed PC-3 cells also not being sensitive to RTI-79. Error bars represent 1 standard deviation. PC-3 cells exhibiting this variation may be indicative of other scenarios where a particular cell line has a wide range of response to RTI-79 and combination therapies. All concentrations have N=6, DU-145 had 2000 cells/well, while PC-3 had 400 cells/well. Readout was determined by using 4ng/well of resazurin added on day 8 and read on day 9.

Figure II-6: DU-145 RT in Combination with RTI-79.



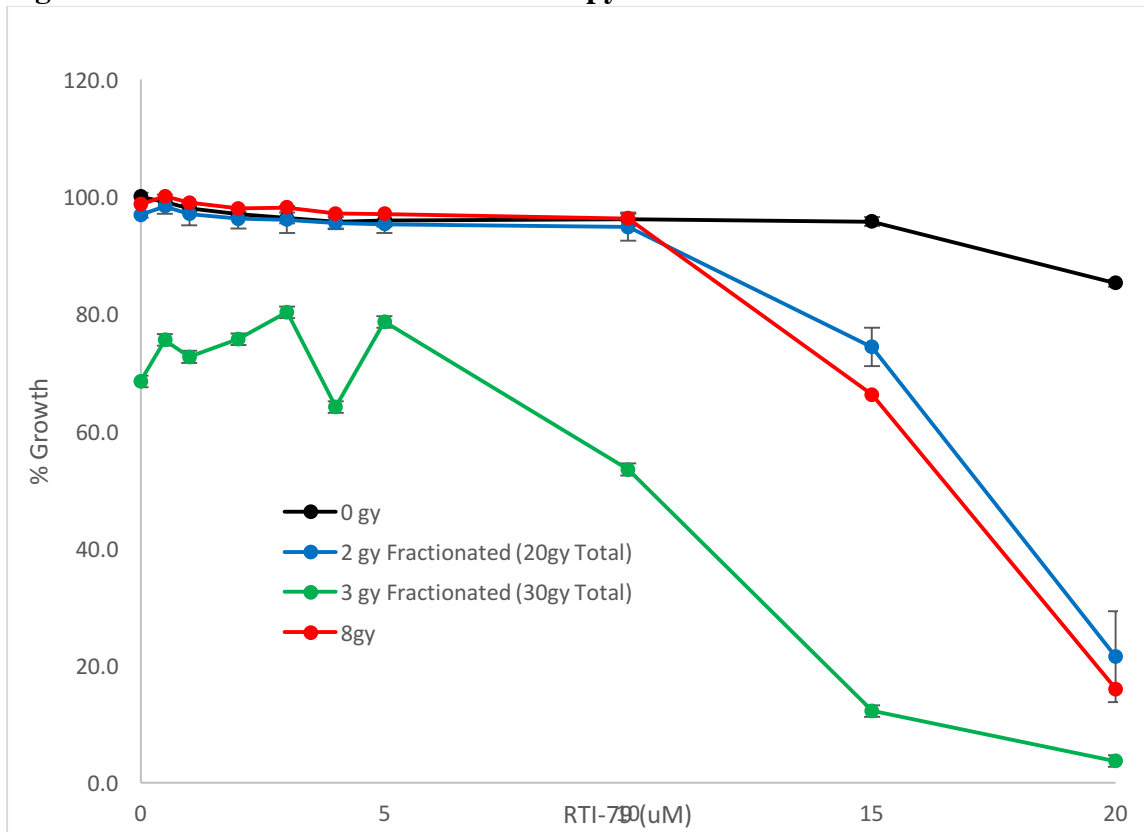
DU-145 cells were treated using the standard RT protocol listed in methods at the doses of 0gy, 4gy, and 8gy with a range of RTI-79, N=6. Error bars represent 1 standard deviation. Synergy Between RTI-79 and 8gy of radiation shows over 50% reduction in growth.

Figure II-7: PC-3 RT in Combination with RTI-79.



PC-3 cells were treated using the standard RT protocol listed in methods at the doses of 0gy, 4gy, and 8gy with a range of RTI-79. Error bars represent 1 standard deviation. PC-3 here consistently shows no sensitivity to RTI-79 as well as exhibiting high sensitivity to RT.

Figure II-8: Fractionated Radiation Therapy in Combination with RTI-79.



DU-145 cells were treated with an 8gy single dose. They were also treated with fractionated therapy of 2gy or 3gy Monday through Friday for 2 weeks, 10 doses total, N=6. Error bars represent 1 standard deviation. Resazurin at 4ng/well was added after the final fractionated dose and read the following day.

CHAPTER III

ELESCLOMAL ALLEVIATES MENKES PATHOLOGY AND MORTALITY IN A MOUSE MODEL BY ESCORTING CU TO CUPROENZYMES IN CELLS*

ABSTRACT

Loss of function mutations in the copper transporter ATP7A causes Menkes disease. Menkes is an infantile fatal hereditary copper deficiency disorder characterized by progressive neurological injury culminating in death typically by three years of age. Severe copper deficiency leads to multiple pathologies including impaired energy generation caused by cytochrome c oxidase dysfunction in the mitochondria. Here we report that the small molecule, elesclomol, escorted copper to mitochondria and increased cytochrome c oxidase levels in the brain. Through this mechanism, elesclomol prevented detrimental neurodegenerative changes and improved survival of the mottled-brindled mouse; a murine model of severe Menkes disease. Thus, elesclomol holds promise for the treatment of Menkes and associated disorders of hereditary copper deficiency.¹

*Part of this chapter is reprinted with permission from “Elesclomol alleviates Menkes pathology and mortality in a mouse model by escorting Cu to cuproenzymes in cells” by Liam M. Guthrie, Shivatheja Soma, Sai Yuan, Andres Silva, Mohammad Zulkifli, Thomas C. Snavely, Hannah Faith Greene, Elyssa Nunez, Brogan Lynch, Courtney De Ville, Vinit Shanbhag, Franklin R. Lopez, Arjun Acharya, Michael J. Petris, Byung-Eun Kim, Vishal M. Gohil, James C. Sacchettini, 2020. *Science*, 368, 620-625, Copyright [2020] by Science Magazine.

INTRODUCTION

Effective Copper Transportation is Vital for Viable Nervous System Development

Copper (Cu) is an essential micronutrient required for numerous critical enzyme including cytochrome *c* oxidase (CcO) of the ATP-generating electron transport pathway found in mitochondria (1). Paradoxically, Cu possesses inherent toxicity, in part because of its ability to generate hydroxyl radicals in biological systems (2). Organisms have evolved highly complex systems of metallochaperones and transporters to safely distribute Cu (3, 4). Mutations impairing the function of any component of Cu transport can impact numerous cellular processes affecting systems as diverse as energy production (5, 6), catecholamine biosynthesis, and connective tissue maturation—resulting in debilitating, often fatal human diseases (7).

The coordinated efforts of the two major Cu membrane transporters, CTR1 and ATP7A, regulate intracellular Cu levels and directional transport across polarized epithelial layers such as the intestinal enterocyte lining (8) and choroid plexus (9). CTR1 effects initial Cu entry while ATP7A facilitates Cu egress from cells.

Mutations in the Cu transporting ATPase, *ATP7A*, results in Menkes disease - a fatal X-linked infantile condition with no FDA-approved treatment (10). Clinical presentations of Menkes include abnormal catecholamine ratios, characteristic kinky hair, hypopigmentation, connective tissue defects, and severe neurodegeneration (7, 10, 11). In the brain, this Cu deficit causes secondary CcO dysfunction leading to progressive neurological injury and death (12-14). Efforts to restore normal Cu levels and enzyme function by means of parenteral Cu supplementation using hydrophilic complexes, such

as copper histidine, do not always ameliorate severe neurological pathology in Menkes patients because of poor penetrance and low restoration of neuronal CcO function in the brain (14, 15). We previously reported that elesclomol (ES), a small highly lipophilic Cu²⁺-binding molecule, restores mitochondrial function in the context of defective Cu transport in yeast and mammalian cell lines (16). A membrane traversing drug like ES, capable of Cu delivery to key cuproenzymes, such as CcO in brain mitochondria, should translate to *in vivo* models and alleviate the neurodegenerative aspects of Menkes disease. This would be similar to hinokitiol, a lipophilic carrier that restores iron levels in the context of defective membrane transport both *in vitro* and *in vivo* (17, 18). Modeling Systemic Disease

Menkes syndrome is biologically well understood, however, an effective treatment becomes complicated because affected males systemically sequester copper intestinally, creating insufficient copper levels systemically, which leads to hampered development of the nervous system. Despite the genetic mutation being expressed selectively in different types of tissue, the complex nature of the disrupted copper homeostasis systemically needs to, in practice, be tested *in vivo* to understand if a particular treatment will be effective.

Several neurological and protein misfolding diseases found in human brains are able to be modeled in yeast (34). This type of approach works well to quickly test intracellular biological deficiencies. Due to the fact that Menkes syndrome causes sequestration in the digestive tract and doesn't achieve distribution to other tissues, rescue must accomplish both removal from deposition stockpiles and facilitate delivery to depleted cells. New compounds can be tested for the ability to impact copper homeostasis

in cells, but testing must then be elevated to an animal model to demonstrate that copper homeostasis is corrected organism wide.

A treatment which corrects that deficiency is the most straightforward means to treat patients with Menkes. Two major approaches to treating Menkes have been using copper bound to a transporting molecule, such as copper histidine, and using viral gene therapy to restore ATP7A activity [24]. While neither therapy had any statistically significant effect alone, a combined therapy was able to provide 53% survival greater than 300 days in mice [24]. Unfortunately, the historical neurological results from a combined viral and copper therapy are not described with sufficient detail to compare to our ES-Cu²⁺ treatment although it does appear generally that the ES-Cu²⁺ therapy had an impact on rescue of Menkes' phenotype [24]. A direct comparison of ES-Cu²⁺ to copper histidine therapy shows that ES-Cu²⁺ is far superior by all measured metrics. This begs the question of potential efficacy from a future study using a combination therapy with viral genome editing and ES-Cu²⁺ used in place of copper histidine.

Current studies to utilize viral gene therapy have run into issues with the size limitations of viral systems [35]. One way to circumvent that is the use of multiple vectors, but at the cost of significant efficacy [35]. Clinical viral gene therapy on humans began in 2016 [35]. Off-target effects are a major concern, but that concern drives research to identify and rectify this potentially lethal error [35]. From a cost and sophistication approach, small molecule drugs are much more feasible than viral therapy, at least with current technology. Neither ES-Cu²⁺ nor viral therapy has been used to treat Menkes in humans, so the best empirical comparison of different treatments is to look at results from

treating the *mo-br* murine model. The most effective combination of viral gene therapy with copper histidine provided 75% survival at 30 days, while ES-Cu²⁺ without any gene therapy provided 82% survival at 10 weeks (the endpoint for our publication) [24]. Whether looking at cost, efficacy, or current treatment capabilities, administration of ES-Cu²⁺ is far superior to copper histidine. Future studies should focus on adapting viral gene therapy for Menkes to humans as well as combination therapies using ES in place of histidine.

MATERIALS AND METHODS

Reagents

Elesclomol (> 98.8%) was purchased from Accel Pharmtech (E. Brunswick, NJ). Captisol®, a proprietary β -cyclodextrin SBE derivative, was purchased from CyDex Pharmaceuticals, Inc. (Lenexa, KS). Methocel™ A15 LV, a proprietary carboxymethyl cellulose, was purchased from Dow, Inc. (Midland, MI). All other chemicals and reagents were purchased from Sigma-Aldrich unless otherwise noted.

Synthesis of elesclomol-Cu²⁺ Complex

The copper complex of ES was synthesized as described by Yadav et al, J Inorg Biochem. 2013/PMID: 23707906. Briefly, to a stirred solution of 6.0 mmol ES in ethanol, excess CuCl₂·2H₂O was added and stirred at room temperature for one hour to allow complete 1:1 stoichiometric complexation. Crude solid was precipitated by the addition of water and collected by filtration. The solid was dissolved in methylene chloride and

filtered. The methylene chloride solution was further washed three times with water followed by acetone, dried with Na₂SO₄, and a solid recovered following solvent removal in a rotary evaporator. Solid was further purified by two rounds of crystallization from acetonitrile followed by a final, 48-hour lyophilization yielding a fine, dark reddish-brown powder. Powder was stored at 4°C for pharmacological formulations.

Synthesis of copper histidine complex

The copper complex of histidine was synthesized as described by Gala et al, Molecules. 2014/PMID: 24434671. Briefly, to a stirred solution of 0.2 mmol pharmaceutical grade L-histidine in 100 mM HEPES buffer pH 7.4, CuCl₂·2H₂O (17.05 mg) was added and stirred at room temperature for three hours to allow complete 2:1 stoichiometric complexation. The resulting dark blue solution was filtered to remove particulates and stored at 4°C for use as a 50 mM HIS-Cu²⁺ stock solution for pharmacological formulations.

In vivo pharmacokinetics and toxicological assessment of elesclomol & elesclomol-

Cu²⁺

Formulation: Phase solubility assays were conducted to determine suitability of vehicles for ES and ES-Cu²⁺ complex in Methocel™ A15-LV and Captisol® per technical materials. Briefly, 500 μL Captisol® preps at 40%, 20%, 10%, and 5% (w/v) were mixed with 5, 2.5, 1.25, and 0.63 mg ES or ES-Cu²⁺ powder in micro centrifuge tubes. Solutions were sonicated and continuously agitated over night with micro spin bars

at 30°C to ensure maximum dissolution. Samples were centrifuged at 6000 rpm for 2 hours to pellet out undissolved material. Solvated ES and ES-Cu²⁺ was quantified by LC-MS. A similar protocol was followed for Methocel™ at 2.0%, 1.0%, 0.5%, and 0.25% (w/v) utilizing 2% DMSO final concentration as an excipient. Methocel™ poorly solubilized ES-Cu²⁺ but adequately solubilized ES and was used for cardiac Ctr1 KO mouse experiments. 20% Captisol® aqueous vehicle was used for ES-Cu²⁺ administration for mo-br mouse experiments.

ES & ES-Cu²⁺ Tolerability: Cohorts of five C57BL/6 adult female mice averaging 20 g were administered 25 mg/kg ES, 7.25 mg/kg ES-Cu²⁺, 3.625 mg/kg ES-Cu²⁺, 0.5% Methocel™ vehicle or 20% Captisol® vehicle via 400 µL subcutaneous injection. Mice were monitored daily for signs of acute toxicity, injection site reaction, and changes in total body weight. Body weight measurements were conducted on day 0, 5, and 10 of protocol and analyzed as percent change from initial weight. Vehicle, ES, and ES-Cu²⁺ cohorts were then compared.

ES & ES-Cu²⁺ Pharmacokinetics: C57BL/6 adult mice averaging 20 g were administered ES subcutaneously in 0.5% Methocel™, 2% DMSO aqueous vehicle at 10 mg/kg. ES-Cu²⁺ was administered as a single bolus dose by intravenous, subcutaneous, or oral routes formulated in 20% Captisol® aqueous vehicle at 3.625 (IV), 7.25 (SubQ), and 10.875 (Oral) mg/kg. Serial blood sampling was conducted at 0, 0.05, 0.25, 0.5, 1, 2, 4, 8, and 24 hours with each time point representing a biological triplicate. Whole blood was collected in heparinized tubes and spun down at 2200 rpm for five minutes. Plasma was collected and frozen at -80°C until quantitative analysis by LC-MS. Non-

compartmental and compartmental analysis was conducted using PKSolver software as described in Zhang et al, Comput Methods Programs Biomed. 2010/PMID: 20176408. Intravenous and/or subcutaneous PK parameters were generated in PKSolver using a single (Methocel™, ES) or type 2a 2-compartment (Captisol®, ES-Cu2+) model. Oral route was not modeled due to poor systemic exposure. Bioavailability was calculated manually using the following equation:

$$F_{abs} = [(AUC_{0-inf}^{Oral}/SQ \times DIV)] / [(AUC_{0-inf}^{IV} \times D^{Oral}/SQ)] \times 100\%$$

Brain elesclomol-Cu2+ exposure

Cohorts of six postnatal age 7 day pups and adult C57BL/6 mice were administered ES-Cu2+ as a single bolus dose at 7.25 mg/kg via subcutaneous injection in 20% Captisol®. Two mice of each age group were administered vehicle only. Mice were euthanized by isoflurane overdose and thoracotomy. Blood was removed by cardiocentesis and carcasses perfused with 20-50 mL normal saline. Brains were harvested, flash frozen with liquid nitrogen, and stored at -80°C pending analysis.

LC-MS quantification of elesclomol & elesclomol-Cu2+ in plasma and brain

Plasma Processing: Plasma collected from mice was thawed and 100 µL extracted with two 500 µL volumes of acetonitrile. Samples were spun down at 2200 rpm for five minutes and supernatant transferred to clean 1.7 mL micro centrifuge tube. Solvent was evaporated in a Vacufuge™ (Eppendorf™) concentrator at 45°C for 3 hours. Plasma extracts were reconstituted in 100 µL acetonitrile + 0.1% formic acid spiked with 100

ng/mL fluconazole internal standard. Constitution of standards involved spiking of ES/ES-Cu²⁺ in control plasma ranging from 1000 ng/mL to 1.93 ng/mL followed by identical processing to correct for matrix effects. All samples were run as biological triplicates and technical duplicates.

Brain Processing: Brain tissue was mechanically pulverized by ball milling using a CryoMill (Retsch® Newtown, PA). Homogenate was collected and extracted with 36 μ L of extraction buffer consisting of 75% acetonitrile, 25% methanol + 0.2% formic acid spiked with 100 ng/mL fluconazole internal standard per milligram of tissue. 4 μ L of ultrapure water per milligram of tissue was added and mixture vortexed for 30 s. Mixture was then centrifuged at 6000 rpm, 4°C and supernatant collected for analysis. Constitution of standards involved spiking of ES or ES-Cu²⁺ in control brain homogenate ranging from 1000 ng/mL to 1.93 ng/mL followed by identical processing to correct for matrix effects. All samples were run as biological triplicates and technical duplicates.

LC-MS Protocol: ES and ES-Cu²⁺ in plasma and brain were detected and quantified on a triple quadrupole mass spectrometer (Quantiva, Thermo Scientific, Waltham, MA) coupled to a binary pump HPLC (UltiMate 3000, Thermo Scientific). MS parameters were optimized for the target compound under direct infusion at 5 μ L min⁻¹ to identify the SRM transitions (precursor/product fragment ion pairs). Samples were maintained at 4 °C on an autosampler before injection. The injection volume was 10 μ L. Chromatographic separation was achieved on a Hypersil Gold 5 μ m 50 x 3 mm column (Thermo Scientific) maintained at 30 °C using a solvent gradient method. Solvent A was 0.1% formic acid in water. Solvent B was 0.1% formic acid in acetonitrile. The gradient

method used was 0-1.6 min (20% B to 80% B), 1.6-4 min (80% B) and 4-5 min (80% B to 20% B). The flow rate was 0.5 mL min⁻¹. Sample acquisition and analysis was performed with TraceFinder 3.3 (Thermo Scientific).

Cardiac CTR1 knockout mice

The cardiac-specific Ctr1 deletion mouse (Ctr1^{hrt/hrt}) was generated by crossing Ctr1^{flox/flox} mice (Nose et al, Cell Metab., 2006/PMID:16950140) with mice expressing Cre recombinase driven by the promoter of cardiac-expressed β -Myosin Heavy Chain (MHC) obtained from the Jackson Laboratory as performed previously (Kim et al, Cell Metab., 2010/PMID: 20444417). Age-matched Ctr1^{flox/+} or Ctr1^{flox/flox} siblings not expressing Cre served as control animals. All mouse genotypes were confirmed by performing Ctr1 excision genotyping PCR on cardiac tissue as previously described in Kim et al 2010 and cardiac Ctr1 protein levels in selected mice were determined by immunoblot. All mice were maintained on the C57BL/6 genetic background. All animal procedures were performed in accordance with the National Institutes of Health Guide and approved by the Institutional Animal Care and Use Committee (IACUC) at the University of Maryland, College Park (Protocol # R-APR-18-14).

Mottled-brindled mice

Heterozygous C57BL/6-Atp7A^{+ /mo-br} /J females and wildtype C57BL/6-Atp7A^{+ /y} /J males were procured from the Jackson Laboratory. Mice were housed in an OptiMice® animal care system with 14/10 hour light-dark cycle. Breeding for

experimental and colony maintenance purposes involved random sibling crosses between carrier females and wildtype males. Cage and nutritional enrichment in the form of nestlets, shepherd huts, and Love Mash® (Bio-Serv) reproductive supplement was provided in addition to Teklad 4% fat standard diet (Envigo) and water ad libitum. Litter size for experimental pairs was reduced to 3-4 pups by culling of females. On post-natal day 5, tail snip biopsies of males were used to confirm genotypes of pigment deficient mice. Genomic DNA was isolated and amplified using PCR forward primer (5' TTAATCTATAGGGCAAACCT) and reverse primer (5' GAGTTCAGAGTTACAATAGTG 3') containing the mo-br 6-bp deletion followed by electrophoretic separation on a polyacrylamide gel. All breeding and experimental procedures were approved by the Texas A&M University IACUC under protocols #2017-0380 and #2018-0069.

Administration of elesclomol to cardiac Ctr1 knockout mice

ES Formulation & Delivery: 10 mg/kg body weight ES or 0.5% Methocel™ vehicle (final 2% DMSO) was subcutaneously administered to cardiac Ctr1 KO and WT control mice every three days until post-natal day 26 after which dosing frequency was reduced to once weekly until post-natal day 54. Weight adjusted amounts of ES were first dissolved in DMSO and mixed with Methocel™ solution to reach a 2% final DMSO concentration. Mouse body weight was recorded daily from post-natal day 5 to 26 then weekly from 26 to 54. Survival and growth curves were generated from observational data.

Subsequent subsets of mice on post-natal day 10 and 26 were harvested for histological and biochemical analysis.

Administration of elesclomol, elesclomol-Cu²⁺, and copper histidine to mo-br mice

ES Formulation & Delivery: 2X stock solution of ES was prepared by wetting 2.5 mg ES base with 10 mL 20% Captisol® solution. Slurry was sonicated for 5 min. at 30°C and continuously mixed at constant temperature for 3 hours to ensure complete dissolution. Material was filtered and stored at 4°C yielding a stock of 250 µg/mL. Final formulation involved 1:2 dilution of stock with Captisol® to 125 µg/mL with adjustment of pH to 7.4 with 0.2 N NaOH. ES final product was sterilized by 0.2 µm filtration. Each 100 µL subcutaneous dose contained 12.5 µg ES. Pups received injections on postnatal days 7 and 10 for a total ES dose of 25 µg.

ES-Cu²⁺ Formulation & Delivery: 2X stock solution of ES-Cu²⁺ was prepared by wetting 2.9 mg complex with 10 mL 20% Captisol® solution. Slurry was sonicated for 5 min. at 30°C and continuously mixed at constant temperature for 3 hours to ensure complete dissolution. Material was filtered and stored at 4°C yielding a stock of 290 µg/mL. Final formulation involved 1:2 dilution of stock with Captisol to 145 µg/mL with adjustment of pH to 7.4 with 0.2 N NaOH. ES-Cu²⁺ final product was sterilized by 0.2 µm filtration. Each 100 µL subcutaneous dose contained 14.5 µg ES-Cu²⁺ (12.5 µg ES, 2 µg Cu²⁺). Pups received injections on postnatal days 7 and 10 for a total ES-Cu²⁺ dose of 29 µg (25 µg ES, 4 µg Cu²⁺).

HIS-Cu²⁺ Formulation & Delivery: 72 μ L of 50 mM (16.3 mg/mL) HIS-Cu²⁺ in 100 mM HEPES was added to a stirring solution of 9.93 mL 20% Captisol®. pH was adjusted to 7.4 using 0.2 N NaOH and filter sterilized. Final formulation concentration was 116.7 μ g/mL. Each 100 μ L subcutaneous dose contained 11.67 μ g HIS-Cu²⁺ (9.67 μ g Histidine, 2 μ g Cu²⁺) and 20 μ g inert Captisol®. Final HEPES concentration was negligible at 0.72 mM. Pups received injections on postnatal days 7 and 10 for a total HIS-Cu²⁺ dose of 23.3 μ g (19.34 μ g HIS, 4 μ g Cu²⁺).

All formulation work was conducted in a class II, type 2a laminar flow biosafety cabinet. All reagents were of pharmaceutical or cell culture grade. Each 100 μ L treatment contained 20 μ g inert Captisol® delivered by a 27G, 0.5cc allergy syringe with permanently attached needle (BD Biosciences, San Jose, CA).

Growth curves and Kaplan-Meier survival plot

Treated pups were weighted daily from PND 5 to PND 70 (10 weeks) and monitored for survival. The primary growth and survival study endpoints concluded on PND 70. Mice at 10 weeks were then divided into groups for behavioral, biochemical, and histological assessment. A subset of WT (n = 5), WT ES-Cu²⁺ (n = 4), and ES-Cu²⁺ mo-br (n = 11) mice were monitored without further manipulation until PND 245 (35 weeks) in order to calculate median survival. Only observations and weekly weightings were conducted for this subset between weeks 11 – 35. Growth curves and Kaplan-Meier survival plots were generated from body weight and survival data. To assess immediate

effects of interventions, additional pups were treated on PND 7 and 10 for biochemical and histological characterization of intervention effects.

Locomotor function

The following protocols were conducted utilizing WT (n = 8) and ES-Cu²⁺ treated mo-br (n = 13) mice between 10-13 weeks of age at the TAMU Rodent Preclinical Phenotyping Core (College Station, TX). Mice were randomly assessed during mid-light cycle in environmentally controlled settings. Mice were allowed to acclimate for 1 hour before activity initiation.

Open Field Assessment: Mice were placed in open field chambers (Tru Scan Activity System 2.0, Coulbourn Instruments) for 30 minutes. Test chambers and sensor plates were disinfected between runs. Animals completing assessment were temporary housed in holding cages before return to home housing. Data for each mouse was collected and averaged for three trials over a six day period of time with one rest day between assessments. Vector traces and measured parameters were exported to Excel for processing and data analysis.

Forelimb Strength Assessment: Mice were suspended by the tail and allowed to grasp a horizontally orientated metal mesh plate consisting of 1 mm diameter wire connected to a Chatillon force meter. Gentle horizontal force was applied to the mouse until maximum grip strength is achieved and the mouse released the plate. Average maximum force (N) of three trials separated by rest periods of 15 minutes were recorded in Excel for data analysis.

Rotarod Assessment: Mice were trained on the rotarod (UGO Basile model 7650) for three sessions at constant rotation of 4 rpm the week before testing. To assess motor performance, mice were placed on an accelerating rotarod (4 rpm to 40 rpm 5 min.) for a maximum of 420 seconds. Latency to fall or passive rotation (s) was recorded and averaged for three trials per session with three sessions over a six day period of time.

DigiGait™ Assessment: Gait assessment was conducted as described by Lambert et al, Behav Brain Res. 2015/PMID: 25116252 with modifications. Briefly, mice were trained for five consecutive days before data collection on the DigiGait™ system. Training sessions included three runs per day separated by a 2 hour rest interval. Mice began training at 12 cm/s which was accelerated to 24 cm/s over a two minute interval. Avoidance behavior was corrected by gentle nudging of mice with the rear bumper. Most animals exhibited rhythmic gait at 24 cm/s. Between runs, the belt and chamber were sterilized. Data collection occurred 4 days after completion of training and involved securing mice in the chamber and initializing the treadmill immediately at 24 cm/s. DigiGait™ Imaging Software was used to acquire and process video collected in 30 s intervals. Sequences containing 6-10 continuous strides were chosen for analysis in DigiGait™ Analyzer. Temporal and spatial gait parameters were collected for each assessed mouse and exported to Excel.

Necropsy & histology

WT and mo-br treatment cohorts at 2 weeks and 10 weeks were euthanized by isoflurane overdose and thoracotomy. Blood samples for serology were collected by cardiocentesis.

Histological Samples: Before organ harvest, mice were perfused through the left ventricle of the heart after severing of the right atrium with 10% neutral buffered formalin. Brains, hearts, livers, kidneys, and spleens were collected, fixed in formalin, and sent to the Texas Veterinary Medical Diagnostic Lab (College Station, TX) for analysis by a blinded pathologist. Reports and digital slides were returned for each sample set.

Brain Digital Slides: NDP Viewer was used to review sagittal sections of brain (H&E stain) in order to generate high resolution images. Percent pyknotic neurons of the CA1-3 region of the hippocampus at 40X-80X magnification were generated by counting 400 nuclei in each brain hemisphere (800 nuclei per biological replicate, n = 4 per cohort; 3200 total per cohort). Qualitative assessment of cortex and cerebellum was provided in the pathologist's report along with detailed analysis of the Purkinje cell layer of the cerebellar peduncles.

Organ Digital Slides: NDP Viewer was used to review longitudinal and cross sections of liver, kidney, heart, and spleen (H&E stain) in order to generate high resolution images. Qualitative assessment of organs was provided in the pathologist's report.

Biochemistry

WT and mo-br treatment cohorts at 2 weeks and 10 weeks were euthanized and blood collected as previously described. Before organ harvest, mice were perfused through the left ventricle of heart with normal saline. Brains, hearts, thymus, lungs, livers, spleens, and kidneys were harvested, washed, trimmed, weighted, and flash frozen with liquid nitrogen. Samples were stored at -80°C pending analysis.

Copper Measurement: Tissue and serum copper levels were measured by using a PerkinElmer DRC II inductively coupled plasma (ICP) mass spectrometer. Intact tissue samples were washed with 100 μ M EDTA-containing water, weighed, and digested with 40% nitric acid (TraceSELECT; Sigma) at 90°C for 18 h, followed by digestion with 1% hydrogen peroxide (Ultratrace analysis; Sigma) at 90°C for 4 h. Samples were diluted in ultrapure metal-free water (TraceSELECT; Sigma) and analyzed by ICP-MS. Copper standard solutions were prepared by appropriate dilutions of commercially available mixed metal standards (BDH Aristar Plus).

Immunoblotting: Tissue samples were homogenized on ice in RIPA extraction buffer (50 mM Tris (pH 7.4), 150 mM NaCl, 1% NP-40, 0.5% sodium deoxycholate, 0.1% SDS supplemented with a 1 \times cOmplete protease inhibitor cocktail (Roche, Indianapolis, IN) and centrifuged at 4°C for 15 min at 14,000 \times g to obtain a supernatant. Protein concentration of the supernatant was determined using BCA assay (Pierce BCA Protein Assay) and indicated protein (20 μ g) samples were separated by SDS-PAGE and blotted onto a polyvinylidene difluoride membrane. Membranes were treated for 1 hr in blocking buffer containing 5% nonfat milk dissolved in Tris-buffered saline with 0.1% Tween 20

(TBST-milk), followed by overnight incubation with primary antibody in TBST-milk at 4°C. Primary antibodies were used at the following dilutions: COX1, 1:5000 (14705; Abcam); ATP5A, 1: 10,000 (14748; Abcam); SOD1, 1:5000 (PA1-30195; Invitrogen).

ATP7A knockout B16 melanoma cells

The B16 melanoma cells were obtained from American Type Culture Collection (ATCC®, B16-F10 CRL-6475™). ATP7A KO CellTiter-Glo Luminescent Viability assay (Promega Cat. #G9241) cells were generated by transfecting wildtype B16 cells with a CRISPR-Cas9/GFP construct targeting Exon 16 of ATP7A [5'-CCCATGGAACCCAGTAGTGAA-3'] (Sigma-Aldrich), using Lipofectamine 2000. GFP-positive cells were isolated using a Beckman Coulter MoFlo CDP and individual clones were screened for ATP7A protein by immunofluorescence and immunoblot analyses. Cells were grown in complete medium consisting of Dulbecco's modified Eagle's medium (Life Technologies) supplemented with 10% (v/v) fetal bovine serum, 2 mM glutamine and 100 units/ml penicillin and streptomycin (Life Technologies, Carlsbad, CA) in 5% CO₂ at 37°C.

Tyrosinase Activity (Qualitative): ATP7A KO cells were treated with DMSO, 25 μ M CuCl₂, or 1 nM ES for 3 days prior to trypsinization, washing, and pelleting. Pigment content of pellet was recorded following visual inspection.

CTR1 knockout H9c2 cells.

The CTR1 KO H9c2 cells were generated as described in Soma et al. Proc Natl Acad Sci U S A (2018)/PMID 30038027. Briefly, rat H9c2 cells (ATCC®, CLR-1446™) were generated by transfecting wildtype H9c2 cells with a lentiCRISPRv2 construct targeting Exon 1 of CTR1 (Addgene Cat. #52961). Two days after transfection, cells were plated in puromycin selection media. Disruption of CTR1 was confirmed by genomic sequencing.

Oxygen consumption rate measurements: Oxygen consumption rate (OCR) measurements were carried out as previously described (Gohil et al., Nat Biotech. 2010/20160716) with minor modifications. Briefly, rat H9c2 control and CTR1 KO cardiomyocytes were treated with DMSO or 1 nM elesclomol for three days in high glucose DMEM growth media supplemented with 10% FBS (Sigma) and 1 mM sodium pyruvate (Life Technologies). The cells were then seeded in XF24-well cell culture microplates (Agilent Technologies) at 20,000 cells/well in 250 μ l of growth media with DMSO or 1 nM elesclomol and incubated at 37 °C, 5% CO₂ for ~20 h. Before the measurements were made, 525 μ l of the pre-warmed growth medium was added to each well and cells were incubated at 37 °C for 30 min. OCR measurements were carried out in intact cells using Seahorse XF24 Extracellular Flux Analyzer (Agilent Technologies). Mix, wait and measure durations were set to 2, 2 and 2?min, respectively. For the mitochondrial stress test, oligomycin, carbonyl cyanide 3-cholorophenylhydrazone (CCCP) and antimycin A were sequentially injected to achieve final concentrations of 0.5, 10 and 1? μ M, respectively. Immediately after the assay, the cell culture microplates were

washed thrice with 500 μ l PBS and 25 μ l RIPA lysis buffer (25mM Tris. HCl pH 7.6, 150mM NaCl, 1% NP-40, 1% sodium deoxycholate, 0.1% SDS) was added to each well and incubated on ice for 30 min. Protein concentration in each well was measured by BCA assay (Thermo Scientific) and the OCR values were normalized to protein content.

ATP measurement: Rat H9c2 control and Ctr1 KO cardiomyocytes were treated for 3 days with DMSO or 1 nM elesclomol in No glucose DMEM media supplemented with 10 mM galactose, 10% FBS (Sigma) and 1 mM sodium pyruvate (Life Technologies) were seeded in 96 well plates at 5,000 cells/well. After ~20 h of growth ATP levels were assayed by CellTiter-Glo Luminescent Viability assay (Promega Cat. #9241) according to the manufacturer's instructions.

Statistical analysis and software

Statistical analysis was conducted using XLSTAT, GraphPad Prism, and Excel. One-way ANOVA/Welch ANOVA with post hoc Tukey's HSD test and t-test were used to determine significance among cohorts unless otherwise specified. PKSolver was used to analyze PK data and generate models. GraphPad Prism 8 was used to generate growth curves, Kaplan-Meier plot, and preliminary figures. ImageJ was used to quantitatively analyze Western blots. Final figures were processed in Adobe Illustrator.

RESULTS

ES restores mitochondrial function in Ctr1 Knockout H9c2 Cells and Mice

We measured oxygen consumption rate (OCR), an indication of electron transport

activity, and ATP levels in the Cu importer *Ctr1* knockout (KO) H9c2 rat cardiomyocytes. *Ctr1* KO H9c2 cells exhibited significant reduction in basal OCR and ATP levels. Preincubation with 1 nM ES restored OCR to 103% (+34%) of WT (2.5 vs $3.7 \mu\text{M}\cdot\text{min}^{-1}\cdot\mu\text{g protein}^{-1}$, $p < 0.001$) (Fig. S1A). Similarly, ES treatment increased ATP levels compared to the *Ctr1* KO vehicle (0.74 vs 1.01 , $p < 0.001$) (Fig. S1B).

Loss of CTR1 results in severe cellular Cu deficiency in mice. *Ctr1*^{-/-} mice demonstrate lethality in utero (19). The cardiac-specific *Ctr1* knockout (KO) mouse (20), exhibits growth retardation, severe hypertrophic cardiomyopathy due to cardiac muscle CcO dysfunction, and death around postnatal day (PND) 12. To assess the ability of ES to escort Cu²⁺ through CTR1-deficient cardiac cellular membranes, we administered subcutaneous ES at $10 \text{ mg}\cdot\text{kg}^{-1}$. WT mice tolerated ES injections well with favorable tolerability and pharmacokinetics (Table S1) (Fig. S2). We observed a 100% 26 day survival rate in ES-treated mice whereas those receiving vehicle died between PND 8–12 (Fig. 1A, B). Growth of ES mice was restored to WT pattern with no significant deviation from either WT vehicle or WT ES-treated groups (Fig. 1C) (Fig. S3A).

ES mice demonstrated normalization of total body, heart, and spleen weights at PND 10 (Fig. 1D, E) (Fig. S3B-D). Cardiac histopathology at PND 10 of vehicle treated KO mice showed pronounced hypertrophy characterized by increased cell area as compared to WT tissue samples (186 vs $87 \mu\text{m}^2$, $p < 0.01$) (Fig. S3E, F). ES treatment ameliorated severe cardiac pathology with a partial reduction in hypertrophy ($119 \mu\text{m}^2$, $p < 0.01$) (Fig. S3E, F). Cardiac [Cu] increased with ES treatment from a vehicle KO level

of 34% to 55% (1.6 vs 2.6 $\mu\text{g}\cdot\text{g}^{-1}$, $p = 0.04$) (Fig. 1F). The 21% increase in cardiac [Cu] resulted in a 28% increase in COX1, the Cu-containing subunit of CcO (*1*) (Fig. 1G, H). SOD1, a cuproenzyme highly resistant to depletion (*21*), remained unchanged (Fig. S4).

ES Alone Does Not Rescue Mottled-Brindled Mice

The *mottled-brindled* (*mo-br*) mouse phenotypically recapitulates Menkes disease (*22*). *Mo-br* mice possess a 6-bp deletion in exon 11 of the mouse *ATP7A* gene resulting in an in-frame deletion of Leu799 and Ala800. This deletion results in little residual Cu transporting function with severe disease phenotypes including hypopigmentation, kinky whiskers, growth delay, neurological abnormalities, seizures, and death around PND 14. As with most Menkes patients, the *mo-br* mouse shows little response to treatment with hydrophilic Cu complexes alone (*23-25*).

In preliminary studies, we administered ES at 10 $\text{mg}\cdot\text{kg}^{-1}$ body weight. Unlike the cardiac *Ctr1* KO mice, this pilot study demonstrated no enhanced survival amongst treated *mo-br* males. This was likely because *mo-br* mice were too deficient in systemic Cu to benefit from ES alone whereas the cardiac *Ctr1* KO mouse possess an elevated serum Cu pool capable of ES-mediated redistribution to deficient cardiomyocytes (*20*). We hypothesized that by pre-loading ES with Cu^{2+} , we would address the systemic Cu deficiency and ATP7A-mediated defective transport.

ES-Cu²⁺ Complex Rescues mottled-brindled Mice

Menkes disease is characterized by severe neurodegeneration, therefore any

successful treatment must involve a drug that facilitates Cu delivery across the blood-brain barrier or blood-cerebral spinal fluid barrier (9, 10, 14). Brain pharmacokinetic studies on PND 7 mice demonstrated high levels of ES in the brain at $201.3 \pm 41.7 \text{ ng}\cdot\text{mg}^{-1}$ (Fig. S5A) whereas adult exposure, though still significant, was about 25-fold lower at $7.8 \pm 5.0 \text{ ng}\cdot\text{mg}^{-1}$ (Fig. S5B).

We next administered ES-Cu²⁺ at $3.625 \text{ mg}\cdot\text{kg}^{-1}$ per dose by subcutaneous injection on PND 7 and 10. The total dose of Cu approximated the total amount of Cu ($4 \mu\text{g}$) in a 4 g WT mouse (26). Additional *mo-br* cohorts included vehicle, ES only, and copper histidine (HIS-Cu²⁺) formulated with an equivalent dose of Cu as compared to the ES-Cu²⁺ cohort (Table 1). We selected HIS-Cu²⁺ as a control because of the drug's investigational status for Menkes disease (14). ES-Cu²⁺ was well tolerated and exhibited favorable pharmacokinetics (Table S2-4) (Fig. S6-S7).

Within 24 hours, we observed pigment production in ES-Cu²⁺ treated mice in the immediate vicinity of the injection site (Fig. 2A-C) (Fig. S8A). Pigment production indicated increased activity of the secretory pathway cuproenzyme tyrosinase. This was in agreement with the in vitro assessment of an *ATP7A* KO B16 melanoma cell line which showed that 1 nM ES was able to partially rescue tyrosinase activity (Fig. S8B). Because tyrosinase requires the action of *ATP7A* for Cu import into the Golgi complex (27), our findings were unexpected and suggest that ES-Cu²⁺ was delivering Cu to cuproenzymes metalated in the Golgi complex. We also observed that whisker appearance improved from bushy, highly kinked clumps to near-normal by PND 70 in only the ES-Cu²⁺ cohort (Fig.

S8C)—indicating improved sulfhydryl oxidase activity (28).

Mo-br vehicle, ES only, and HIS-Cu²⁺ cohorts developed seizures beginning around PND 11 (Video S1). Seizures increased in severity, with subsequent death of all individuals in these groups between PND 14-21. We only observed a negligible survival advantage for HIS-Cu²⁺ over vehicle alone (Table 1). ES-Cu²⁺ treated *mo-br* adult mice did not have seizures and exhibited similar body size to that of WT siblings (Fig. 2D, E) (Video S2). ES-Cu²⁺ increased the survival of *mo-br* mice and successfully rescued 82% of animals at 10 weeks of age with a median survival of 203 days ($p < 0.01$, Log-Rank) (Fig. 2F) (Fig. S8D) (Table 1). After treatment, ES-Cu²⁺ *mo-br* mice experienced accelerated growth and near normal body weight by week 10 (Fig. 2G) (Fig. S8E). Histological examination of the livers of WT vehicle and both ES-Cu²⁺ treated WT and *mo-br* mice demonstrated no pathological changes associated with drug exposure (Fig. S9).

Neuromotor Assessment of ES-Cu²⁺ Rescue

Ten week old *mo-br* mice were evaluated by phenotype and neuromotor functional tests. ES-Cu²⁺ treated *mo-br* mice revealed hypopigmentation but no other gross abnormalities upon observation (Fig. 2D, E). On a forelimb grip strength test using a Chatillon force apparatus, ES-Cu²⁺ treated *mo-br* mice possessed 73% grip strength compared to WT animals (0.94 vs 1.29 N, $p < 0.01$) (Fig 3A). On the accelerating rotarod, a test of endurance and motor coordination, ES-Cu²⁺ *mo-br* mice exhibited average latency to fall time of 222 s compared to 379 s ($p < 0.01$) for WT (Fig 3B). On the gait

treadmill, overall ataxic indices were statistically insignificant for both pelvic and shoulder girdles compared to WT (Fig. 3C) (Table S5) (Video S3, S4). In the open field, *mo-br* mice demonstrated 35% decreased movement time, 24% increased rest time, and traveled 60% of total distance as compared to WT ($p < 0.01$) (Fig. 3D-F).

Brain Histology and Biochemical Markers of ES-Cu²⁺ Therapy

Brain sections of vehicle and HIS-Cu²⁺ treated mice at 2 weeks of age showed marked, diffuse neurodegeneration of cortical and hippocampal neurons (Fig. 4A) (Fig. S10A). In the hippocampus, necrotic pyramidal neurons represented 10.5% of 3200 counted cells in vehicle and 4.9% in HIS-Cu²⁺ *mo-br* mice. ES-Cu²⁺ preserved cortical and hippocampal neurons with hippocampal regions showing no signs of necrosis as characterized by pyknotic nuclei (Fig. 4A). The Purkinje neuron layer in the cerebellum was also preserved. (Fig. S10B). At 10 weeks of age, brain structures were preserved with no distinct differences between WT and ES-Cu²⁺ treated *mo-br* mice (Fig. 4B) (Fig. S11A-C).

Two week old mice treated with ES-Cu²⁺ showed normalized serum [Cu] (Fig. 5A) with increased brain [Cu] from the vehicle baseline of 22% of WT, to 41% (0.45 vs 0.82 $\mu\text{g}\cdot\text{g}^{-1}$, $p < 0.01$) compared to 24% with HIS-Cu²⁺ (0.48 $\mu\text{g}\cdot\text{g}^{-1}$) (Fig. 5B). ES-Cu²⁺ proved superior to HIS-Cu²⁺ at delivering Cu to brain tissue ($p < 0.01$). Necropsy at 2 weeks showed significant decrease in total brain mass in *mo-br* animals treated with vehicle and HIS-Cu²⁺ (-16% and -12%) (Fig. 5C) (Table S6, S7). ES-Cu²⁺ normalized

brain mass comparable to WT littermates (< 2% difference between WT and *mo-br* ES-Cu²⁺ cohorts) (Fig. 5C).

Mitochondrial COX1 levels exhibited a 14% improvement with ES-Cu²⁺ intervention (30% vs 16%, $p = 0.03$) (Fig. 5D, E). We did not observe any significant correction in COX1 levels in vehicle or HIS-Cu²⁺ treated mice (17%, $p = 0.99$) (Fig. 5D, E). Though overall brain [Cu] was about 2-fold lower in ES-Cu²⁺ cohort as compared to WT (0.82 vs 1.95 $\mu\text{g}\cdot\text{g}^{-1}$), the mitochondria-specific delivery mechanism of ES-Cu²⁺ could explain the degree of COX1 metalation. We also observed significant improvements in [Cu] and COX1 levels in hearts of ES-Cu²⁺ treated *mo-br* mice both at PND14 and PND70 (Fig. S12). SOD1 levels remained unchanged (Fig. S13).

At 10 weeks, COX1 levels in ES-Cu²⁺ mice were 42% of WT (Fig. 5F-G). Serum [Cu] reverted to earlier established *mo-br* baseline of 28% of WT (0.48 vs 1.73 $\mu\text{g}\cdot\text{mL}^{-1}$) (Fig. 5H). In the brain, Cu levels declined from 41% to 34% of WT (1.57 vs 4.64 $\mu\text{g}\cdot\text{g}^{-1}$) (Fig. 5I) but brain weights remained indistinguishable (0.448 vs 0.432 g, $p = 0.23$) (Fig. 5J) (Table S6).

Identification of elesclomol as a potential therapeutic agent

In a previous publication, we screened a diverse set of small molecules that bind copper for their ability to rescue a *Saccharomyces cerevisiae* strain deficient in electron transport due to deletion of *coa6* (*coa6* Δ) (16). Coa6 is an assembly factor for CcO and a component of the mitochondrial copper relay system utilized to metalate the CcO subunit

Cox2 (1). Elesclomol (ES) restored near-wildtype (WT) growth, oxygen consumption rate, and CcO function with an ED50 of 0.8 nM; representing the most potent molecule identified in our *coa6Δ* functional complementation assay (16). The results of this initial publication served as an in vitro groundwork and justification for the transition to vertebrate animal models of hereditary copper deficiency disorders.

Chemical properties and mechanism

ES, a substituted bis(thio-hydrazide) amide, is a small molecule with a molecular weight of $400.5 \text{ g}\cdot\text{mol}^{-1}$. It strongly binds Cu^{2+} in a 1:1 stoichiometric ratio (30). The Cu^{2+} ion coordinates with four atoms of ES; forming two S – Cu and N – Cu interactions that result in an approximately square planar geometry capable of permeating lipid bilayer membranes. ES escorts Cu^{2+} from outside of the cell into the mitochondrial matrix by traversing three membrane systems (plasma, outer mitochondrial, and inner mitochondrial) where it is liberated from the complex by reduction of the Cu^{2+} cupric ion to the cuprous form, Cu^{1+} (30-32). Mechanistically this occurs by the action of the mitochondrial cytochrome p450 enzyme ferredoxin (FDX1) (33). In yeast and mammalian cell lines, liberated Cu^{1+} is then bound by metallochaperones of the copper relay system and used to metalate Cox2, resulting in restoration of CcO function (16).

Tolerability and pharmacokinetics of elesclomol

Adult C57BL/6 mice given ES at $25 \text{ mg}\cdot\text{kg}^{-1}$ for five consecutive days via the subcutaneous route experienced no signs of acute toxicity or weight loss. ES formulated in 0.5% Methocel™ (w/v) aqueous vehicle performed well as a solvating system (Table S1). The pharmacokinetic profile of ES was determined by administering a $10 \text{ mg}\cdot\text{kg}^{-1}$ subcutaneous (SQ) dose to adult mice followed by serial blood sampling and quantification by LC-MS. We constructed a 1-compartment PK model using PKSolver and determined the total exposure ($\text{AUC}_{0-\infty}$) of subcutaneous ES was $300.5 \text{ ng}\cdot\text{mL}^{-1}\cdot\text{hr}^{-1}$ with a C_{max} of $529.7 \text{ ng}\cdot\text{mL}^{-1}$ and $t_{1/2}$ of 3 min. (Fig S2).

Tolerability and pharmacokinetics of elesclomol-Cu²⁺ complex

In order to solubilize this rather lipophilic complex, we formulated ES-Cu²⁺ in 20% Captisol® aqueous vehicle (Fig. S6). Single bolus subcutaneous injections of $7.25 \text{ mg}\cdot\text{kg}^{-1}$ ES-Cu²⁺ showed no overt signs of acute toxicity. Mice retained body weight as compared to control animals (Table S2). Compartmental analysis of the PK profile showed that the ES-Cu²⁺ complex exhibits nonlinear PK (Fig. S7A, B). After initial high plasma C_{max} of $197.6 \text{ ng}\cdot\text{mL}^{-1}$ at 22.8 min, subcutaneous ES-Cu²⁺ exhibits rapid elimination from the central compartment ($t_{1/2 \alpha}$ of 54.6 min) and slow elimination from the peripheral compartment ($t_{1/2 \beta}$ of 18.8 hr) (Fig. S7C).

Peripheral tissue levels exhibited good ES-Cu²⁺ penetrance ($5.3 \text{ ng}\cdot\text{mL}^{-1}$) indicating tissue partitioning of the metalated complex (Fig. S7C). The lipophilic nature

of the preformed complex explains the greater tissue penetrance and slower elimination as compared to ES alone. Formation of ES-Cu²⁺ in vivo is rate-limited by the availability of labile copper and provides an explanation for the initial lack of response in mo-br mice treated with ES alone. (31, 32). Subcutaneous ES-Cu²⁺ complex is 72% bioavailable (Fig. S7C).

In a previous publication, we screened a diverse set of small molecules that bind copper for their ability to rescue a *Saccharomyces cerevisiae* strain deficient in electron transport due to deletion of *coa6* (*coa6*[?]) (16). *Coa6* is an assembly factor for CcO and a component of the mitochondrial copper relay system utilized to metalate the CcO subunit Cox2 (1). Elesclomol (ES) restored near-wildtype (WT) growth, oxygen consumption rate, and CcO function with an ED₅₀ of 0.8 nM; representing the most potent molecule identified in our *coa6*[?] functional complementation assay (16). The results of this initial publication served as an in vitro groundwork and justification for the transition to vertebrate animal models of hereditary copper deficiency disorders.

ES restores mitochondrial function in Ctr1 Knockout H9c2 Cells and Mice

We measured oxygen consumption rate (OCR), an indication of electron transport activity, and ATP levels in the Cu importer *Ctrl1* knockout (KO) H9c2 rat cardiomyocytes. *Ctrl1* KO H9c2 cells exhibited significant reduction in basal OCR and ATP levels. Preincubation with 1 nM ES restored OCR to 103% (+34%) of WT (2.5 vs 3.7 pM·min⁻¹·μg protein⁻¹, *p* < 0.001) (Fig. S1A). Similarly, ES treatment increased ATP levels compared to the *Ctrl1* KO vehicle (0.74 vs 1.01, *p* < 0.001) (Fig. S1B).

We measured oxygen consumption rate (OCR), an indication of electron transport activity, and ATP levels in the Cu importer Ctr1 knockout (KO) H9c2 rat cardiomyocytes. Ctr1 KO H9c2 cells exhibited significant reduction in basal OCR and ATP levels. Preincubation with 1 nM ES restored OCR to 103% (+34%) of WT (2.5 vs 3.7 $\mu\text{M}\cdot\text{min}^{-1}\cdot\mu\text{g protein}^{-1}$, $p < 0.001$) (Fig. S1A). Similarly, ES treatment increased ATP levels compared to the Ctr1 KO vehicle (0.74 vs 1.01 , $p < 0.001$) (Fig. S1B).

Loss of CTR1 results in severe cellular Cu deficiency in mice. Ctr1^{-/-} mice demonstrate lethality in utero (19). The cardiac-specific Ctr1 knockout (KO) mouse (20), exhibits growth retardation, severe hypertrophic cardiomyopathy due to cardiac muscle CcO dysfunction, and death around postnatal day (PND) 12. To assess the ability of ES to escort Cu²⁺ through CTR1-deficient cardiac cellular membranes, we administered subcutaneous ES at 10 $\text{mg}\cdot\text{kg}^{-1}$. WT mice tolerated ES injections well with favorable tolerability and pharmacokinetics (Table S1) (Fig. S2). We observed a 100% 26 day survival rate in ES-treated mice whereas those receiving vehicle died between PND 8–12 (Fig. 1A, B). Growth of ES mice was restored to WT pattern with no significant deviation from either WT vehicle or WT ES-treated groups (Fig. 1C) (Fig. S3A).

ES mice demonstrated normalization of total body, heart, and spleen weights at PND 10 (Fig. 1D, E) (Fig. S3B-D). Cardiac histopathology at PND 10 of vehicle treated KO mice showed pronounced hypertrophy characterized by increased cell area as compared to WT tissue samples (186 vs 87 μm^2 , $p < 0.01$) (Fig. S3E, F). ES treatment ameliorated severe cardiac pathology with a partial reduction in hypertrophy (119 μm^2 , $p < 0.01$) (Fig. S3E, F). Cardiac [Cu] increased with ES treatment from a vehicle KO level

of 34% to 55% (1.6 vs 2.6 $\mu\text{g}\cdot\text{g}^{-1}$, $p = 0.04$) (Fig. 1F). The 21% increase in cardiac [Cu] resulted in a 28% increase in COX1, the Cu-containing subunit of CcO (1) (Fig. 1G, H). SOD1, a cuproenzyme highly resistant to depletion (21), remained unchanged (Fig. S4).

ES Alone Does Not Rescue Mottled-Brindled Mice

The mottled-brindled (mo-br) mouse phenotypically recapitulates Menkes disease (22). Mo-br mice possess a 6-bp deletion in exon 11 of the mouse *Atp7A* gene resulting in an in-frame deletion of Leu799 and Ala800. This deletion results in little residual Cu transporting function with severe disease phenotypes including hypopigmentation, kinky whiskers, growth delay, neurological abnormalities, seizures, and death around PND 14. As with most Menkes patients, the mo-br mouse shows little response to treatment with hydrophilic Cu complexes alone (23-25).

In preliminary studies, we administered ES at 10 $\text{mg}\cdot\text{kg}^{-1}$ body weight. Unlike the cardiac *Ctrl* KO mice, this pilot study demonstrated no enhanced survival amongst treated mo-br males. This was likely because mo-br mice were too deficient in systemic Cu to benefit from ES alone whereas the cardiac *Ctrl* KO mouse possess an elevated serum Cu pool capable of ES-mediated redistribution to deficient cardiomyocytes (20). We hypothesized that by pre-loading ES with Cu^{2+} , we would address the systemic Cu deficiency and *ATP7A*-mediated defective transport.

ES- Cu²⁺ Complex Rescues mottled-brindled Mice

We next administered ES-Cu²⁺ at 3.625 mg·kg⁻¹ per dose by subcutaneous injection on PND 7 and 10. The total dose of Cu approximated the total amount of Cu (4 μg) in a 4 g WT mouse (26). Additional mo-br cohorts included vehicle, ES only, and copper histidine (HIS-Cu²⁺) formulated with an equivalent dose of Cu as compared to the ES-Cu²⁺ cohort (Table 1). We selected HIS-Cu²⁺ as a control because of the drug's investigational status for Menkes disease (14). ES-Cu²⁺ was well tolerated and exhibited favorable pharmacokinetics (Table S2-4) (Fig. S6-S7).

Within 24 hours, we observed pigment production in ES-Cu²⁺ treated mice in the immediate vicinity of the injection site (Fig. 2A-C) (Fig. S8A). Pigment production indicated increased activity of the secretory pathway cuproenzyme tyrosinase. This was in agreement with the in vitro assessment of an ATP7A KO B16 melanoma cell line which showed that 1 nM ES was able to partially rescue tyrosinase activity (Fig. S8B). Because tyrosinase requires the action of ATP7A for Cu import into the Golgi complex (27), our findings were unexpected and suggest that ES-Cu²⁺ was delivering Cu to cuproenzymes metalated in the Golgi. We also observed that whisker appearance improved from bushy, highly kinked clumps to near-normal by PND 70 in only the ES-Cu²⁺ cohort (Fig. S8C)—indicating improved sulfhydryl oxidase activity (28).

Mo-br vehicle, ES only, and HIS-Cu²⁺ cohorts developed seizures beginning around PND 11 (Video S1). Seizures increased in severity, with subsequent death of all individuals in these groups between PND 14-21. We only observed a negligible survival advantage for HIS-Cu²⁺ over vehicle alone (Table 1). ES-Cu²⁺ treated mo-br adult mice

did not have seizures and exhibited similar body size to that of WT siblings (Fig. 2D, E) (Video S2). ES-Cu²⁺ increased the survival of mo-br mice and successfully rescued 82% of animals at 10 weeks of age with a median survival of 203 days ($p < 0.01$, Log-Rank) (Fig. 2F) (Fig. S8D) (Table 1). After treatment, ES-Cu²⁺ mo-br mice experienced accelerated growth and near normal body weight by week 10 (Fig. 2G) (Fig. S8E). Histological examination of the livers of WT vehicle and both ES-Cu²⁺ treated WT and mo-br mice demonstrated no pathological changes associated with drug exposure (Fig. S9).

Neuromotor Assessment of ES-Cu²⁺ Rescue

Ten week old mo-br mice were evaluated by phenotype and neuromotor functional tests. ES-Cu²⁺ treated mo-br mice revealed hypopigmentation but no other gross abnormalities upon observation (Fig. 2D, E). On a forelimb grip strength test using a Chatillon force apparatus, ES-Cu²⁺ treated mo-br mice possessed 73% grip strength compared to WT animals (0.94 vs 1.29 N, $p < 0.01$) (Fig 3A). On the accelerating rotarod, a test of endurance and motor coordination, ES-Cu²⁺ mo-br mice exhibited average latency to fall time of 222 s compared to 379 s ($p < 0.01$) for WT (Fig 3B). On the gait treadmill, overall ataxic indices were statistically insignificant for both pelvic and shoulder girdles compared to WT (Fig. 3C) (Table S5) (Video S3, S4). In the open field, mo-br mice demonstrated 35% decreased movement time, 24% increased rest time, and traveled 60% of total distance as compared to WT ($p < 0.01$) (Fig. 3D-F).

Brain Histology and Biochemical Markers of ES-Cu²⁺ Therapy

Brain sections of vehicle and HIS-Cu²⁺ treated mice at 2 weeks of age showed marked, diffuse neurodegeneration of cortical and hippocampal neurons (Fig. 4A) (Fig. S10A). In the hippocampus, necrotic pyramidal neurons represented 10.5% of 3200 counted cells in vehicle and 4.9% in HIS-Cu²⁺ mo-br mice. ES-Cu²⁺ preserved cortical and hippocampal neurons with hippocampal regions showing no signs of necrosis as characterized by pyknotic nuclei (Fig. 4A). The Purkinje neuron layer in the cerebellum was also preserved. (Fig. S10B). At 10 weeks of age, brain structures were preserved with no distinct differences between WT and ES-Cu²⁺ treated mo-br mice (Fig. 4B) (Fig. S11A-C).

Two week old mice treated with ES-Cu²⁺ showed normalized serum [Cu] (Fig. 5A) with increased brain [Cu] from the vehicle baseline of 22% of WT, to 41% (0.45 vs 0.82 $\mu\text{g}\cdot\text{g}^{-1}$, $p < 0.01$) compared to 24% with HIS-Cu²⁺ (0.48 $\mu\text{g}\cdot\text{g}^{-1}$) (Fig. 5B). ES-Cu²⁺ proved superior to HIS-Cu²⁺ at delivering Cu to brain tissue ($p < 0.01$). Necropsy at 2 weeks showed significant decrease in total brain mass in mo-br animals treated with vehicle and HIS-Cu²⁺ (-16% and -12%) (Fig. 5C) (Table S6, S7). ES-Cu²⁺ normalized brain mass comparable to WT littermates (< 2% difference between WT and mo-br ES-Cu²⁺ cohorts) (Fig. 5C).

Mitochondrial COX1 levels exhibited a 14% improvement with ES-Cu²⁺ intervention (30% vs 16%, $p = 0.03$) (Fig. 5D, E). We did not observe any significant correction in COX1 levels in vehicle or HIS-Cu²⁺ treated mice (17%, $p = 0.99$) (Fig. 5D, E). Though overall brain [Cu] was about 2-fold lower in ES-Cu²⁺ cohort as compared to

WT (0.82 vs 1.95 $\mu\text{g}\cdot\text{g}^{-1}$), the mitochondria-specific delivery mechanism of ES-Cu²⁺ could explain the degree of COX1 metalation. We also observed significant improvements in [Cu] and COX1 levels in hearts of ES-Cu²⁺ treated *mo-br* mice both at PND14 and PND70 (Fig. S12). SOD1 levels remained unchanged (Fig. S13).

At 10 weeks, COX1 levels in ES-Cu²⁺ mice was 42% of WT (Fig. 5F-G). Serum [Cu] reverted to earlier established *mo-br* baseline of 28% of WT (0.48 vs 1.73 $\mu\text{g}\cdot\text{mL}^{-1}$) (Fig. 5H). In the brain, Cu levels declined from 41% to 34% of WT (1.57 vs 4.64 $\mu\text{g}\cdot\text{g}^{-1}$) (Fig. 5I) but brain weights remained indistinguishable (0.448 vs 0.432 g, $p = 0.23$) (Fig. 5J) (Table S6).

DISCUSSION

While deficiencies in Cu transport and processing adversely affects numerous important biological pathways, the most profound pathological changes occur owing to perturbation of the electron transport chain (5, 6). Specifically, CcO requires Cu for assembly and catalytic activity of two subunits COX1 and COX2 (1). CcO dysfunction secondary to Cu deficiency results in cardiomyopathy, neurodegeneration, and premature death (13, 14). ES at relatively low dose, stopped early mortality, and conferred near normal cardiac and brain histology while improving COX1 abundance in Cu deficient cardiac-specific *Ctrl* KO and *mo-br* mice (29).

In the cardiac *Ctrl* KO mouse, affected animals possess elevated serum [Cu] (20); allowing for in vivo ES-Cu²⁺ complex formation and redistribution of Cu across CTR1-deficient cardiomyocyte membranes to mitochondria for metalation of CcO without

supplementation of exogenous Cu. ES treatment completely reversed the delayed growth and slowed disease progression in these mice. ES treated mice exhibited improved survival at PND 26. Heart COX1 levels improved from 34% baseline to 66% (+28%) with a corresponding normalization of heart weight and reduced cardiomyocyte area despite only modest improvement in total tissue Cu levels.

HIS-Cu²⁺ clinical trials for Menkes disease have shown mixed results. While there were some improvements in survival and clinical markers, it was primarily for a subset of patients with mutations that display residual ATP7A activity (14, 25). The *mo-br* mouse, possessing little residual transporter functionality (22), only marginally benefits from HIS-Cu²⁺ therapy. In contrast, ES-Cu²⁺ significantly improves total brain tissue [Cu] levels compared to HIS-Cu²⁺ with improved outcomes for survival, restoration of growth, preservation of neurological structures, tissue Cu delivery, and COX1 abundance. Two doses of ES-Cu²⁺, equaling approximately 4 μ g of Cu by PND 10 rescued *mo-br* males and improved median survival from 14 to 203 days.

The 14% improvement in brain COX1 level in two week old mice sufficiently preserved key neurological structures, such as cortical and hippocampal neurons. Preservation of brain structures and COX1 persisted past the two week assessment. At ten weeks of age, the ES-Cu²⁺ treated *mo-br* mice demonstrated normal brain structures and increased COX1 metalation with only small defects in gross neuromotor function as determined by open field, rotarod, grip strength, and gait treadmill.

Our in vivo results indicate the mechanism of ES-mediated Cu relocalization may

not be limited to the mitochondria. Morphological changes in fur pigmentation and whisker structure indicate improvement in the secretory pathway cuproenzymes tyrosinase and sulfhydryl oxidase, enzymes whose metalation requires ATP7A activity in the Golgi complex. Partial improvement in other secretory pathway cuproenzymes, such as dopamine- β -hydroxylase and lysyl oxidase, could further explain the beneficial effects given the profound deficiency of most Cu-utilizing systems associated with Menkes disease.

Significance in Treating Human Disease and Impending Effective Menkes Therapy

With current technology and the rare occurrence of Menkes syndrome, prenatal testing of all infants is not done. A mother may find through the birth of a child, that she is a carrier of mutant *ATP7A*. As newer technology such as those kits used for affordable genetic screening for ancestry and disease becomes cheaper and more common place, it is feasible that mothers will know they are a carrier and be able to perform prenatal or newborn sequencing to test for Menkes syndrome in the child. Without the modern significant advances in genomic sequencing, a child would be identified by phenotype with significant neurological damage. As this research found, two treatments in the first 10 days of life were necessary, but effective, to promote proper neurological development despite some phenotypes still being visible in external pigmentation.

Identifying Menkes syndrome as early as possible is critical, but only one-half of the solution. The remaining hurdle is restoring copper homeostasis. With the improvements of ES-Cu²⁺ over standard HIS-Cu²⁺ treatment providing months of life to

treated mice, the potential for humans is exciting. If Es-Cu²⁺ treatment is as successful in humans as it is in mice, affected persons could live to older middle age or for a full lifespan. Ultimately this treatment is a stop gap therapy until genetic modification to remove genetic diseases from embryos becomes commonplace.

ACKNOWLEDGMENTS

We thank H. McGuire and R. McAdams for rodent husbandry and tissue processing assistance; P. Trivedi for optimizing mo-br genotyping protocol; C. Klemashevich and S. Shankar from Texas A&M University Integrated Metabolomics Analysis Core (IMAC) for mass spectroscopy technical expertise. We thank M. Anguiano from Texas Veterinary Medicine Diagnostics Lab (TVMDL) for brain histology technical help. **Funding:** This work was supported by the Chancellor's Research Initiative, Texas A&M University System (J.C.S.), Welch Foundation grants A-0015 (J.C.S), A-1810 (V.M.G.) and National Institutes of Health grants R01GM111672 (V.M.G.), R01DK110195 (B.E.K). **Author Contributions:** L.M.G. established mo-br rodent colony, husbandry/breeding, drug formulations, PK/Tox experiments, developed interventional protocols, efficacy studies, behavioral studies, and wrote the manuscript. A.S., T.C.S., S.S., M.Z., H.F.G, B.L., and E.N. assisted in husbandry and biological sample processing for PK/Tox, histology, and biochemical experiments. S.S. and M.Z. performed tissue copper, and biochemical studies. A.A. and C.D.V. synthesized ES-Cu²⁺ complex. V.S. and M.J.P. developed the ATP7A^{-/-} B16 melanoma cell line and provided technical expertise. F.R.L. performed histopathology sectioning, generation of digital slide sets, and analysis. S.Y. and B.E.K. established cardiac Ctr1 KO rodent colony, husbandry/breeding, efficacy studies, histology, and biochemical studies. V.M.G. and J.C.S. developed the concept of ES drug therapy for hereditary copper disorders, provided administrative and technical expertise, undertook data analysis, and helped write the manuscript. **Thomas Snavely (T.C.S.)** Alongside L.M.G and A.S., established initial

murine breeding colony for embryo freeze-back, trained and supervised technicians maintaining the colony, performed organ harvesting for M.S. and histology, carried out phenotypic characterization and monitored long-term surviving male mice. **Competing Interests:** L.M.G, J.C.S, S.S. and V.M.G. are inventors on patent applications PCT/US2019/041571 submitted by Texas A&M University that covers Compositions for the Treatment of Copper Deficiency and Methods of Use.

REFERENCES

1. B. E. Kim, T. Nevitt, D. J. Thiele, Mechanisms for copper acquisition, distribution and regulation. *Nat Chem Biol.* 4(3), 176-185 (2008).
2. L. M. Gaetke, H. S. Chow-Johnson, C. K. Chow, Copper: toxicological relevance and mechanisms. *Arch Toxicol.* 88(11), 1929-1938 (2014).
3. E. D. Harris, Cellular copper transport and metabolism. *Annu Rev Nutr.* 20(1), 291-310 (2000).
4. N. J. Robinson, D. R. Winge, Copper metallochaperones. *Annu Rev Biochem.* 79, 537-562 (2010).
5. I. Valnot et al., Mutations of the SCO1 gene in mitochondrial cytochrome c oxidase deficiency with neonatal onset hepatic failure and encephalopathy. *Am J Hum Genet.* 67(5), 1104-1109 (2000).
6. L. C. Papadopoulou et al., Fatal infantile cardioencephalomyopathy with COX deficiency and mutations in SCO2, a COX assembly gene. *Nat Genet.* 23(3), 333-337 (1999).
7. S. G. Kaler, Inborn errors of copper metabolism. *Handb Clin Neurol.* 113, 1745-1754 (2013).
8. H. Ohrvik, D. J. Thiele, How copper traverses cellular membranes through the mammalian copper transporter, Ctr1. *Ann N Y Acad Sci.* 1314, 32-41 (2014).
9. B. S. Choi, W. Zheng, Copper transport to the brain by the blood-brain barrier and blood-CSF-barrier. *Brain Res.* 1248, 14-21 (2009).

10. S. G. Kaler, ATP7A-related copper transport diseases: emerging concepts and future trends. *Nat Rev Neurol.* 7(1), 15-29 (2011).
11. H. Kodama, Y. Murata, M. Kobayashi, Clinical manifestations and treatment of Menkes disease and its variants. *Pediatr Int.* 41(4), 423-429 (1999).
12. M. Sparaco, A. Hirano, M. Hirano, S. DiMauro, E. Bonilla, Cytochrome *c* oxidase deficiency and neuronal involvement in Menkes' kinky hair disease: immunohistochemical study. *Brain Pathol.* 3(4), 349-354 (1993).
13. S. Zlatic et al., Molecular basis of neurodegeneration and neurodevelopment defects in Menkes Disease. *Neurobiol Dis.* 81, 154-161 (2015).
14. S. G. Kaler et al., Neonatal diagnosis and treatment of Menkes disease. *N Engl J Med.* 358(6), 605-614 (2008).
15. J. H. Kim et al., Novel mutations and clinical outcomes of copper-histidine therapy in Menkes disease patients. *Metab Brain Dis.* 30(1), 75-81 (2015)
16. S. Soma et al., Elesclomol restores mitochondrial function in genetic models of copper deficiency. *Proc Natl Acad Sci U S A.* 115(32), 8161-8166 (2018).
17. A. S. Grillo et al., Restored iron transport by a small molecule promotes absorption and hemoglobinization in animals. *Science* 356(6338), 608-616 (2017).
18. M. D. Garrick et al., A direct comparison of divalent metal-ion transporter (DMT1) and hinokitiol, a potential small molecule replacement. *Biometals* (32), 745-755 (2019).

19. J. Lee, J. R. Prohaska, D. J. Thiele, Essential role for mammalian copper transporter Ctr1 in copper homeostasis and embryonic development. *Proc Natl Acad Sci U S A.* 98(12), 6842-6847 (2001).
20. B. E. Kim et al., Cardiac copper deficiency activates a systemic signaling mechanism that communicates with the copper acquisition and storage organs. *Cell Metab.* 11(5), 353-363 (2010).
21. M. J. Niciu et al., Altered ATP7A expression and other compensatory responses in a murine model of Menkes disease. *Neurobiol Dis.* 27(3) 278-291 (2007).
22. A. Grimes, C. J. Hearn, P. Lockhart, D. F. Newgreen, J. F. Mercer. Molecular basis of the brindled mouse mutant (Mo(br)): a murine model of Menkes disease. *Hum Mol Genet.* 6(7), 1037-1042 (1997).
23. A. Donsante et al., ATP7A gene addition to the choroid plexus results in long-term rescue of the lethal copper transport defect in a Menkes disease mouse model. *Mol Ther.* 19(12), 2114-2123 (2011).
24. M. R. Haddad et al., rAAV9-rsATP7A plus subcutaneous copper histidinate advance survival and outcomes in a Menkes disease mouse model. *Mol Ther Methods Clin Dev.* 10, 165-178 (2018).
25. S. G. Kaler, Neurodevelopment and brain growth in classic Menkes disease is influenced by age and symptomatology at initiation of copper treatment. *J. Trace Elem Med Biol.* 28(4), 427-430 (2014).

26. J. W. Pyatskowitz, J. R. Prohaska, Copper deficient rats and mice both develop anemia but only rats have lower plasma and brain iron levels. *Comp Biochem Physiol C Toxicol Pharmacol.* 147(3), 316-323 (2008).
27. S. R. Setty et al., Cell-specific ATP7A transport sustains copper-dependent tyrosinase activity in melanosomes. *Nature.* 454(7208), 1142-1146 (2008).
28. J. M. Gillespie, Keratin structure and changes with copper deficiency. *Australas J Dermatol.* 14(3), 127-131 (1973).
29. M. Bourens, A. Barrientos, A *CMCI*-knockout reveals translation-independent control of human mitochondrial complex IV biogenesis. *EMBO Rep.* 18(3), 477-494 (2017).
30. A. A. Yadav, D. Patel, X. Wu, B. B. Hasinoff, Molecular mechanisms of the biological activity of the anticancer drug elesclomol and its complexes with Cu(II), Ni(II), and Pt(II). *J Inorg Biochem.* 126, 1-6 (2013).
31. M. Nagai et al., The oncology drug elesclomol selectively transports copper to the mitochondria to induce oxidative stress in cancer cells. *Free Radic Biol Med.* 52(10), 2142-2150 (2012).
32. R. K. Blackman et al., Mitochondrial electron transport is the cellular target of the oncology drug elesclomol. *PLoS One.* 7(1), e29798 (2012).
33. P. Tsvetkov et al., Mitochondrial metabolism promotes adaptation to proteotoxic stress. *Nat Chem Biol.* 15(7), 681-689 (2019).

34. Miller-Fleming, L., F. Giorgini, and T.F. Outeiro, *Yeast as a model for studying human neurodegenerative disorders*. Biotechnology Journal, 2008. 3(3): p. 325-338.
35. Lau, C.-H. and Y. Suh, *In vivo genome editing in animals using AAV-CRISPR system: applications to translational research of human disease*. F1000Research, 2017. 6: p. 2153-2153.

Figure III-1: Effects of ES treatment in cardiac Ctr1 KO mice.

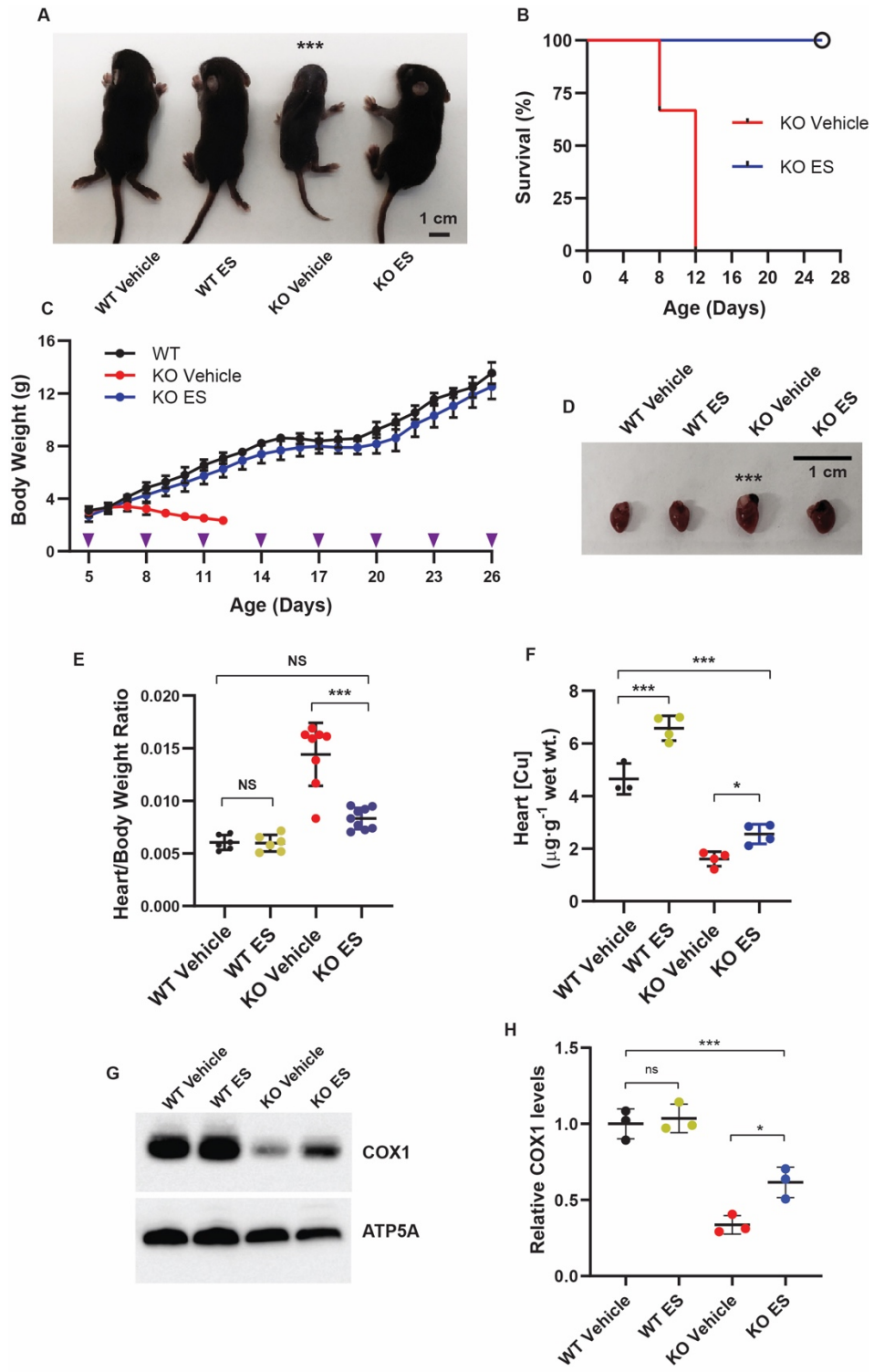


Figure III-1 Continued: A) Gross appearance of mice at PND 10. B) Kaplan-Meier survival curve. C) Growth Curves. WT and WT ES mice exhibited identical growth curves (WT ES omitted for clarity: see Fig S3A). Cohorts consisted of WT vehicle ($n = 3$), WT ES ($n = 7$), KO vehicle ($n = 3$), and KO ES ($n = 9$). D) Gross appearance of hearts at PND 10. E) Heart/body weight ratio. Cohorts consisted of $n = 6, 6, 8, \& 9$ animals respectively. F) Heart [Cu] levels. Cohorts consisted of $n = 4$ per treatment. G) Heart COX1 levels. H) Quantification of relative COX1 levels. Data reported as mean \pm SD with statistical significance assessed by one-way ANOVA with post hoc Tukey's HSD test or Welch one-way ANOVA with post hoc Tukey's HSD test. NS = not significant, $*p < 0.05$, $***p < 0.001$. Western blot images analyzed with ImageJ software. Image bars represent 1 cm.

Figure III-2: Effects of ES-Cu²⁺ treatment in *mo-br* mice.

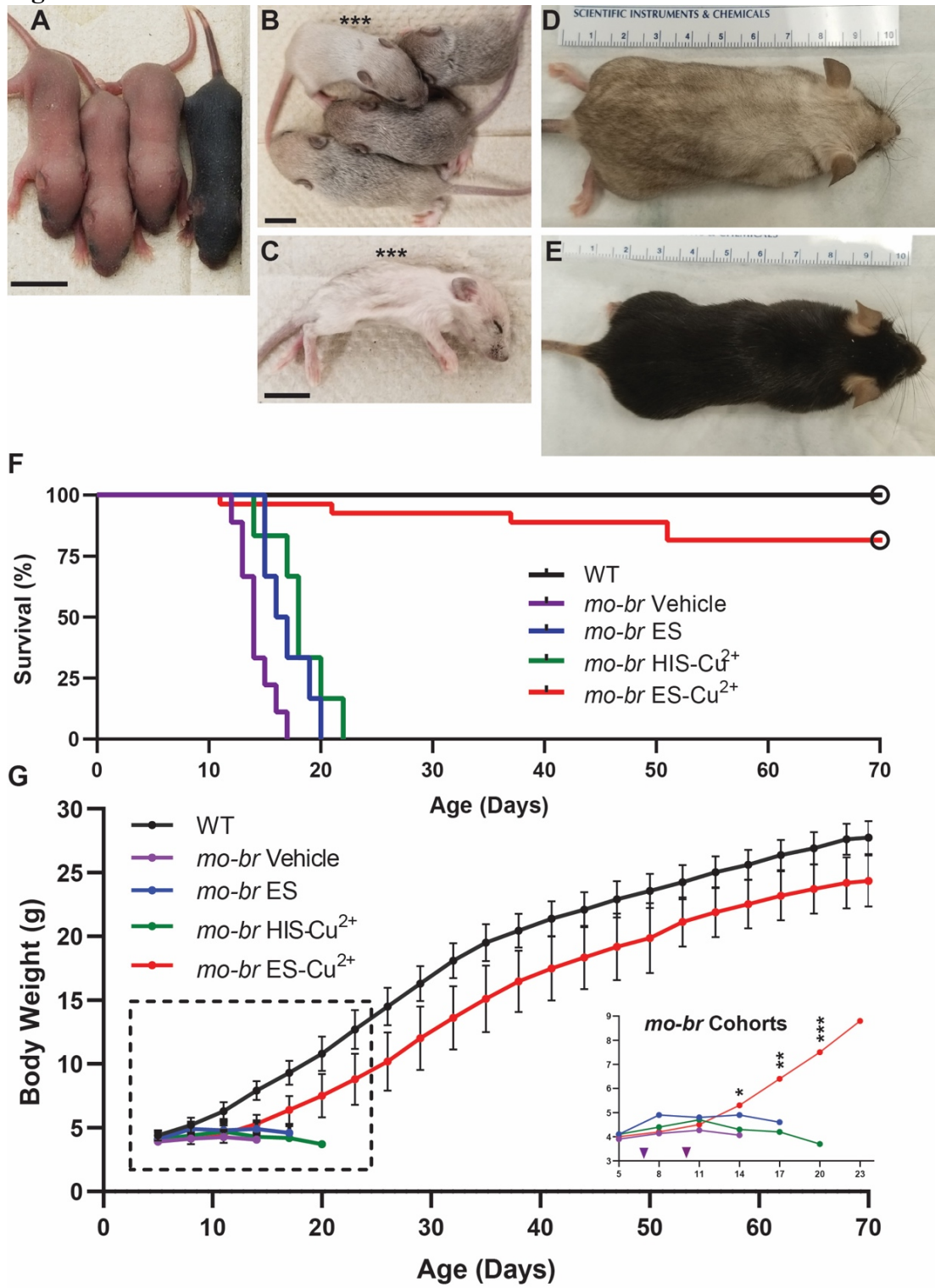
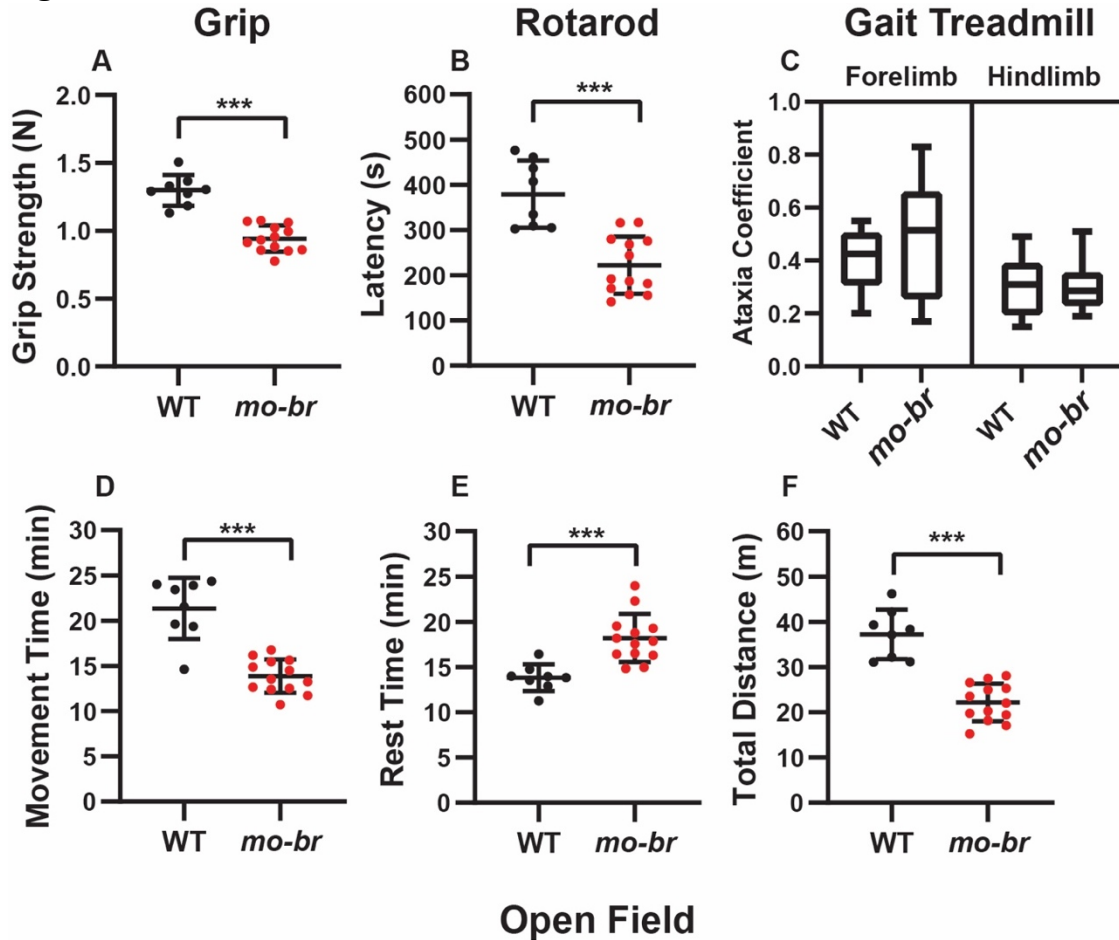


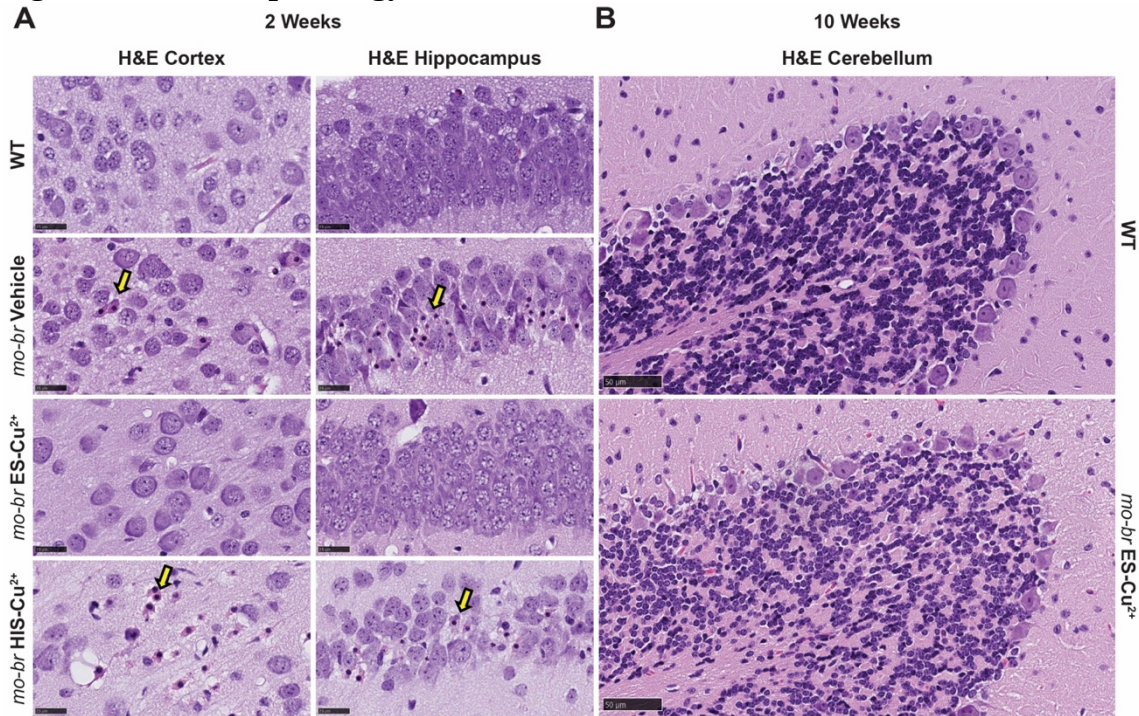
Figure III-2 Continued: A) *Mo-br* hemizygous males and WT littermate at PND 5 before intervention. B) Pigmentation changes in *mo-br* males administered ES-Cu²⁺ compared to vehicle (***) on PND 12. C) Moribund *mo-br* vehicle (***) mouse PND 14. D & E) *mo-br* ES-Cu²⁺ and WT littermate at PND 70. F) Kaplan-Meier survival curve. All WT mice survived experimental protocol. G) Growth Curves of indicated groups: WT and WT ES-Cu²⁺ mice exhibited near identical growth curves (WT ES-Cu²⁺ omitted for clarity: see Fig S8E). Cohorts consisted of WT vehicle ($n = 15$), WT ES-Cu²⁺ ($n = 13$), *mo-br* vehicle ($n = 9$), *mo-br* ES ($n = 6$), *mo-br* HIS-Cu²⁺ ($n = 6$), and *mo-br* ES-Cu²⁺ ($n = 27$). Data reported as mean \pm SD with statistical significance assessed by one-way ANOVA test or Welch one-way ANOVA with post hoc Tukey's HSD test. * $p < 0.05$, ** $p < 0.01$, *** $p < 0.001$. Image bars represent 1 cm.

Figure III-3: Neuromotor tests of 10 week old mice.



Mice were assessed by grip strength, rotarod, gait treadmill, and open field at 10 weeks of age. A) Forelimb grip strength. B) Rotarod. C) Gait Treadmill. DigiGait™ generated ataxia coefficients of shoulder and pelvic girdles were statistically insignificant. D-F) Open Field. Movement time, rest time, and total distance. Cohorts consisted of WT $n = 8$ and *mo-br* $n = 13$. Data reported as mean \pm SD with statistical significance assessed by unpaired t-test. *** $p < 0.001$.

Figure III-4: Neuropathology of 2 and 10 week old mice.



A) Cortex and hippocampus from PND 14 WT and *mo-br* mice administered vehicle, ES-Cu²⁺ or HIS-Cu²⁺. Somatomotor cortical neurons in *mo-br* vehicle and HIS-Cu²⁺ cohorts exhibit marked, diffuse neurodegenerative changes characterized by numerous pyknotic nuclei with eosinophilic cytoplasm (yellow arrows). In the hippocampus, the pyramidal neuron layer of region CA1 demonstrates degenerative changes including necrotic neurons in vehicle and HIS-Cu²⁺ *mo-br* mice (yellow arrows). B) Cerebellar peduncles from PND 70 WT and *mo-br* ES-Cu²⁺ mice revealed preservation of continuous Purkinje neuron layer. Scale bars represent 25 μm in cortical and hippocampal H&E slides. Scale bars represent 50 μm in cerebellar H&E slides.

Figure III-5: ES-Cu⁺ rescues biochemical phenotypes in 2 and 10 week old *mo-br* mice.

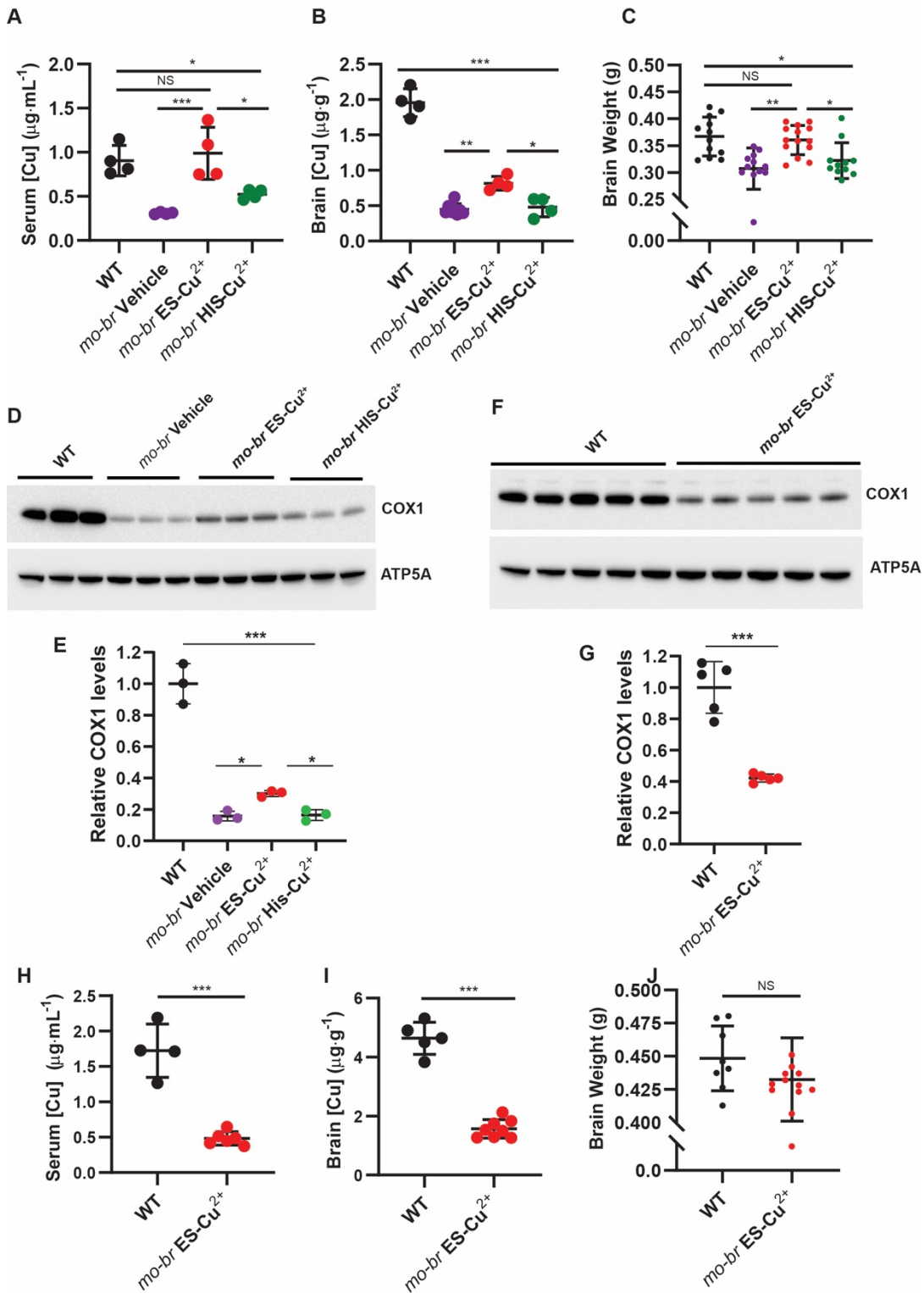
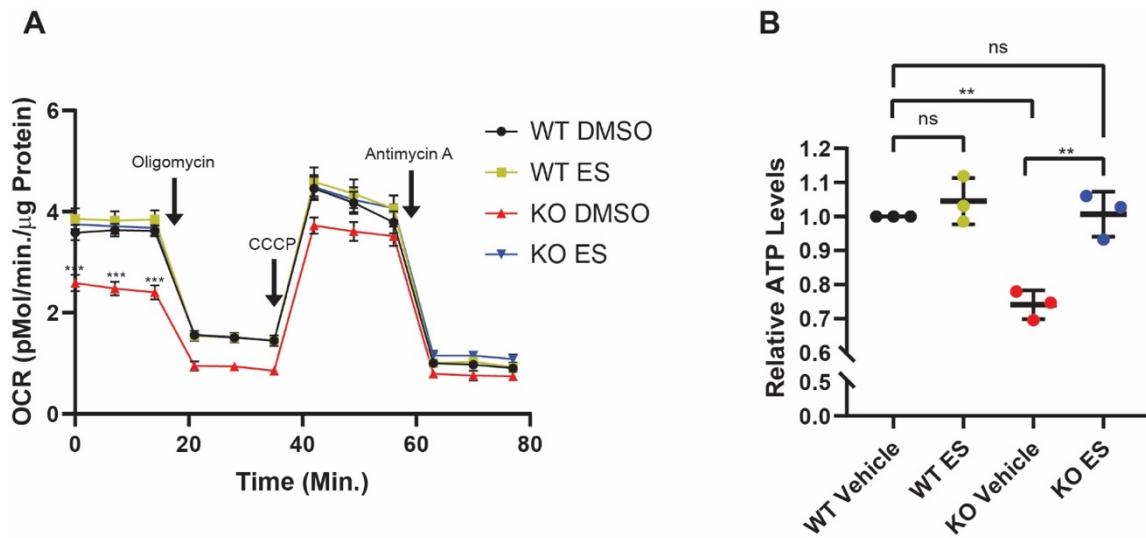


Figure III-5 Continued: A) Serum [Cu] at PND 14. (All cohorts $n = 4$) B) Brain [Cu] at PND 14. (All cohorts $n = 4$) C) Brain weights at PND 14. (WT $n = 12$, *mo-br* Vehicle $n = 12$, *mo-br* ES-Cu²⁺ $n = 14$, *mo-br* HIS-Cu²⁺ $n = 11$, D-E) Brain COX1 at PND 14 (All cohorts $n = 3$). F-G) Brain COX1 at PND 70 (All cohorts $n = 5$) H) Serum [Cu] at PND 70. (WT $n = 4$, *mo-br* ES-Cu²⁺ $n = 6$) I) Brain [Cu] at PND 70. (WT $n = 5$, *mo-br* ES-Cu²⁺ $n = 8$) J) Brain weights at PND 70. (WT $n = 8$, *mo-br* ES-Cu²⁺ $n = 13$). Data reported as mean \pm SD with statistical significance assessed by one-way ANOVA or Welch one-way ANOVA with post hoc Tukey's HSD test. NS = not significant * $p < 0.05$, ** $p < 0.01$, *** $p < 0.001$. Western images analyzed with ImageJ software.

Table III-1: Treatment Regime and 10 week survival in the *mottled-brindled* mouse.

Cohort	<i>n</i>	Treatment				Survival		
		Exposure (mg·kg ⁻¹)	Total (μg)	ES/HIS (μg)	Cu ²⁺ (μg)	Median (Days)	Viable Mice 10 Weeks	Percent (%)
WT Vehicle	15	-	-	-	-	-	15	100
WT ES-Cu²⁺	13	7.25	29	25.02	3.98	-	13	100
<i>mo-br</i> Vehicle	9	-	-	-	-	14	0	0
<i>mo-br</i> ES	6	6.25	25.02	25.02	-	16.5	0	0
<i>mo-br</i> ES-Cu²⁺	27	7.25	29	25.02	3.98	203	22	81.5
<i>mo-br</i> HIS-Cu²⁺	6	5.83	23.3	19.35	3.98	18	0	0

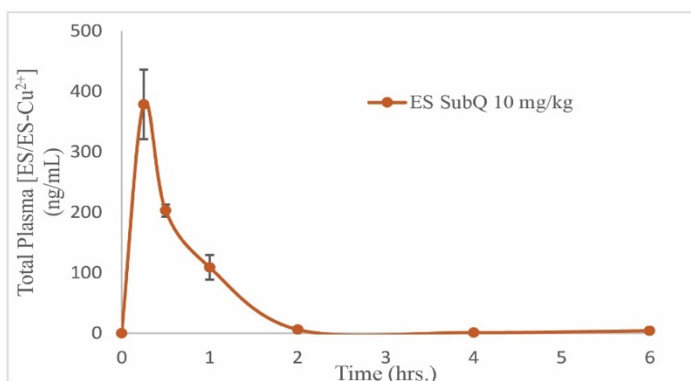
Figure III-6 (S1): Effects of ES treatment on OCR and relative ATP levels in *Ctrl* KO H9c2 cardiac cells.



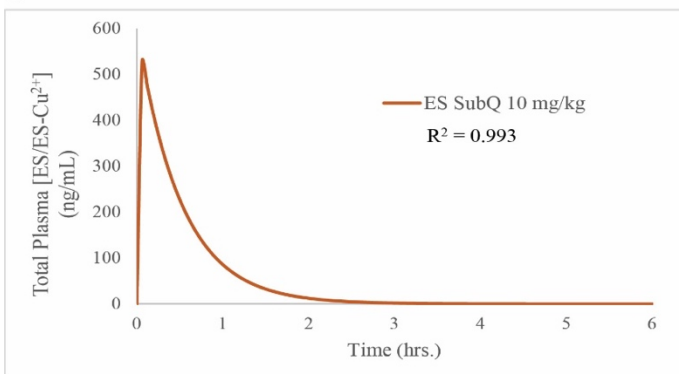
A) ES treatment restores mitochondrial respiration in *Ctrl* KO H9c2 cardiac cells ($n = 15$, three biological replicates each with 5 technical replicates per cohort, *** $p < 0.01$). WT and *Ctrl* KO cells were cultured with and without 1 nM ES for 4 days prior to performing oxygen consumption rate (OCR) measurements. Oligomycin, CCCP, and antimycin A were used to measure ATP-coupled respiration, maximum respiratory capacity, and mitochondria—specific respiration, respectively. OCR data reported as mean \pm SEM. B) WT and *Ctrl* KO H9c2 cells were cultured with and without 1 nM ES in galactose-containing media for 4 days before ATP measurements. ATP quantification data expressed as mean \pm SD, ($n=3$). Statistical analysis reported as one-way ANOVA with post hoc Tukey’s multiple comparisons test.

Figure III-7 (S2): ES 0.5% Methocel™ pharmacokinetics (PK).

A



B



C

ES Compartmental Analysis		Route
Parameter	Units	SubQ
Exposure	mg/kg	10
Dose	µg	207
A	ng/ml	601.08
α	1/h	0.01
t _{1/2}	h	0.36
C ₀ /C _{max}	ng/ml	529.74
T _{max}	h	0.05
AUC _{0-t}	ng/ml*h	300.45

A) Non-compartmental analysis (NCA) of plasma vs time plot of subcutaneously administered ES formulated in 0.5% Methocel™ with 2% final DMSO. B) PKSolver generated 1-compartment analysis (CA) model. C) Calculated PK parameters of subcutaneous ES. NCA data presented as mean ± SD of biological triplicates, analytical duplicates per time point. Methocel™ vehicle was used for cardiac *Ctrl* KO mouse efficacy studies.

Figure III-8 (S3): Effects of ES treatment in cardiac *Ctrl* KO mice.

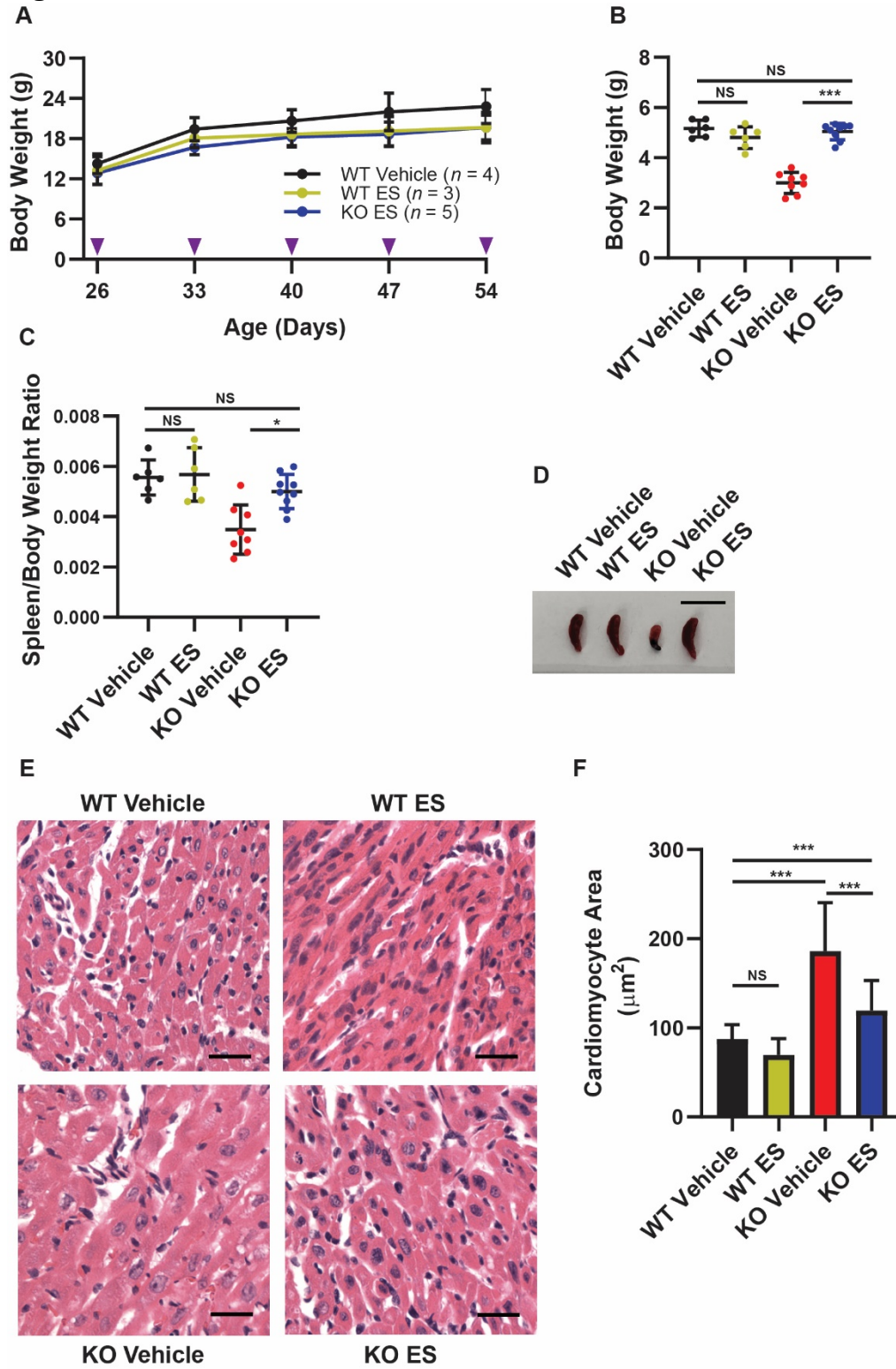
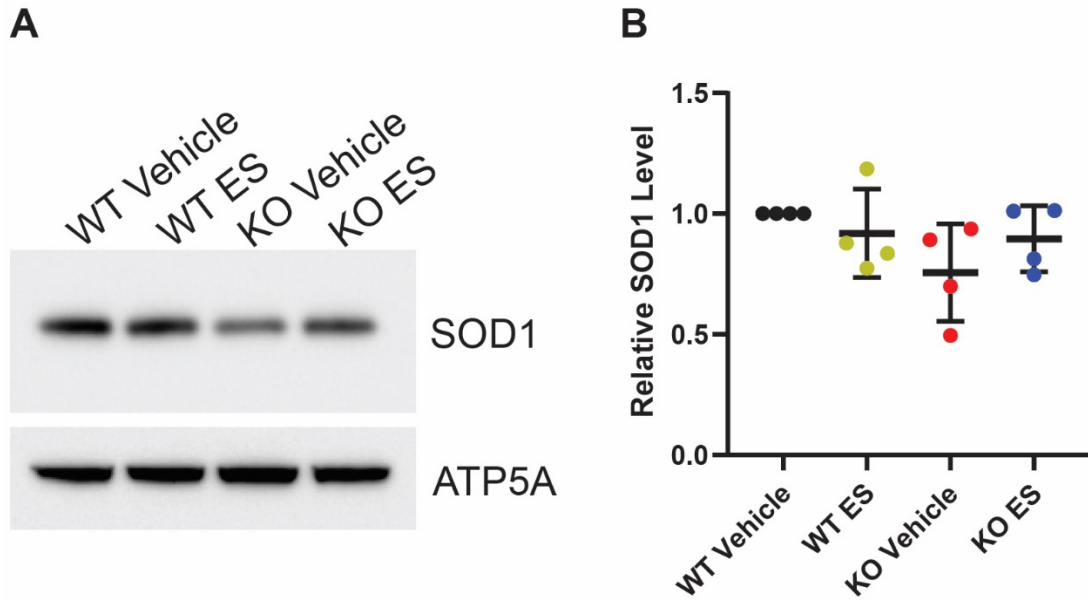


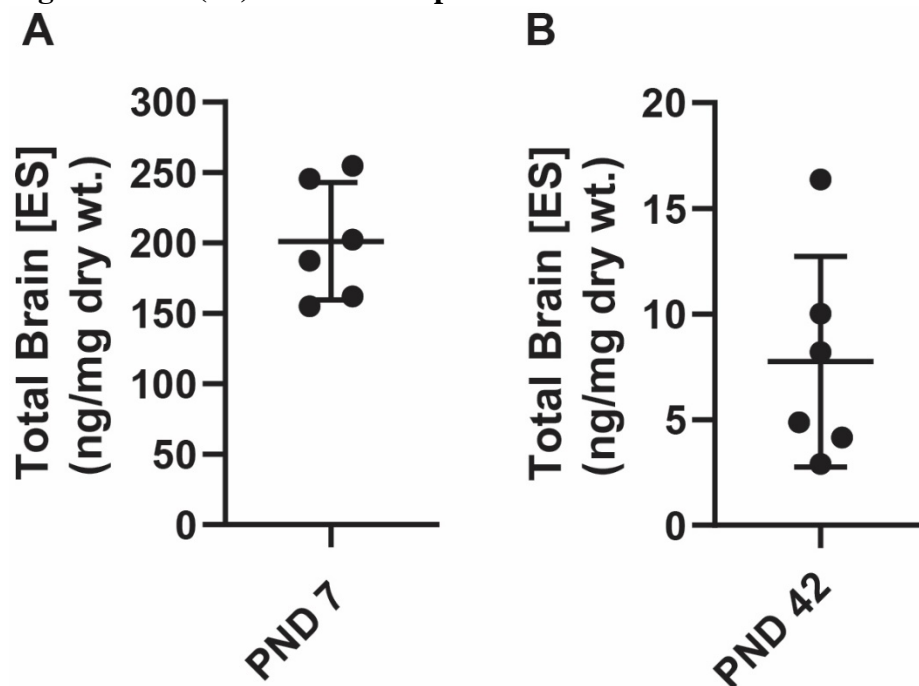
Figure III-8 (S3) Continued: A) Extended treatment and monitoring of WT and KO mice to PND 54. B) Body weight at PND 10 necropsy: Treatment of KO mice with ES normalized body weight (5.2 g WT vs 5.0 g KO ES, $p = 0.92$) while KO vehicle demonstrates severe growth deficit compared to ES treatment (3.0 g vs 5.0 g, $p < 0.01$). C) Spleen/body weight ratio: KO ES treatment normalized spleen/body weight ratio to WT ($p = 0.61$) whereas KO vehicle mice exhibited smaller spleens ($p < 0.01$). Cohorts for B & C consisted of WT vehicle $n = 6$, WT ES $n = 6$, KO vehicle $n = 8$, and KO ES $n = 9$. (NS = not significant, $*p < 0.05$, $***p < 0.001$). D) Spleen gross appearance. E/F) Cardiac histology: KO vehicle mice exhibit pronounced hypertrophic changes characterized by increased cardiomyocyte cell area. All data reported as mean \pm SD. Statistical analysis reported as one-way ANOVA with post hoc Tukey's multiple comparisons test unless otherwise noted. Spleen image bar represent 1 cm. Cardiac histology image bars represent 25 μ m.

Figure III-9 (S4): Effects of ES treatment on SOD1 levels in cardiac *Ctrl* KO mice.



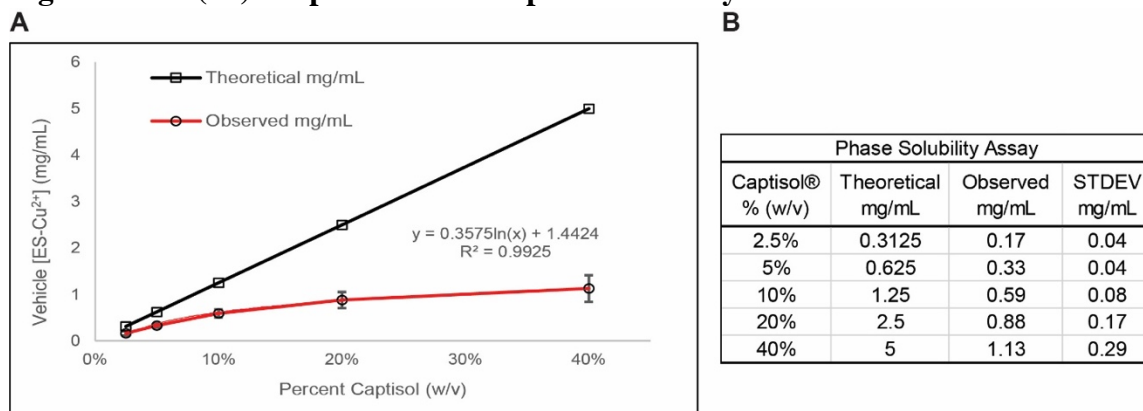
A) Representative Western blot depicting SOD1 abundance in cardiac tissue of two week old mice. B) Quantification of relative abundance ($n = 4$). No significance found between cohorts ($p > 0.01$). All data reported as mean \pm SD. Statistical analysis reported as one-way ANOVA with post hoc Tukey's multiple comparisons test. Western images analyzed using ImageJ software.

Figure III-10 (S5): Brain ES exposure.



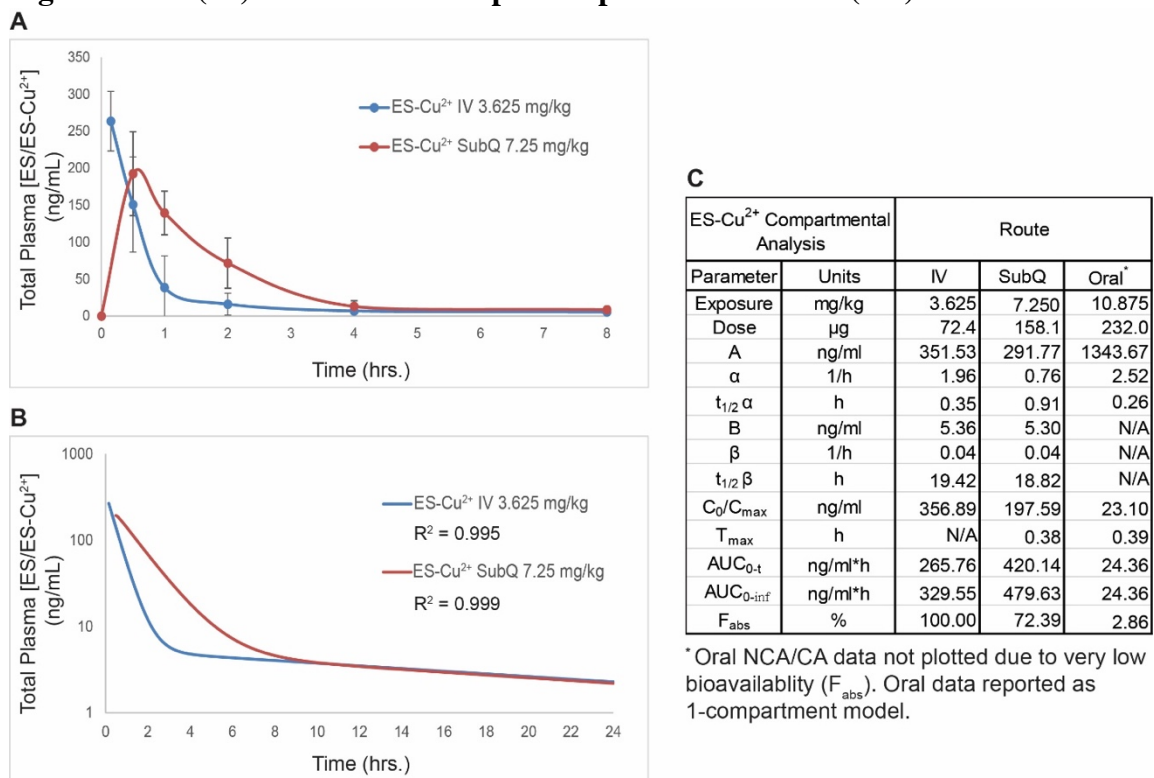
WT C57BL/6 mice ($n = 6$) of PND 7 and 42 (6 weeks) of age administered 3.625 mg/kg ES-Cu²⁺ complex were harvested approximately 1 hour after subcutaneous injection. Drug quantification from brain tissue followed euthanasia and saline perfusion. A) PND 7 mice: Brain drug exposure 201.3 ± 41.7 ng/mg. B) PND 42 mice: Brain drug exposure 7.8 ± 5.0 ng/mg. All data reported as mean ± SD.

Figure III-11 (S6): Captisol® ES-Cu²⁺ phase solubility.



A) Theoretical and observed solubility curves of ES-Cu²⁺ complex in 2.5%, 5%, 10%, 20%, and 40% Captisol® vehicle preparations. B) Quantified complex by LC-MS demonstrating maximum stable concentrations of drug complex preparations. All data reported as mean ± SD. Individual values represent analytical triplicates.

Figure III-12 (S7): ES-Cu²⁺ 20% Captisol® pharmacokinetics (PK).



A) Non-compartmental analysis (NCA) of plasma vs time plot of intravenous and subcutaneously administered ES-Cu²⁺ formulated in Captisol®. B) PKSolver generated 2-compartment analysis (CA) models. C) Calculated PK parameters of intravenous, subcutaneous, and oral ES-Cu²⁺. NCA data presented as mean ± SD of biological triplicates, analytical duplicates per time point. Captisol® vehicle was used for *mo-br* mouse efficacy studies.

Figure III-13 (S8): Effects of ES-Cu²⁺ treatment in *mo-br* mice.

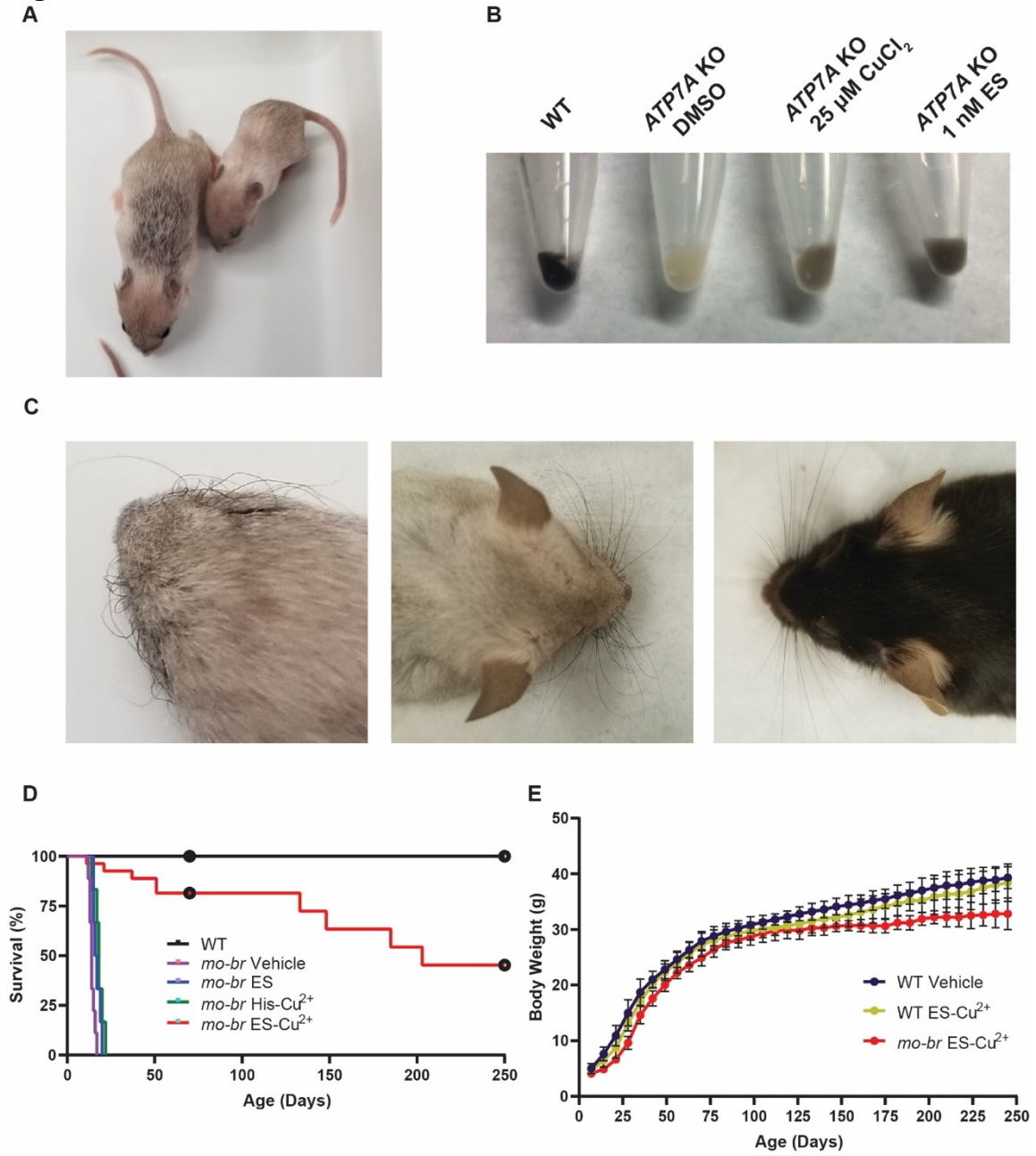
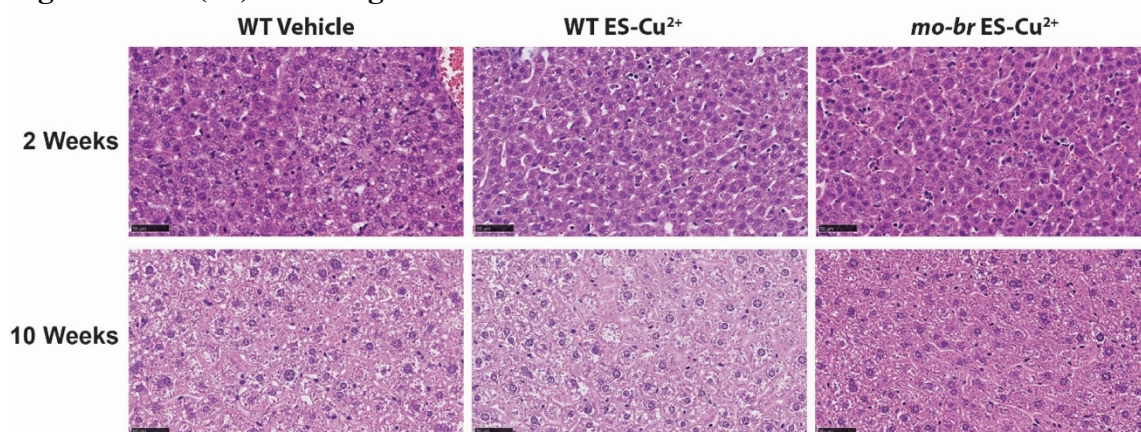


Figure III-13 (S8) Continued: A) Fur pigmentation: Intense pigmentation changes around the site of injection indicated rescue of the secretory pathway cuproenzyme tyrosinase. B) B16 melanoma *ATP7A* KO: ES and treatment improves tyrosinase activity *in vitro*. C) Whisker morphology: *mo-br* mice initially presented with highly kinked, bushy clumps of whiskers (left). Whisker appearance normalized at PND 70 (center). WT male at PND 70 (right). D) Extended survival study: Subsets of WT ($n = 5$), WT ES-Cu²⁺ ($n = 4$), and *mo-br* ES-Cu²⁺ ($n = 11$) continued on an observation only arm of the initial study until PND 245. All WT mice survived to week 35. *Mo-br* mice reported a median survival of 203 days. ($p < 0.01$, Log-Rank). E) Extended growth curve: Weekly weight reveals no difference between WT cohorts. *Mo-br* mice demonstrated gross body weight deficit. All data reported as mean \pm SD. Statistical analysis reported as one-way ANOVA with post hoc Tukey's multiple comparisons test unless otherwise noted. Image bars represent 1 cm.

Figure III-14 (S9): Histological examination of 2 and 10 week livers.



Livers collected from WT vehicle, WT ES-Cu²⁺, and *mo-br* ES-Cu²⁺ treated mice at 2 and 10 weeks of age revealed no pathological changes following exposure to ES-Cu²⁺ treatment. A blinded pathologist's report indicated minimal, multifocal hepatocellular vacuolization (lipid type) and mild, multifocal extramedullary hematopoiesis in samples collected from 2 week old mice. Both findings are considered incidental in young animals. No abnormal findings were documented in 10 week old animals. All samples were fixed in 10% neutral buffered formalin before sectioning and H&E staining. Liver histopathology image bars represent 50 μ m.

Figure III-15 (S10): Additional neuropathology in 2 week old mice.

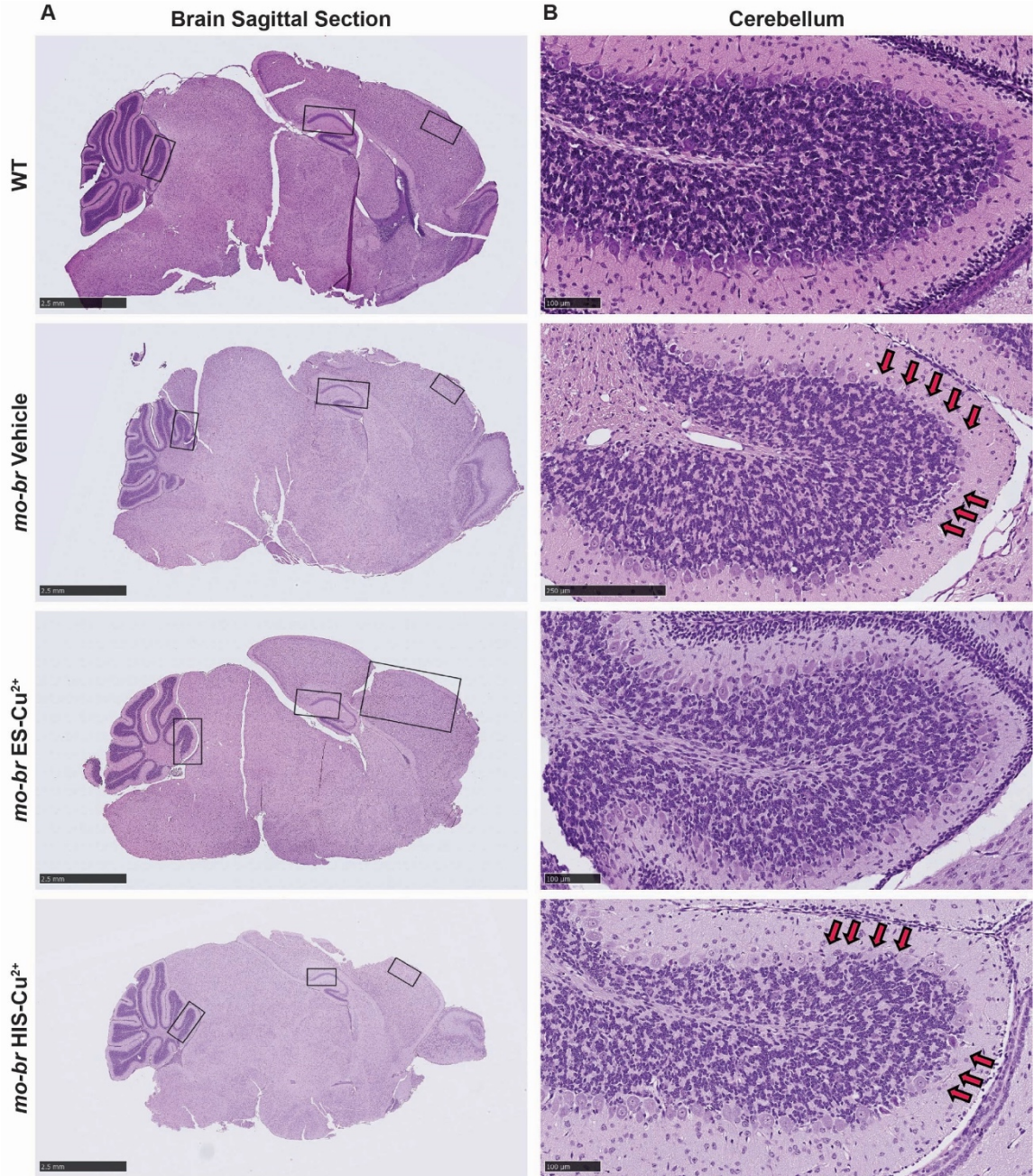
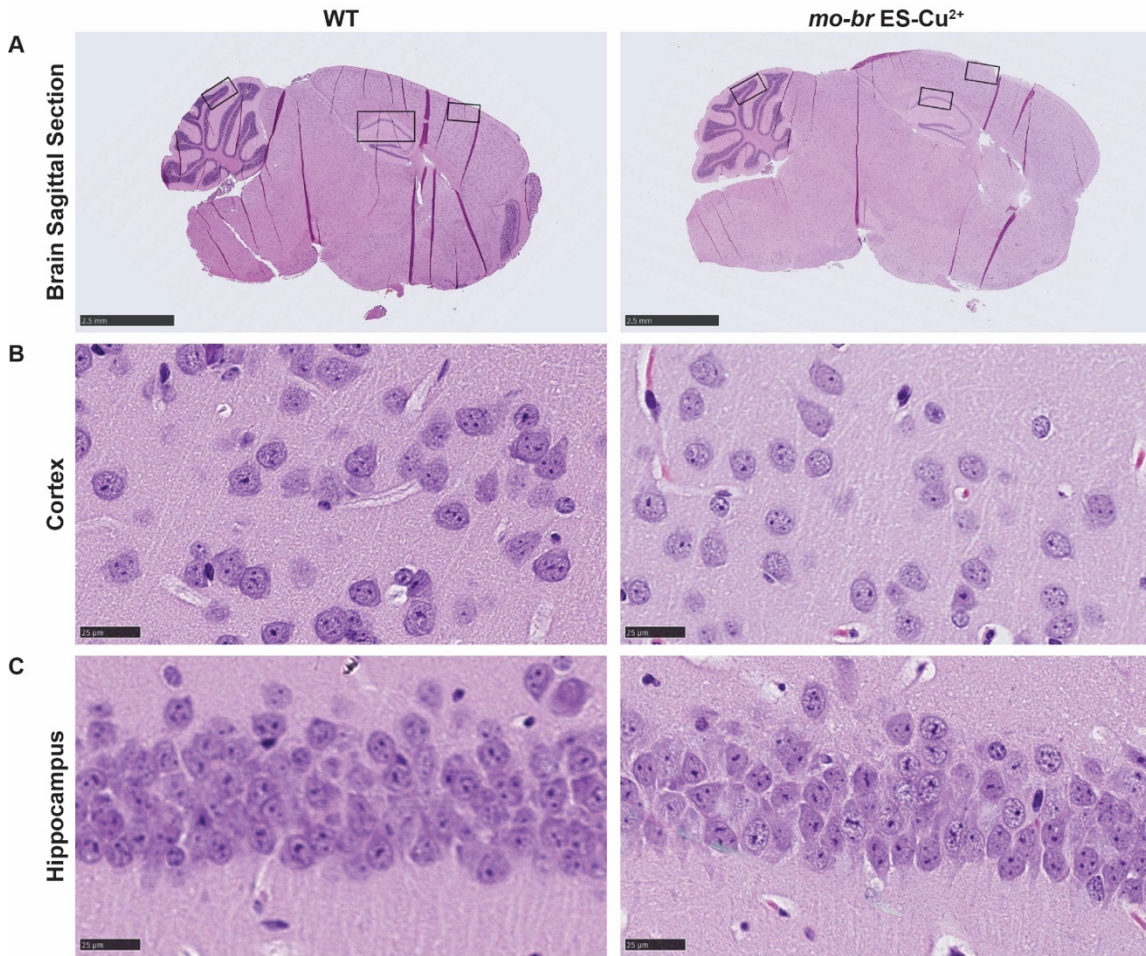


Figure III-15 (S10) Continued: Sagittal whole brain sections analyzed among cohorts. Surveyed areas represented by rectangular boxes (leftmost – cerebellum Fig. S10B, middle – hippocampus Fig. 4A, and rightmost – cortex Fig. 4A). Scale bars represent 2.5 mm. B) Cerebellum: Purkinje neuron layers are discontinuous (red arrows) and marked by rare necrotic nuclei in *mo-br* vehicle and HIS-Cu²⁺ cohorts. Normal tissue architecture is preserved in *mo-br* ES-Cu²⁺ mice. Scale bars represent 100 μ m.

Figure III-16 (S11): Additional neuropathology in 10 week old mice.



A) Sagittal brain sections analyzed among cohorts. Surveyed areas represented by rectangular boxes (leftmost – cerebellum Fig. 4B, middle – hippocampus Fig. S11C, and rightmost – cortex Fig. 11B). Scale bars represent 2.5 mm. B) Cortex: Neuroprotective effects of ES-Cu²⁺ treatment persisted to 10 week assessment. Scale bars represent 25 μm. C) Hippocampus: Pyramidal neurons preserved. Scale bars represent 25 μm.

Figure III-17 (S12): Heart biochemistry *mo-br* mice.

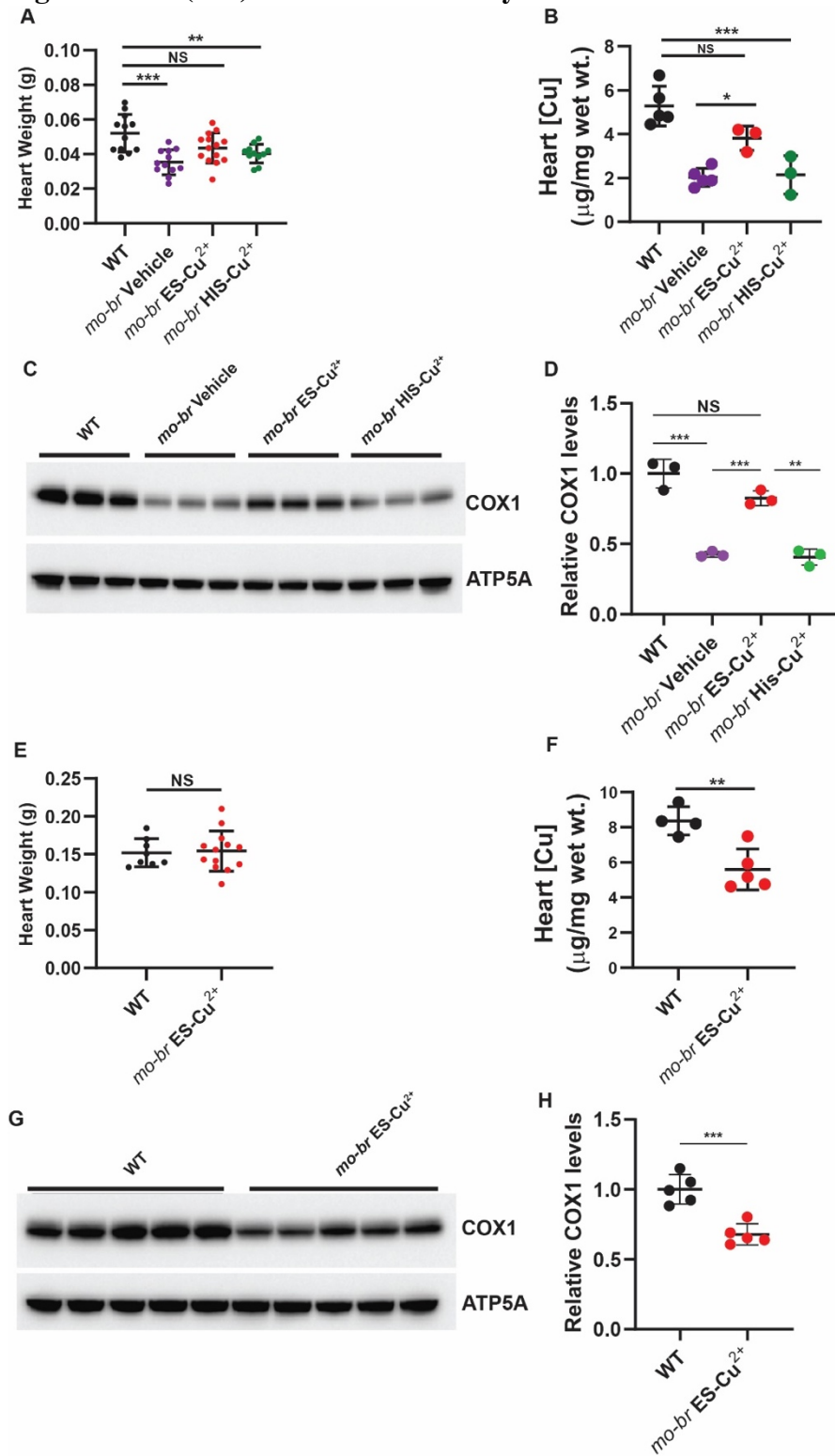
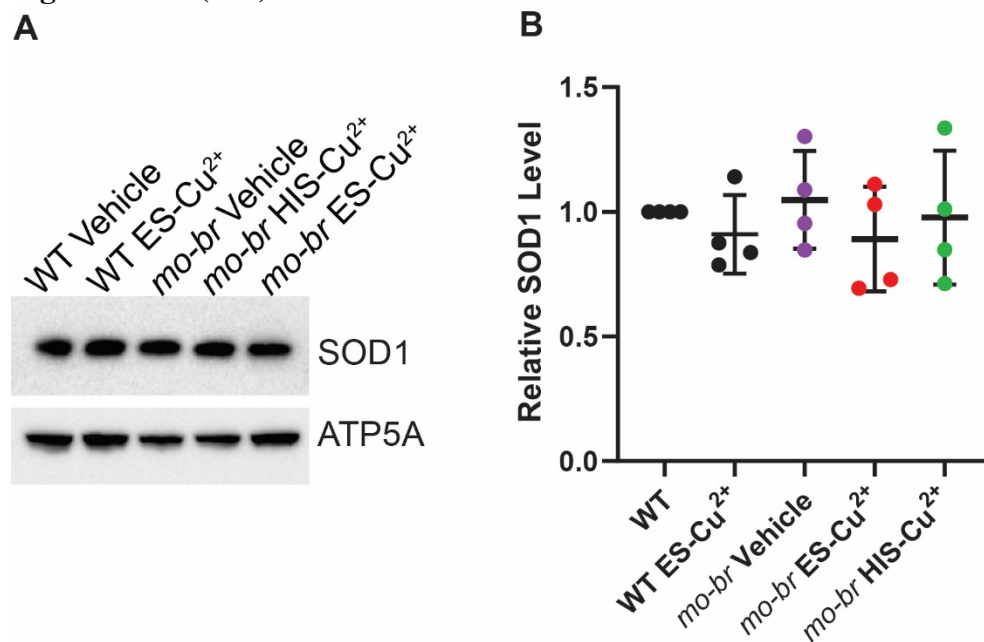


Figure III-17 (S12) Continued: A) Heart weight at PND 14: *Mo-br* ES-Cu²⁺ treatment normalizes heart weight compared to WT (0.043 vs 0.052 g, $p = 0.06$). (Cohorts $n = 12, 12, 14,$ & 11). B) Heart [Cu] at PND 14: ES-Cu²⁺ treatment increased heart [Cu] from baseline vehicle levels of 2.0 to 3.8 $\mu\text{g}\cdot\text{g}^{-1}$ ($p = 0.02$) and proved superior to HIS-Cu²⁺ (2.1 $\mu\text{g}\cdot\text{g}^{-1}$, $p = 0.01$). ES-Cu²⁺ normalize heart [Cu] to WT levels (5.3 $\mu\text{g}\cdot\text{g}^{-1}$, $p = 0.06$). ES-Cu²⁺ improved [Cu] from 38% to 72% of WT levels—an approximate increase of 34%. For comparison, HIS-Cu²⁺ improved mean heart [Cu] by only 2% (2.1 $\mu\text{g}\cdot\text{g}^{-1}$, $p = 0.98$). (Cohorts $n = 5, 5, 3,$ & 3). C) COX1 at PND 14. D) COX1 Relative levels at PND 14: ES-Cu²⁺ improved COX1 abundance by 41.6% relative to vehicle (0.835 vs 0.406, $p = 0.002$). HIS-Cu²⁺ did not significantly improve COX1 abundance (0.426, $p = 0.98$). E) Heart weight at PND 70 (Cohorts $n = 8$ & 13). F) Heart [Cu] PND 70: Heart [Cu] declined to 67% of WT (5.6 vs 8.4 $\mu\text{g}\cdot\text{g}^{-1}$, $p < 0.01$). (Cohorts $n = 4$ & 5). G) COX1 at PND 70. H) COX1 Relative levels at PND70: ES-Cu²⁺ *mo-br* adults 67.9% of WT ($p < 0.001$). (NS = not significant, * $p < 0.05$, ** $p < 0.01$, *** $p < 0.001$). All data reported as mean \pm SD. Statistical analysis reported as one-way ANOVA or Welch ANOVA with post hoc Tukey's multiple comparisons test or unpaired t-test.

Figure III-18 (S13): Effects of ES treatment on SOD1 levels in *mo-br* mice.



A) Representative Western blot depicting SOD1 abundance in brain tissue of two week old mice. B) Quantification of relative abundance ($n = 4$). No significance found between cohorts ($p > 0.01$). All data reported as mean \pm SD. Statistical analysis reported as one-way ANOVA with post hoc Tukey's multiple comparisons test. Western images analyzed using ImageJ software.

Table III-2 (S1): Elesclomol tolerability in adult C57BL/6 females.

SubQ Bolus		Body Mass								
		Day 0		Day 5			Day 10			
Dose Level	<i>n</i>	Mass	p-value	Mass	% Δ	p-value	Mass	% Δ	p-value	
Methocel™ Vehicle	3	18.8 ± 0.7	0.39	19.5 ± 0.7	3.5%	0.25	19.9 ± 0.7	5.9%	0.56	
ES 25 mg·kg ⁻¹ Methocel™	5	18.3 ± 0.9		18.9 ± 0.6	3.3%		19.6 ± 0.7	7.3%		
Captisol® Vehicle	4	18.4 ± 0.7	0.73	18.9 ± 0.6	2.9%	0.53	19.7 ± 0.6	7.5%	0.64	
ES 25 mg·kg ⁻¹ Captisol®	5	18.2 ± 0.8		18.6 ± 0.8	2.2%		19.5 ± 0.5	7.6%		

Table III-3 (S2): Elesclomol tolerability in adult C57BL/6 females.

SubQ Bolus		Body Mass								
		Day 0		Day 5			Day 10			
Dose Level	<i>n</i>	Mass	p-value	Mass	% Δ	p-value	Mass	% Δ	p-value	
Captisol® Vehicle	4	20.6 ± 1.8	-	21.2 ± 1.8	2.8%	-	21.7 ± 1.7	5.5%	-	
3.625 mg/kg ES-Cu ²⁺	5	19.8 ± 1.2	0.56	20.1 ± 1.4	1.3%	0.41	20.6 ± 1.7	4.2%	0.48	
7.25 mg/kg ES- Cu ²⁺	5	20.1 ± 1.0	0.80	19.6 ± 1.0	-2.8%	0.19	20.1 ± 1.2	-0.3%	0.22	

Table III-4 (S3): CBC of 10 week old C57BL/6 and *mo-br* mice.

CBC	WT Vehicle (n = 5)	WT ES- Cu²⁺ (n = 5)	<i>mo-br</i> ES-Cu²⁺ (n = 10)	Ref. Range*
WBC 10 ⁹ /l	6.7 ± 1.5	9.1 ± 3.6	6.9 ± 2.1	6 – 15
LYM 10 ⁹ /l	5.4 ± 1.1	6.7 ± 2.3	5.1 ± 2.0	3 – 7
MON 10 ⁹ /l	0.2 ± 0.2	0.2 ± 0.2	0.1 ± 0.1	0.0 – 0.6
NEU 10 ⁹ /l	1.1 ± 1.0	2.2 ± 1.9	1.7 ± 1.3	0.5 – 3.8
RBC 10 ¹² /l	11.3 ± 0.4	11.2 ± 0.8	9.8 ± 0.9	7 – 12
HCT %	52.9 ± 1.2	50.3 ± 5.5	47.3 ± 3.9	35 – 45
HGB g/dl	16.8 ± 0.9	16.4 ± 1.7	15.2 ± 1.3	12 – 16
MCV <u>f</u> l	47.0 ± 1.4	45.0 ± 2.3	48.2 ± 2.1	45 – 55
MCH <u>p</u> g	15.0 ± 1.2	14.6 ± 0.7	15.5 ± 0.8	11 – 13
MCHC g/dl	31.9 ± 2.0	32.6 ± 1.0	32.1 ± 0.8	22 – 32
PLT 10 ⁹ /l	463.2 ± 78.2	531.2 ± 81.3	425.6 ± 156.4	200 – 450

* Normal hematology ranges as indicated by Vet Scan HM5 Operator's Manual for mice.

Table III-5 (S4): Serum chemistries of 10 week old C57BL/6 and *mo-br* mice.

Serum Chemistries	WT Vehicle (n= 4)	WT ES-Cu²⁺ (n = 4)	<i>mo-br</i> ES-Cu²⁺ (n = 8)	Ref. Range*
ALP (U/l)	120.3 ± 11.5	155.3 ± 25.5	251.1 ± 41.6	100 – 184
ALT (U/l)	15.5 ± 4.0	14.0 ± 3.5	9.3 ± 4.8	13 – 56
BUN (mg/dl)	17.0 ± 1.2	16.5 ± 1.3	11.9 ± 4.6	7.8 – 15.5
CRE (mg/dl)	0.3 ± 0.2	0.3 ± 0.1	2.2 ± 0.8	0.3 – 0.4
TP (g/dl)	4.8 ± 0.7	4.5 ± 0.8	1.7 ± 0.3	4.4 – 5.8

*Normal ranges as indicated by Clinical Chemistry Reference Intervals for C57BL/6J,

C57BL/6N, and C3HeB/FeJ Mice. Otto et al. *J Am Assoc Lab Anim Sci.* 2016.

Table III-6 (S5): Gait parameters at 10 week assessment in WT and *mo-br* males.

Gait Parameters						
Limb Girdle	Fore Limb			Hind Limb		
Cohorts	WT	<i>mo-br</i>	p-value	WT	<i>mo-br</i>	p-value
Stride (s)	0.284 ± 0.016	0.257 ± 0.008	< 0.001	0.285 ± 0.017	0.258 ± 0.008	< 0.001
Swing (s)	0.116 ± 0.009	0.096 ± 0.008	< 0.001	0.113 ± 0.006	0.097 ± 0.015	0.001
Brake (s)	0.048 ± 0.010	0.054 ± 0.019	0.316	0.021 ± 0.006	0.033 ± 0.010	< 0.001
Propel (s)	0.120 ± 0.017	0.107 ± 0.023	0.079	0.151 ± 0.011	0.129 ± 0.009	< 0.001
Stance (s)	0.168 ± 0.019	0.161 ± 0.011	0.105	0.172 ± 0.013	0.162 ± 0.012	0.020
Stride Frequency	3.600 ± 0.171	3.953 ± 0.134	< 0.001	3.550 ± 0.232	3.936 ± 0.127	< 0.001
Stride Length (cm)	6.817 ± 0.383	6.161 ± 0.200	< 0.001	6.833 ± 0.398	6.206 ± 0.182	< 0.001
Stance Width (cm)	1.667 ± 0.225	1.672 ± 0.259	0.963	2.583 ± 0.264	2.244 ± 0.313	0.027
Step Angle (°)	62.283 ± 2.440	65.033 ± 9.499	0.496	58.833 ± 8.209	57.289 ± 7.511	0.674
Paw Angle (°)	7.000 ± 6.4000	9.139 ± 7.601	0.386	16.658 ± 4.846	18.117 ± 5.804	0.438
Paw Area (cm²)	0.363 ± 0.059	0.447 ± 0.126	0.031	0.773 ± 0.108	0.859 ± 0.161	0.094
Ataxia Coefficient	0.406 ± 0.112	0.495 ± 0.231	0.205	0.313 ± 0.111	0.315 ± 0.087	0.944

Table III-7 (S6): Body, brain, and heart weights at 2 & 10 week necropsy.

2 Weeks		Organ Weights (g)					
		Body Weight		Brain		Heart	
Cohort	<i>n</i>	Mean	p-value	Mean	p-value	Mean	p-value
WT Vehicle	12	8.0 ± 0.9	-	0.3669 ± 0.0362	-	0.0520 ± 0.0052	-
WT ES-Cu ²⁺	11	7.2 ± 1.0	0.03	0.3784 ± 0.0438	0.93	0.0589 ± 0.0047	0.11
<i>mo-br</i> ES-Cu ²⁺	14	5.1 ± 0.7	< 0.01	0.3603 ± 0.0274	0.95	0.0435 ± 0.0087	0.09
<i>mo-br</i> His-Cu ²⁺	11	4.7 ± 0.7	< 0.01	0.3220 ± 0.0336	0.01	0.0403 ± 0.0054	< 0.01
<i>mo-br</i> Vehicle	12	3.9 ± 0.5	< 0.01	0.3070 ± 0.0386	< 0.01	0.0353 ± 0.0072	< 0.01
10 Weeks		Organ Weights (g)					
		Body Weight		Brain		Heart	
Cohort	<i>n</i>	Mean	p-value	Mean	p-value	Mean	p-value
WT Vehicle	8	30.7 ± 1.5	-	0.4484 ± 0.0245	-	0.1519 ± 0.0184	-
WT ES-Cu ²⁺	7	30.8 ± 2.2	0.99	0.4523 ± 0.0316	0.95	0.1513 ± 0.0155	0.99
<i>mo-br</i> ES-Cu ²⁺	13	25.2 ± 2.6	< 0.01	0.4523 ± 0.0315	0.33	0.1542 ± 0.0265	0.97

Table III-8 (S7): Thymus, lungs, kidney, liver, and spleen weights at 2 & 10 week necropsy

2 Weeks		Organ Weights (g)									
Cohort	n	Thymus		Lungs		Kidney		Liver		Spleen	
		Mean	p-value	Mean	p-value	Mean	p-value	Mean	p-value	Mean	p-value
WT Vehicle	12	0.0602 ± 0.0130	-	0.1001 ± 0.0126	-	0.0545 ± 0.0545	-	0.3277 ± 0.1194	-	0.0352 ± 0.0139	-
WT ES-Cu ²⁺	11	0.0607 ± 0.0091	0.99	0.0940 ± 0.0146	0.65	0.0678 ± 0.0118	0.02	0.3869 ± 0.0387	0.41	0.0496 ± 0.0106	0.06
<i>mo-br</i> ES-Cu ²⁺	14	0.0442 ± 0.0123	0.01	0.0812 ± 0.0174	< 0.01	0.0501 ± 0.0107	0.92	0.2647 ± 0.0448	0.32	0.0282 ± 0.0096	0.5
<i>mo-br</i> His-Cu ²⁺	11	0.0427 ± 0.0097	< 0.01	0.0880 ± 0.0230	0.19	0.0479 ± 0.0120	0.44	0.3255 ± 0.0735	0.99	0.0351 ± 0.0112	0.99
<i>mo-br</i> Vehicle	12	0.0143 ± 0.0085	< 0.01	0.0621 ± 0.0221	< 0.01	0.0300 ± 0.0065	< 0.01	0.1298 ± 0.0278	< 0.01	0.0070 ± 0.0039	< 0.01
10 Weeks		Organ Weights (g)									
Cohort	n	Thymus		Lungs		Kidney		Liver		Spleen	
		Mean	p-value	Mean	p-value	Mean	p-value	Mean	p-value	Mean	p-value
WT Vehicle	8	0.0494 ± 0.0079	-	0.2073 ± 0.0143	-	0.1883 ± 0.0351	-	1.3956 ± 0.0823	-	0.0879 ± 0.0057	-
WT ES-Cu ²⁺	7	0.0459 ± 0.0110	0.98	0.1988 ± 0.0137	0.44	0.2009 ± 0.0160	0.59	1.3937 ± 0.0713	0.99	0.0936 ± 0.0054	0.01
<i>mo-br</i> ES-Cu ²⁺	13	0.0497 ± 0.0161	0.45	0.1751 ± 0.0335	< 0.01	0.1818 ± 0.0308	0.89	1.2178 ± 0.1270	< 0.01	0.1162 ± 0.0348	0.03

CHAPTER IV
TESTING OF NOVEL COMPOUNDS AGAINST MYCOBACTERIUM
TUBERCULOSIS INFECTED

INTRODUCTION

Treating Tuberculosis Infection

There is currently no high efficacy vaccine for *Mtb* despite many attempts including vaccination with BCG, *Mycobacterium Bovis* , as well as with attenuated *Mtb*[1]. The BCG vaccine was used for the first time in 1921[1]. Using attenuated *Mtb* in an attempt to trigger an immune response was unsuccessful, but led to the BSL-2 auxotrophic strains used in research today[2]. The pitfalls of an attenuated strain being so weak that it fails to elicit an immune response as a vaccine are also critical to ensuring those strains of *Mtb* are safe enough for use in research under BSL-2 conditions. Research found that non-human primates with simian immunodeficiency virus (SIV), the non-human primate variant of human immunodeficiency virus (HIV), were still unable to be infected with attenuated *Mtb* despite SIV having destroyed the non-human primate immune system[3].

A typical course of treatment will last for 6+ months[4]. Providing consistent access to care for that length of time creates a global problem, especially in less developed countries. Infected persons may feel better and stop treatment, allowing the infection to flair back up and be spread. The consequence of individuals feeling as though the infection has been treated is compounded when regionally, individuals are required to travel long

distances to get more medication. Taking time away from work to travel for medical care has a significant economic impact on that individual and their families (e.g. choosing between continuing antibiotics or putting food on the table).

Currently, there are only 10 drugs that are Food and Drug Administration (FDA) approved for *Mtb* treatment, plus 2 fluoroquinolones and 5 others in clinical trials for treating *Mtb* infections[5]. *Mtb* has the ability to mutate and form drug resistance relatively easily[6, 7]. Unfortunately, this is not just a speculative concern and the development of drug resistant *Mtb* is so extensive that the categories of multi-drug resistant (MDR) and extremely drug resistant (XDR) *Mtb* were created and are used commonly in *Mtb* research[6, 7].

To combat an individual infection without fully characterizing the strain of concern first, something that would delay the start of treatment, a multi-drug therapy is used. Multi-drug treatments are also used as a means of preventing the development of *Mtb* strains with additional drug resistance, making *Mtb* harder to treat globally[6]. By using multiple drugs simultaneously, the development of resistance to any particular drug will not prevent the other drugs from killing the *Mtb*, thus curing the infection in the host and preventing dissemination of any newly resistant strain of *Mtb*.

Tuberculosis Biosafety Level

Laboratory *Mtb* is likely to provide the most useful data if maintained in as close to a natural environment as possible, as could be said for any infectious agent. To balance safety, speed, cost, and applicability to clinical conditions, auxotrophic strains were

developed to allow work with viable *Mtb* in a BSL-2 working environment[2]. Auxotrophic strains were created that had multiple deletions affecting multiple independent pathways of essential metabolic genes e.g.. Δ RD1 Δ panCD. RD1 is region of difference 1 and is associated with increased virulence in *Mtb*[8]. *PanC* and *PanD* are sequential in the process of synthesizing pantothenate (Pan), not only requiring Pan addition for culturing, but also ensuring that even if a mutation causes an effective complementation of *PanC* or *PanD*, the other is still deleted and Pan supplementation is still required[2].

Mycobacterium tuberculosis (*Mtb*) from nature is classified as biosafety level 3 (BSL-3) due to its lethality and transmissibility. BSL-3 work is inherently slower and more expensive than comparable research at lower BSL-2 and BSL-1 levels. This is due to security, oversight, safety equipment, and a bias towards disposables. Of equal importance is safety to scientists, biosafety personnel, facility management, and equipment repair technicians. The cost is also amplified for a research group doing some work outside of BSL-3 conditions due to the need for redundant equipment. BSL-3 equipment is dedicated to that space and cannot realistically be moved or used for BSL-2 work. This is because trying to sterilize the inside of most electronic equipment is not feasible. As a general rule, with minimal exceptions, materials that go into a BSL-3 space, come out through an autoclave. Adding animals to the research project (ABSL-3) adds several more layers of complexity and cost.

Auxotrophs of *Mtb* have been approved that have regions associated with virulence (e.g.. RD1) but require no supplementation[2]. This type of deletion for the purpose of

downgrading biosafety level is paired with an independent deletion(s) that does require supplementation[2]. Some examples of essential nutrient pathways that are commonly interrupted are vitamins and amino acids[2, 3]. In summary, attenuated strains are not sufficient for a biosafety downgrade unless they a completely independent KO that inhibits virulence, with all downgraded BSL-2 *Mtb* strains having independent deletions in 2 independent pathways at a minimum.

By deleting genes from multiple independent pathways, it is highly unlikely that BSL-2 *Mtb* would be able to undergo a mutation which resulted in a loss of essentiality for a given metabolic molecule, and then to propagate that resilience to any progeny. The required second genetic modification, provides viability limitations. When required supplement(s) are not added, no growth on plates or liquid culture is observed (data not shown).

Due to the plethora of options available for BSL-2 *Mtb* strains, a particular pathway of interest can still be tested using strains designed for BSL-2 work without deleting genes from the target pathway. No current examples of research or types of experiments performed using BSL-2 *Mtb* have been identified to have shown different results compared to having performed the same experiment using non-attenuated, BSL-3 *Mtb*. It should be noted that, as a severe limitation, BSL-2 *Mtb*, while useful for *in vitro* as well as *in cellulo* (infected monocytes or lung epithelial tissue) experimentation, is not feasible to be used for *in vivo* modeling or efficacy testing due to inability of said strain to remain viable. As part of the reduced containment approval requirements, the attenuated strains were tested in healthy animals as well as those with a compromised immune

system[2]. Under both scenarios, the attenuated *Mtb* strains which Dr. Bill Jacob's lab was seeking approval for use under BSL-2 conditions were unable to grow *in vivo*[2]. For all the reasons listed above, the use of BSL-2 *Mtb* provides much in the way of safety, time, and lower cost until the project requires infected animal model samples or data and ABSL-3 must then be used.

Methods to determine Anti-Tubercular Efficacy

There are five common methods for conducting efficacy screens against *Mtb*. While each method has its own pros and cons. The major factors under consideration, as each approach was investigated, were read/analysis time, length of wait for results, cost, applicability to *in vivo* and *in cellulo* experiments, and reproducibility of results. All methods, except colony forming units (C.F.U.) counting, require the use of a plate reader for fluorescence, absorbance, or luminescence. The high content analysis (HCA) approach is still read from a plate, but with much more data being collected beyond just a single value for each well. An image of a section on the well, related to magnification, is taken. The image can be bright field, fluorescence, or any combination including multiple images of different areas within each well.

Colony forming units (C.F.U.) is the gold standard for examining viability[9]. It is a direct measurement of bacterial growth, whereas other methods use some type of indirect reporter instead that is designed to be representative of growth (e.g. mCherry or GFP fluorescence). Papers attempting to validate new types of reporters often compare their method to C.F.U. as proof of any advantage[9]. C.F.U. counting is also used to confirm

other reporter methods[10]. To determine C.F.U., agar plates are seeded with liquid culture at a controlled dilution and then counted to determine the impact on growth of the preceding experimentation. A machine such as a spiral plater can be used to reduce variability, and plate a reproducible gradient. Plates may also include compounds of interest. The major downside of this approach is the need to store many plates for weeks before significant sized colonies are visible for counting.

Using 600nm optical density (OD), the amount of *Mtb* in a liquid culture can be read. An OD of 1.0 indicates approximately 31.3 million cells per milliliter[11]. OD can be used to measure doubling time. This approach is fast, in that it requires no incubation time or additional reagents. While strictly looking at absorbance, samples can be read in a plate format using the same plate reader useful for 3 of the 5 listed techniques. Absorbance does correlate to the concentration of *Mtb* but is only useful for higher concentrations of *Mtb* such as 100s of millions of cells per mL of culture because the linear range of a spectrophotometer measuring OD is typically from 0.1 to 1.0, meaning that without dilution or concentration there must be millions of cells per milliliter for OD to be useful. Due to its lack of sensitivity and susceptibility to be impacted by other debris that impacts OD at 600nm, OD is a poor means for looking at drug efficacy against *Mtb*. For experiments using a monolayer of mammalian cells infected with *Mtb* in a 96-well plate, depending on multiplicity of infection (MOI), there will be 10s of thousands of *Mtb* cells or less making OD not sensitive enough to produce qualitative data on compound efficacy directly.

A more sensitive approach is that of the dye resazurin. Resazurin is metabolized inducing a shift in color affecting absorbance and fluorescence[12]. It can be read using absorbance or fluorescence although fluorescence is the more sensitive approach[12]. The readout is quick and can be made in hours to days as opposed to the weeks necessary for CFU counting. One significant downside is that mammalian cells and bacteria both metabolize resazurin, making it impossible to distinguish between the contribution of the cell types individually. Resazurin is useful in an experiment where it will only be exposed to one cell type, such as a liquid culture *Mtb* screen. Resazurin is cost-effective, readily available, dissolves in H₂O, and is highly reproducible. It is not an endpoint assay that requires lysing of the cells, therefore it allows multiple reads of the same well over time, although the window for repeat measurements will be over a span of hours, but not days as is possible with the upcoming methods.

Constitutively producing a protein based fluorophore (e.g.. GFP or mCherry) is a method used to quantify the amount of *Mtb* in a sample without adding additional reagents[9, 13]. It has the additional benefit of not being an endpoint assay, allowing multiple measurements to be taken over time. Fluorescent reporting bacteria suffer from the weakness that fluorescent proteins don't get degraded at a rate that correlates with *Mtb* viability. Analyzing fluorophore expressing bacteria inside macrophages requires a high-content analyzer (HCA) such as the GE InCell 2000 used in these experiments. Unfortunately, HCA instruments are extremely expensive, take over 10 times longer to read a plate, and require significant computing power to analyze the read (the series of images taken). This, in practice, doubles the time required to collect data and export an

excel table of fluorescent image analysis, being closer to 30 minutes per plate instead of 1-2 minutes in a plate reader. HCA overcomes the issues of resazurin when using infected mammalian cells but has significantly more variability. HCA experiments were found to be most reproducible and with the lowest variability at 5 days after infection. Generally, the shorter the incubation, the less the fluorescent output of replicate wells will show consistency. Alternatively, the longer that THP-1 cells are differentiated and infected with *Mtb*, the more likely it is that the macrophages may be overcome by *Mtb* resulting in lysis and releasing viable *Mtb* to grow unhindered in solution.

Luciferase Assays Using Auto-luminescence

Luciferase *Mtb* infected macrophage assays have existed for decades[14]. These assays showed some significant improvements over other approaches, but at the time still required external luciferin to be added. By adding the luxCDABE operon to the luciferase expression plasmid, lysing the cells and then adding relatively expensive reagents was no longer necessary[15, 16]. The combination of intracellular enzyme and substrate expression for luminescence assays was previously being used for biological investigation, but lent itself well to adaptation into a high-throughput screening (HTS) assay[10]. Despite the fact that luciferase use for a viability readout showed promise over other methods, the necessity to add substrate generally kept the focus on using and improving fluorescent approaches. By eliminating the step of adding substrate, cost and throughput were drastically improved. The assay is no longer an obligatory end-point assay, allowing for the collection of multiple measurements from a single sample over

time. This further reduced variability when multiple time-points are required, compared to lysing a different set of wells for each time point instead of being able to read the same well, eliminating influence from well-to-well variation on a time course of data collection. Well-to-well variability will still effect biological replicates.

To develop a method that utilizes the benefits of both previous luciferase approaches and fluorescent assay designs, an improved luciferase assay was developed. A common requirement for luciferase assays is that the cells be lysed, and then a luciferase substrate is added, saturating the luciferase produced by the cells. There is a limited window in which reproducible data can be collected, usually 10-30 minutes. That is an endpoint assay, and by adding the enzymes necessary to produce a substrate for the luciferase to the plasmid, cells can be read multiple times with no reagent addition necessary [10, 16]. Due to the fact that this assay is constantly utilizing substrate as fast as it is produced, the signal is significantly lower than luciferase based approaches which use external substrate to saturate the biologically produced luciferase. A monolayer in a 96-well format produces significant signal for all modern plate readers tested (Data not shown). This assay has the added benefit of not aggregating protein that can cause misleading results. The substrate is utilized effectively immediately once produced meaning that any signal observed is generated by *Mtb* in its current state of viability and not reminiscent of the cells metabolism prior to exposure to the test conditions. Variability well-to-well is also significantly improved over HCA.

Improving Mtb High-Throughput Screening from Semi-Quantitative to Quantitative

Other methods for examining the toxicity of novel compounds suffer from significant downsides including C.F.U. plating, the gold standard, which takes weeks instead of days, to produce results. Methods such as a resazurin screen aren't possible on infection model studies due to the promiscuity of cells regarding the metabolism of resazurin. Some methods, HCA approaches, require very expensive and large automated microscopes that are slow, but provide intracellular levels of analysis requiring according levels of computing power. This study sought to develop an approach which principally relied on a plasmid producing both luciferase and substrate, giving an infinite number of data points along a time-course, a quick time to producing a stabilized result, and lower variability than comparable approaches. All goals were realized producing consistent results only 3 days after exposure to test compounds.

Cytostatic vs Cytotoxic

One common issue in trying to determine the efficacy of a novel compound against *Mtb* is the ability of *Mtb* to remain dormant for many months, making it hard to determine if the compound of interest is cytostatic or cytotoxic. If the compound is cytostatic, it will appear as if the treatment was lethal by halting growth, although once the compound has been removed, or metabolically cleared from the host, *Mtb* will continue to grow again. This shouldn't be viewed as to imply that cytostatic treatments are without value. While killing *Mtb* in the host is necessary for long-term health, the ability to stop growth of *Mtb*

as quickly as possible once infected persons are identified can inhibit the impact of the infection on the host and stop it from spreading.

To determine if a drug is cytostatic or cytotoxic, a treated sample of *Mtb* can be subsequently cultured under antibiotic-free conditions to determine if any portion of the treated culture is still viable. The luminescence strain could be observed after test compound removal and measure the increase in signal. Alternatively, “live/dead” strains can be used that express one fluorophore constitutively and the other under control of a Tet promoter[17]. After removal of the stress condition, tetracycline is added to see if second fluorophore starts getting translated, indicating that the cell is not dead, but recovering from a cytostatic state.

For characterization of a novel strain, target, or lead compound, this added time may not be of significance. However, through the lens of drug discovery, this added step may cause significant delays in progressing through a compound series, while the efficacy to prevent growth can alternatively be determined using a luciferase assay in a few days. Whether a compound is cytotoxic or cytostatic is likely to be a function of what the target is. As new targets are identified, and HTS is used to identify structural backbones to be used in drug design, cytotoxicity and cytostatic conditions must be identified as well.

Modern techniques such as transposon insertion sequencing (TnSeq) can be used to examine the essentiality of genes in the genome under a given set of conditions[18, 19]. In TnSeq, phage is used to insert the HimarI transposon into TA sites in the *Mtb* genome, ideally into one site per cell, but with a bulk library covering as close to 100 percent of the TA sites as possible. Complete coverage will not be identifiable through sequencing

because essential genes that are disrupted by a Himar1 insertion that causes a loss of function (LoF) will not be represented in the sequencing results, only viable insertions are. It has also been determined that an insertion doesn't necessarily cause a complete LoF[19]. An insertion towards the ends of a gene may cause reduced functionality, or have no impact on functionality [19]. This can be identified when insertions towards the end of a gene are found in TnSeq sequencing results but insertions in the middle of the gene are not.

Determining that a gene is essential through TnSeq is useful as it indicates one of four possibilities:

- 1) The gene is essential, insertions in it are lethal, and the gene would make for a good drug target.

- 2) The library doesn't contain insertions in that gene.

- 3) Insertions in the gene inhibit growth to the point that the sequencing results indicate it is essential, but inhibiting the gene of interest (GoI) with compounds is unable to achieve the level of inhibition required for lethality. The drug isn't living up to its potential due to an inability to achieve high levels of inhibition. A different molecule is necessary, but the extent of change necessary will vary significantly.

- 4) There are indirect effects from disrupting the production of the normal full length gene that are not achievable through steric inhibition which make the GoI a poor target.

With these possibilities in mind, TnSeq is a reliable way to identify potential targets, but requires validation.

The Benefit of Intracellular Screens Prior to Animal Studies

The literature has not identified any compounds that had no effect in liquid culture or intracellular macrophage, but then worked in a mammalian model. Some compounds are only active against the enzyme *in vitro* or against a liquid *Mtb* culture, but lose activity against *Mtb* infecting macrophages or epithelial tissue. This variance of results beyond *in vitro* brings in the variability of mammalian cells. The mammalian cells may metabolize the test compound or it could be excreted from the mammalian cells by a drug pump, preventing sufficient exposure to intracellular *Mtb*.

THP-1 cells offer a unique environment for testing compounds for efficacy against *Mtb* intracellular to a mammalian white blood cell. THP-1, as stored in liquid nitrogen (LN), is a human monocytic cell line with acute leukemia. The cancerous background inserts biological deviation from normality which may or may not affect a particular experiment. THP-1 can be differentiated using phorbol 12-myristate 13-acetate (PMA)[20]. These cells are then referred to as macrophage-like cells.

MATERIALS AND METHODS

Generating the Luciferase Tuberculosis Strain (mc^c7000-Lux)

The plasmid encoding luciferase and its substrate (luxCDABE), as well as the kanamycin resistance gene, optimized for mycobacterium tuberculosis (*Mtb*) was a kind gift from Dr. Robert Watson of Texas A&M Medical School. More information about the plasmid has since been published[10]. A 100mL culture of Mc^c-7000 was washed with a

salt-free buffer and concentrated 50x prior to mixing with the reporter plasmid and then electroporated as described in Methods in Manipulating *Mtb*[21]. After plating on 7H10 with kanamycin for 3 weeks, a single colony was picked and grown into a larger culture from which all stocks in Sacchettini Lab were derived. The mCherry carrying strain was produced by the Parish Lab[13].

THP-1 Drug Efficacy Assay (mCherry and Lux)

Mc²-7000 BSL2 *Mtb* was cultured in roller bottles at 12 RPM and 37C. The liquid media used was Middlebrook 7H9 Broth with 10% OADC, 0.05% Tween-80, 100ng/mL pantothenic acid, and either hygromycin (100ng/mL) or kanamycin (25 μ g/mL) as appropriate. Cells are diluted as necessary to remain in normal exponential growth and below an OD at 600nm of 0.8. Any media with *Mtb*, including HyClone RPMI 1640 with L-glutamine, will have 100ng/mL pantothenic acid, but without penn-strep for RPMI used directly on cultures with *Mtb*.

Immediately prior to THP-1 infection, *Mtb* is placed in a 50mL Falcon tube and sonicated 3 times, 20 seconds off/ 20 seconds on using a probe tip sonicator. The sample was then added to glass beads and vortexed for 5 minutes. This suspension is centrifuged at 50 x g for 5 minutes to pellet any clumps while single *Mtb* cells still remain in suspension. The supernatant is carefully removed from the pellet and then diluted with RPMI to an OD of 0.0083. Spectrophotometers generally only have a linear range from 0.1 to 1.0 so the pellet is first resuspended in a small volume to allow accurate OD readings and then further diluted to the desired OD. Adding 100 μ L/well of this solution to

differentiated THP-1 as described below, results in a multiplicity of infection (MOI) of 1:1.

THP-1 monocytes were differentiated with PMA (100nM) for 3 days prior to infection, seeded at 40k cells/well in 200uL RPMI in a 96-well dish previously coated with 0.1% gelatin for 30 minutes at 37C. Mc²-7000 *Mtb* constitutively expressing mCherry/luciferase were incubated with THP-1 for 2 hours at an MOI of 1:1, washed gently, and incubated with gentamycin (10ug/mL) for 2 hours to kill extracellular *Mtb*. Cells were then washed with PBS and incubated with drug (1% DMSO final).

Fluorescent *Mtb* wells were measured on day 0 and day 5 post infection using a GE InCell Analyzer 2000 at 20x magnification and analyzed using the GE software suite. Fold change in fluorescence (R.F.U.) or luciferase signal (R.L.U.) was normalized to Rifabutin (10uM) as the positive control. For luciferase assays, only a bulk luminescence reading for each well is needed from a conventional plate reader with no further processing other than normalization. All experiments were performed with biological triplicates and represent an average of 3 independent experiments unless otherwise specified.

One variable important for luxCDABE reporter strains, that is not an issue for other reporting approaches, is the requirement to maintain a temperature of 37C for each plate. This is uniquely important for luxCDABE because there is an excess of luciferin, with substrate being the limiting factor. The property of utilizing substrate immediately has several consequences:

- 1) As temperature decreases, so does enzymatic activity. This leads to low signal.
- 2) The signal observed is relative to the sample right now, not an accumulation of effects over time.

- 3) This is not an obligatory endpoint assay because no addition is required to read signal. Each well can be read an unlimited amount of times, providing kinetic response data.
- 4) Signal will be significantly lower than an equivalent assay where cells are lysed and the luciferase is saturated with luciferin with a read window typically between 10-30 minutes.

Reagents

The following data was collected using the *Mtb* strain Mc^c-7000. Mc^c-7000 was generated by the laboratory of Dr. Bill Jacobs[2]. In short, mc^c-7000 is an auxotrophic strain derived from the parent strain H37Rv. It contains deletions of both *RD1* and *panCD*. These deletions make the strain less virulent and require the addition of 100ng/mL of pantothenic acid in both liquid or agar growth environments. The strain does not have any antibiotic resistance. The attenuations allowed for the downgrade in classification from BSL3 to BSL2 working conditions.

Mtb was grown in Middlebrook 7H9 broth or on Middlebrook 7H10 agar. The media was supplemented with 10% OADC (Middlebrook), 100ng/mL pantothenic acid (Sigma-Aldrich), and 0.05% Tween-80 (Sigma Aldrich). When carrying the mCherry plasmid, hygromycin (Goldbio) is used at 100 $\mu\text{g}/\text{mL}$ [13]. The luciferase plasmid adds kanamycin resistance and 25 $\mu\text{g}/\text{mL}$ is used.

Human tissue culture was carried out using standard aseptic culture practices in Cellstar flasks with penicillin-streptomycin (Gibco) at 100 U/mL in HyClone RPMI 1640 with L- Glutamine(Life Technologies) with 10% fetal bovine serum (Wisent Bioproducts). Cells were grown in humid incubators at 37C and 5.0% CO₂. THP-1 were passaged for 2 weeks after reviving from cryopreservation prior to use in an assay for up

to 6 weeks after thawing. Cells were maintained between 200,000 cells/mL and 1 million cells/mL.

For experiments utilizing *Mtb* uptake, THP-1 are seeded in 200 μ L volumes at 40,000 cells/well with 100 ng/mL of PMA (Sigma-Aldrich) for 3 days in Falcon 96-well flat bottom, optically clear plates, using black for mCherry and white for luciferase strains. These plates are first coated with 0.1% gelatin (EMD Millipore). Gelatin is added to tissue culture treated polystyrene to cover the cell adherent surface for 15 minutes in the incubator prior to aspirating gelatin and adding cells. When extracellular volumes are washed free of *Mtb*, the wells are replaced with fresh RPMI containing gentamycin (Invitrogen) at 10 μ g/mL for two hours. Gentamycin is used to kill any extracellular *Mtb* not taken up by mammalian cells, or washed away during a media change[12]. Novel compounds are dissolved in DMSO (VWR Scientific) with a final concentration of 0.2%-1% (1% unless noted).

Z'-Factor Calculation

According to Collaborative Drug Discover software, used to statistically evaluate and plot data, Z-score calculation is used to calculate the extent of deviation of an individual sample from the mean (μ) and standard deviation (σ) of a sample population or from the negative control (n). Z-factor is used to compare a sample's standard deviation and mean to that of the positive control (p). All Z'-factors used in this work are a comparison of the positive and negative controls using the following formula:

$$Z' \text{ factor} = 1 - \frac{3 \times (\sigma_p + \sigma_n)}{|\mu_p - \mu_n|}$$

RESULTS

Legacy Fluorescence Based High-Throughput Screening

While using C.F.U. will likely always serve a role in *Mtb* drug discovery research, faster approaches for screening are necessary to facilitate productivity. The initial method being used was with Mc²-7000 with a fluorescent reporter plasmid. Mc²-7000 is a BSL-2 auxotrophic strain requiring the addition of pantothenate because of *PanC* and *PanD* deletions. The nutrients that the auxotrophic strain requires are not found inside mammalian cells in sufficient concentrations for the *Mtb* to survive, preventing accidental infection. Mc²-7000 additionally has an *RDI* deletion to hinder its virulence. The fluorescent strain used for testing has the addition of hygromycin resistance and constitutively expressed mCherry[13].

For a round of experimentation, it takes 7-8 days prior to collecting the final data. This is still a huge improvement over lysing the mammalian cells in the well and plating the lysate for C.F.U. Despite the significant improvement in the length of the experiment, the assay still suffers from several pitfalls. Bulk fluorescence is not read, but instead a high content analyzer, in this case a GE InCell 2000, is used.

Ultimately this is a much larger and more expensive instrument compared to a traditional plate reader and can only process about 3 wells per minute. Depending on settings, a 96-well plate takes 1-3 minutes in a plate reader. There was also a large and unacceptable amount of variability, especially when weaker inhibitors are tested. This can

be seen in Figure 1 and should be noted that the observed variability makes ranking analogs in a compound series very difficult.

The inherent variability in this assay is worsened by the reporting method. The fluorophore used in this strain, mCherry, degrades more slowly than many of the novel compounds inhibit growth, leading to falsely elevated levels of viability (as determined by fluorescence). There are aspects of the experiment that could have been improved while still generally taking the same approach. The mCherry being expressed could have included a PEST sequence, causing faster degradation[22]. The analysis software could also possibly be further optimized.

Real-Time Metabolism Reporting Using Luminescence

In an attempt to overcome the issues inherent to the strain of *Mtb*, while simultaneously improving the reporter used in *Mtb* intracellular to mammalian cells for screening, a different approach to reporting was taken. The luciferase system utilized was similar to the mCherry construct in that they were both self-contained, not requiring the addition of any additional substrate, and neither was an obligatory endpoint assay. Both allow an unlimited number of reads that can be taken. Both assays are stable over the period of minutes, especially under constant conditions so measuring over time hasn't been necessary for quality data.

In Figure 2, one can see that the luminescence strain, called Mc³-Lux (or just Lux) has immediately shown a great improvement. The Lux strain is improved in two fundamental ways: The viability from dose responses of both strong and weak compounds

indicates as expected, with higher concentrations having more inhibition than lower concentrations of the same compound. Also, the phenomenon where lower concentrations of inhibitors lead to higher variability between replicates has been minimized. An important factor to be considered is that due to the luciferin substrate being utilized immediately, instantaneous metabolism is highly important, but lowers with temperature. This requires plates to be maintained at 37C until the completion of reading that sample.

To better quantify the improvement, Figure 3 shows an overlay of the previously discussed data. All three compounds tested had at least one concentration in which the variability was so high that the data is not informative. Testing with such a large amount of data requires a dose response to determine the range of concentrations that cause inhibition. It also requires biological replicates to determine the extent of variation being observed at any given concentration. The mCherry plate had a Z'-factor of -0.88, indicating that the variability likely masks any useful data. The Lux plate had a Z'-factor of +0.78, indicating that this assay is suitable for use in high throughput screening (>0.50). The same drug plate was tested again in duplicate with fresh THP-1 and Lux to validate the Z-Factor and achieved 0.78, 0.68, 0.80, and resulting in an average of 0.75, all shown in Figure 4.

As mentioned previously, conditions with the lowest inhibition, often exhibit the highest variability between biological replicates. In Figure 5, a comparison of two plates of THP-1 macrophage-like cells infected with either Lux or mCherry *Mtb* shows that under the conditions of the highest variability (no drug) showed Lux having 20% less

variability than the mCherry fluorescence strain had. Figure 5.C. shows how drugs with stronger inhibition (red) have lower variability in biological triplicates.

Time Versus Precision

Despite the fact that THP-1 and mc²-7000 were still both being used in the new assay, there were significant differences in the reporting system. This logically led to exploring different times for incubation with compound. A shorter incubation leads to a quicker turn around. While all 3 days examined in Figure 6 show adequate results. Some drug-concentration combinations lead to any increased inhibition from day 3-5 while others lose inhibition over time. During a high-throughput screen this additional information may not be necessary, but multiple time-points are available without significant modification to the protocol if a deeper characterization of the compound is desired. Using 4 days of infection to compare to literature values for some known drugs shows that this assay is in line with literature values. Isoniazid (INZ) has a literature MIC₅₀ of 630nM and 233nM while my assay showed 181nM[23]. Likewise, Ethambutol (EMB) has a literature reported MIC₅₀ of 4.89uM, while I determined it to be 1.62uM [23]. Rifabutin (RBT) is a potent anti-tubercular with a literature MIC₉₀ <35nM, while I found the value to 17nM[24]. There is a significant amount of variability in the literature regarding (MOI) from 1-10 as well as variation in incubation time. Literature values were for the H37Rv strain (BSL-3), while my results are from Mc²7000. I used the macrophage like cell line of THP-1 differentiated from monocytes. The literature varied using either THP-1 or murine RAW264.7 macrophages. Despite all of the variables, I still determined

efficacy to be less than one order of magnitude from reported values using luciferase reporting.

In a recent paper, PKS-13 was targeted with a novel compound series based on crystallography results and (SAR) results[12]. The series was tested with intramacrophage results contributing to the evaluation of each molecule. MKP-184 (10uM) consistently shows 68.5% (± 9.1) inhibition and (1uM) shows 59.6% inhibition (± 2.5) when compared to RBT (10uM) while testing for efficacy against intracellular *Mtb* in THP-1 macrophage-like cells[12]. This study reaffirms that this luciferase based efficacy model reflects results reported in the literature while also being effective for SAR studies. With this assay only taking 3 days for a reliable result, it does not significantly slow down the drug development process while it does provide a modicum of information regarding whether the drug/compound will continue to show efficacy in *in vivo* models.

The Necessity of Intermediate Assays

Testing novel compounds against strains of *Mtb* in liquid culture is common and facilitates a much higher throughput than C.F.U. counting would allow. C.F.U. counting also takes weeks to produce colonies, instead of results in days with a luciferase report strain, while also eliminating the need to lyse macrophages and plate the remaining *Mtb* on 7H10 agar. THP-1 and Lux *Mtb* were being used to evaluate novel compounds which had exhibited inhibition against liquid *Mtb* culture, (Figure 7). Although this dose response in THP-1 indicated poor efficacy, other aspects of that compound series and of this compound, RCD-110, led to it being tested *in vivo* (Figure 8). Unfortunately, RCD-110

failed to show efficacy in the mouse model (Figure 9). Additionally, this compound showed a wide range of efficacy *in vitro* depending on the carbon source (Data not shown). When the compound was tested against *Mtb* in a more complex carbon source environment, efficacy was reduced.

This does reinforce the idea that this assay can be effectively used to rank a series of very similar in structure compounds. It is also useful for identifying compounds with metabolic vulnerabilities to structure modification *in vivo* under more biologically relevant environments. This is still only one aspect that will be used, as seen in Figure 8, there are many important aspects. In Figure 8 it can also be seen where RCD-110 had shown toxicity to HDFs (human dermal fibroblasts). Fortunately, RCD-110 is also very potent against *Mtb* and so a sufficient therapeutic window existed with this compound despite HDF cytotoxicity to the compound.

This current form of “macrophage” *Mtb* assay has significant improvements over other methods, but most important is the quality of the data. Figure 10 shows how the assay performs against compounds at dilutions of reduced inhibition while still minimizing variability.

DISCUSSION

If this macrophage, luciferase *Mtb* uptake assay is truly to be used to select which compounds move forward to *in vivo* testing, then it is extremely important that the assay is both precise and accurate. The currently underutilized system produces both luciferase and substrate so that lysis isn't required and has the option of being run as an endpoint or

kinetic assay has shown to be a consistent improvement on the quality of data as compared to using HCA. As seen in Figure 10, the assay has much more acceptable levels of deviation, even at lower levels of inhibition. Using this assay provides another layer of data while ultimately saving time, money, and required number of animals necessary.

Using this luciferase based assay where the cell is co-opted into making its own substrate allows for an infinite number of real-time reads. This is a distinct difference from common modern luciferase readout systems where the subject cells are lysed, then saturating the available luciferase as a surrogate for cell level prior to lysing.

This luciferase approach not only saves time and money by containing everything necessary in the reporter cell line, but it also allows signal from the intracellular *Mtb* to be measured without lysing. This has several advantages, one of which is that it produces its own substrate[10]. In traditional luciferase based assays, when sufficient time has occurred and a particular well is ready for measurement and analysis, the cells of interest need to be lysed, at which point luciferin is added and luminescence is measured. This is an end point assay, with readings from the lysate being possible for 10-30 minutes at a stable level as long as substrate can keep the luciferase saturated.

Lux uses the luxBCADE operon to produce both luciferase and the enzymes necessary for form the substrate tetradecanal[16]. Compared to a traditional luciferase reporter, this self-contained system will have a much lower signal. In this new form, the enzyme is in excess causing all substrate to be used immediately. In this case, the amount of substrate produced is indicative of viability and metabolic activity. In the traditional assay, the amount of luciferase was proportional to the number of cells producing it and

after lysis, the enzyme is saturated with luciferin to produce that large signal until the substrate is exhausted.

The better alternative to THP-1 would be to use bone marrow derived monocytes from mice or to use blood derived monocytes from humans. The ability to collect human samples, and the short time frame of viability for use, being primary cells and not cancerous like THP-1 cells are, make their use for regular and high-throughput work impractical. In the infected macrophage model, the purpose is to determine whether or not intracellular *Mtb* will be affected despite the compound needing to pass into THP-1 and not be modified by the mammalian cell. There has not been a time where the assay predicted loss of efficacy, but the compound showed efficacy in an animal model. Although it has been reported by some labs, a literature review identified no cases of drugs that didn't work against BSL-3 *Mtb* inside macrophages but then killed effectively *in vivo*.

Conversely, there is always the chance that a compound showing efficacy against intracellular *Mtb* will not be effective in an animal model. Moving forward it should be further explored if a panel of cell lines commonly known to take up *Mtb* could significantly further reduce the chance that a compound passing *in cellulo* screening and *in vivo* pharmacokinetics but then would fail an *in vivo* efficacy study.

REFERENCES

1. Schragger, L.K., et al., *The status of tuberculosis vaccine development*. The Lancet Infectious Diseases, 2020. 20(3): p. e28-e37.
2. Sambandamurthy, V., et al., *Mycobacterium tuberculosis RD1 panCD: a safe and limited replicating mutant strain that protects immunocompetent and immunocompromised mice against experimental tuberculosis*. Vaccine24: 6309–6320. 2006.
3. Sampson, S.L., et al., *Extended safety and efficacy studies of a live attenuated double leucine and pantothenate auxotroph of Mycobacterium tuberculosis as a vaccine candidate*. Vaccine, 2011. 29(29-30): p. 4839-4847.
4. Gelband, H., *Regimens of less than six months for treating tuberculosis*. Cochrane Database of Systematic Reviews, 1999(4).
5. Egelund, E., A. Alsultan, and C. Peloquin, *Optimizing the clinical pharmacology of tuberculosis medications*. Clinical Pharmacology & Therapeutics, 2015. 98(4): p. 387-393.
6. Laurence, Y.V., U.K. Griffiths, and A. Vassall, *Costs to health services and the patient of treating tuberculosis: a systematic literature review*. Pharmacoeconomics, 2015. 33(9): p. 939-955.
7. Mahajan, R., *Bedaquiline: First FDA-approved tuberculosis drug in 40 years*. International journal of applied & basic medical research, 2013. 3(1): p. 1-2.
8. Kurenuma, T., et al., *The RD1 Locus in the *Mycobacterium tuberculosis* Genome Contributes to Activation of Caspase-1 via Induction*

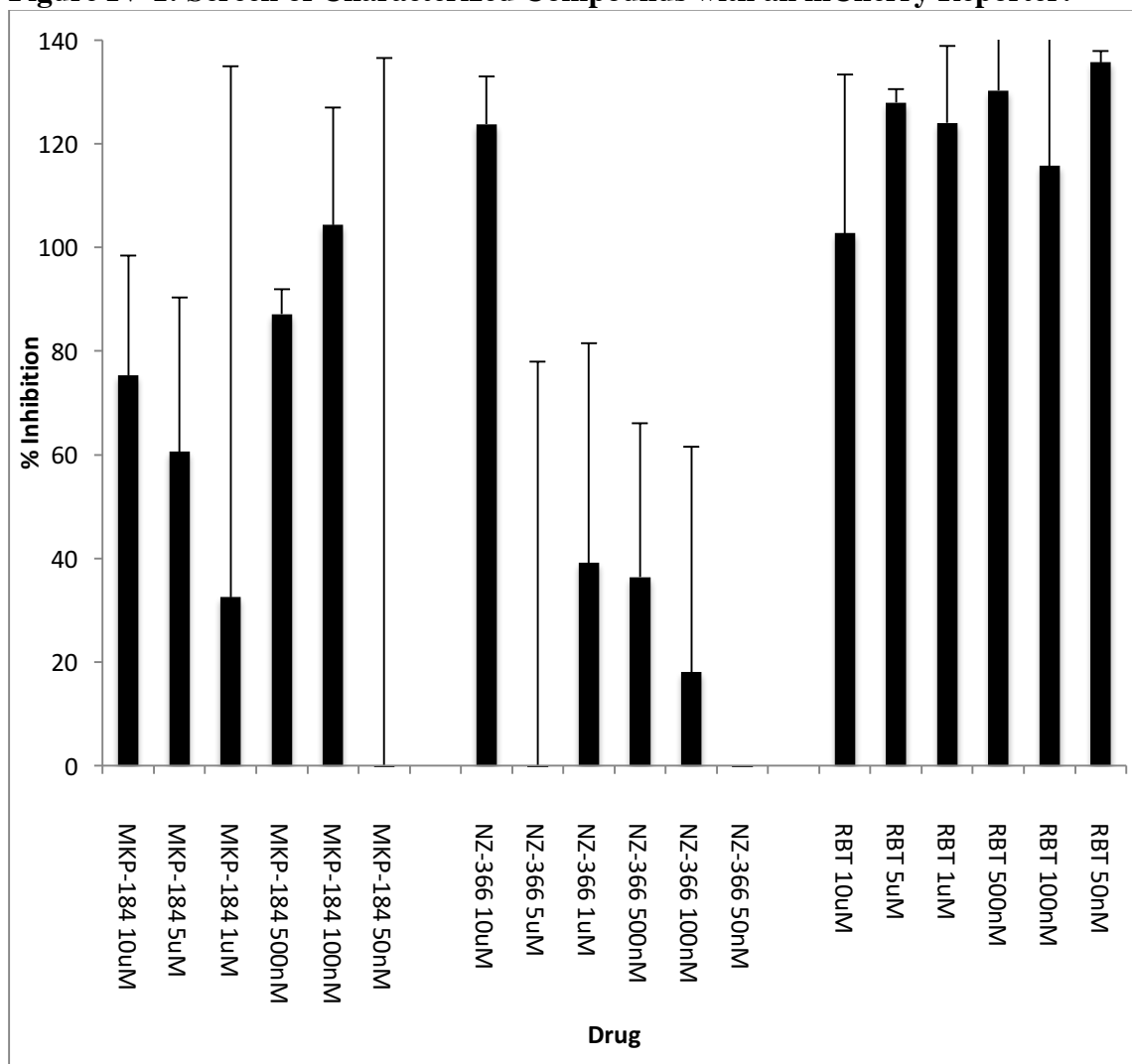
- of Potassium Ion Efflux in Infected Macrophages*. Infection and Immunity, 2009. 77(9): p. 3992-4001.
9. Collins, L.A., M.N. Torrero, and S.G. Franzblau, *Green Fluorescent Protein Reporter Microplate Assay for High-Throughput Screening of Compounds against *Mycobacterium tuberculosis**. Antimicrobial Agents and Chemotherapy, 1998. 42(2): p. 344-347.
 10. Penn, B.H., et al., *An Mtb-Human Protein-Protein Interaction Map Identifies a Switch between Host Antiviral and Antibacterial Responses*. Molecular cell, 2018. 71(4): p. 637-648.e5.
 11. Peñuelas-Urquides, K., et al., *Measuring of Mycobacterium tuberculosis growth. A correlation of the optical measurements with colony forming units*. Brazilian journal of microbiology : [publication of the Brazilian Society for Microbiology], 2013. 44(1): p. 287-289.
 12. Aggarwal, A., et al., *Development of a novel lead that targets M. tuberculosis polyketide synthase 13*. Cell, 2017. 170(2): p. 249-259. e25.
 13. Carroll, P., et al., *Sensitive detection of gene expression in mycobacteria under replicating and non-replicating conditions using optimized far-red reporters*. PloS one, 2010. 5(3): p. e9823.
 14. Arain, T.M., et al., *Reporter gene technology to assess activity of antimycobacterial agents in macrophages*. Antimicrobial Agents and Chemotherapy, 1996. 40(6): p. 1542-1544.

15. Craney, A., et al., *A synthetic luxCDABE gene cluster optimized for expression in high-GC bacteria*. Nucleic acids research, 2007. 35(6): p. e46-e46.
16. Andreu, N., et al., *Optimisation of bioluminescent reporters for use with mycobacteria*. PloS one, 2010. 5(5): p. e10777.
17. Bryson, B.D., et al., *Heterogeneous GM-CSF signaling in macrophages is associated with control of Mycobacterium tuberculosis*. Nature communications, 2019. 10(1): p. 1-11.
18. Griffin, J.E., et al., *High-resolution phenotypic profiling defines genes essential for mycobacterial growth and cholesterol catabolism*. PLoS Pathog, 2011. 7(9): p. e1002251.
19. Zhang, Y.J., et al., *Global assessment of genomic regions required for growth in Mycobacterium tuberculosis*. PLoS Pathog, 2012. 8(9): p. e1002946.
20. Takashiba, S., et al., *Differentiation of monocytes to macrophages primes cells for lipopolysaccharide stimulation via accumulation of cytoplasmic nuclear factor κ B*. Infection and immunity, 1999. 67(11): p. 5573-5578.
21. Larsen, M.H., et al., *Genetic manipulation of Mycobacterium tuberculosis*. Current protocols in microbiology, 2007. 6(1): p. 10A. 2.1-10A. 2.21.
22. Wang, N., et al., *A PEST sequence in ABCA1 regulates degradation by calpain protease and stabilization of ABCA1 by apoA-I*. The Journal of clinical investigation, 2003. 111(1): p. 99-107.
23. Larsson, M.C., et al., *A luciferase-based assay for rapid assessment of drug activity against Mycobacterium tuberculosis including monitoring of*

macrophage viability. Journal of microbiological methods, 2014. 106: p. 146-150.

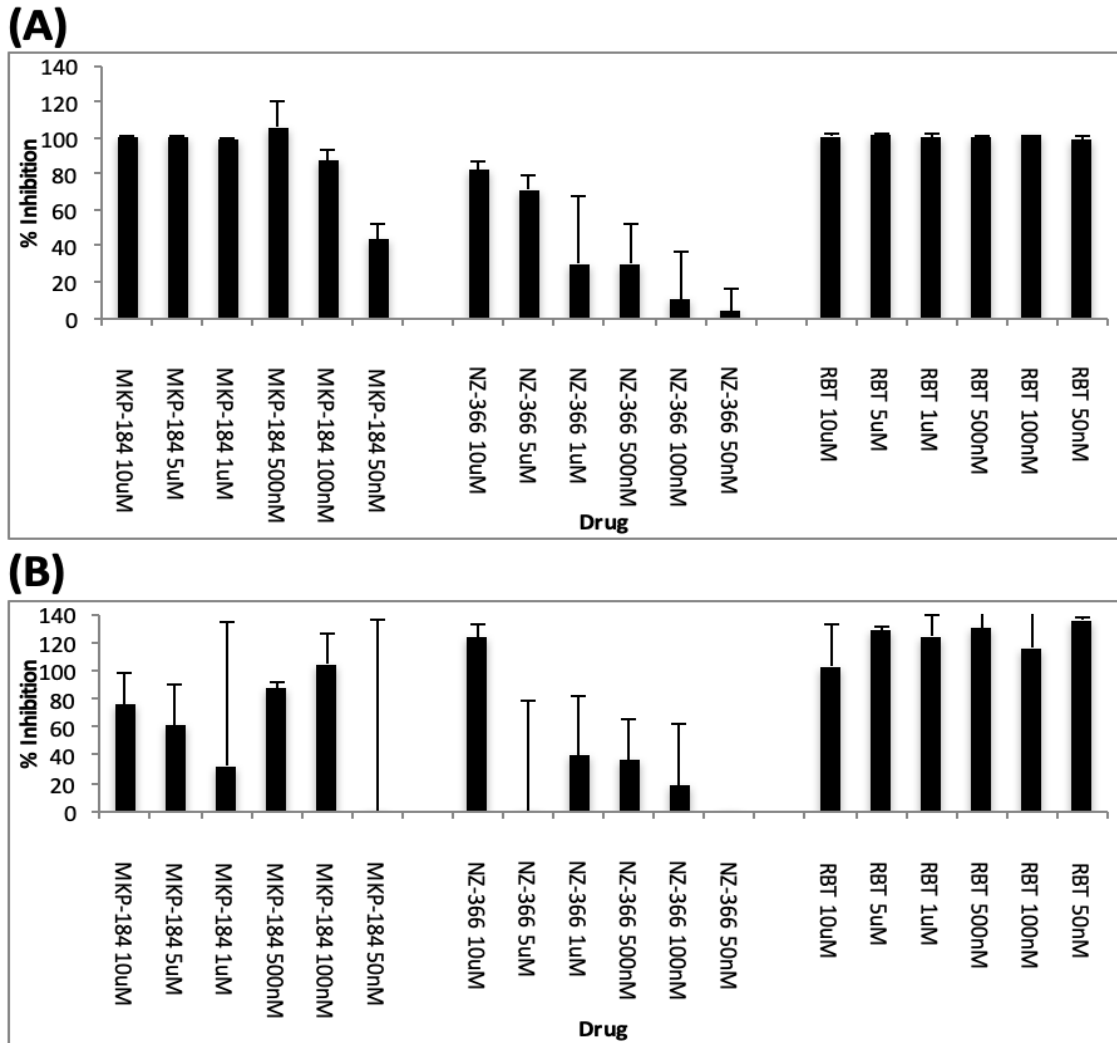
24. Lakshminarayana, S.B., et al., *Comprehensive physicochemical, pharmacokinetic and activity profiling of anti-TB agents*. Journal of Antimicrobial Chemotherapy, 2015. 70(3): p. 857-867.

Figure IV-1: Screen of Characterized Compounds with an mCherry Reporter.



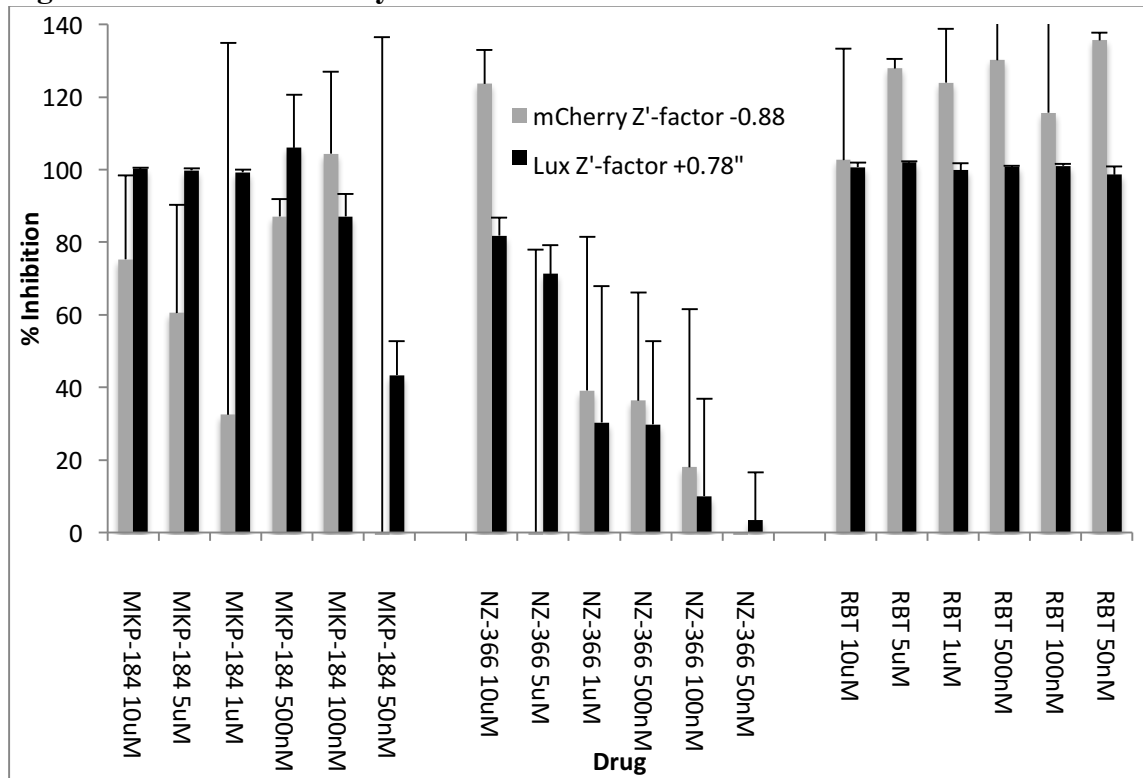
THP-1 cells were infected in triplicate with mCherry expressing *mTB* in the presence of drug for 5 days. Inhibition is the change in fluorescent signal compared to controls of 0.5% DMSO and 10uM rifabutin. Error bars represent 1 standard deviation. Data is collected and analyzed using High Content Analysis (HCA) on a GE InCell 2000. Variability in this style assay often masks results through poor signal-to-noise ratios (S/N). The variability increases under conditions with low levels of growth inhibition.

Figure IV-2: Comparing Reporter Cell Lines.



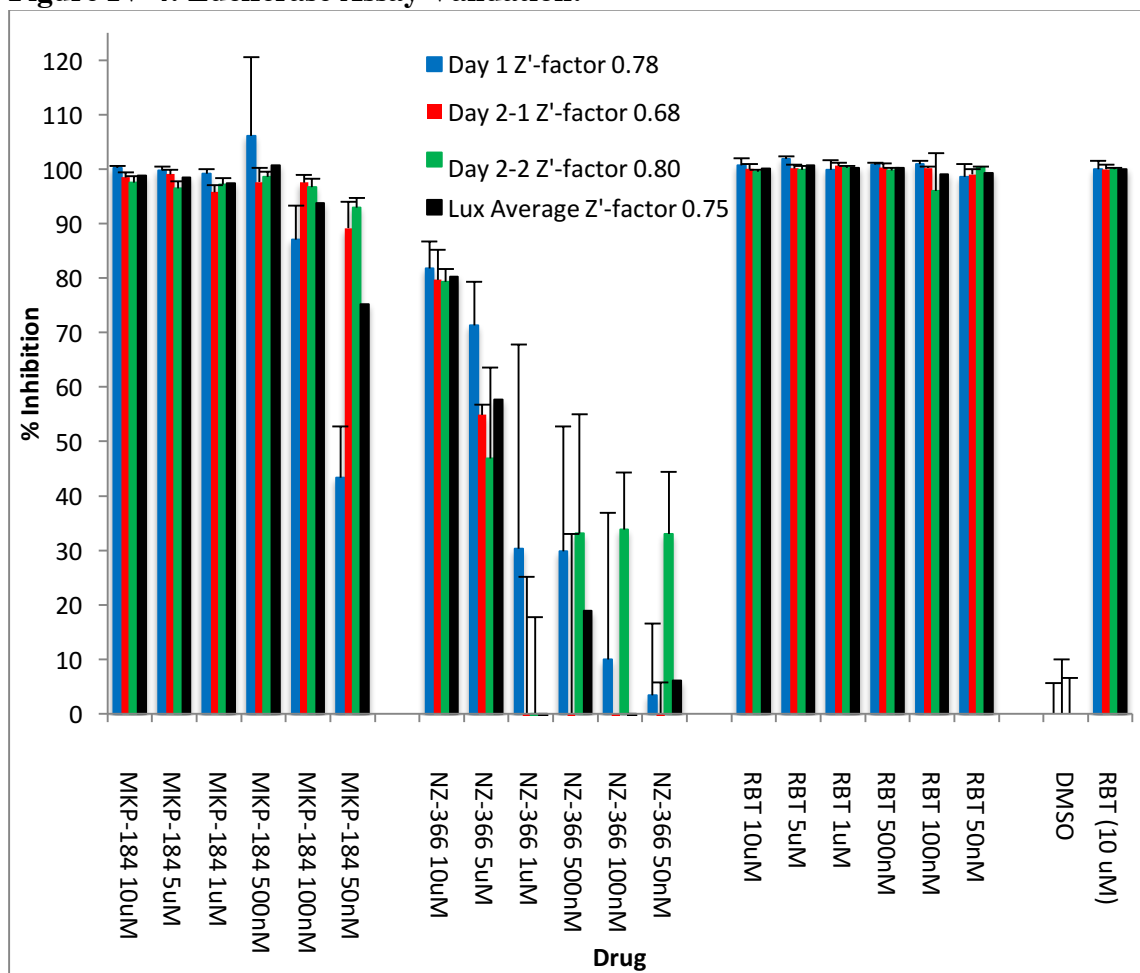
Optimization of the constitutively expressing mCherry variant of Mc-7000 was insufficient in improving S/N. Error bars represent 1 standard deviation. (A) an alternative reporter expressing both luciferase and its substrate simultaneously was compared to (B) the mCherry reporter strain with Lux showing an improvement in variability and reproducibility. Each condition was tested in triplicate on THP-1 infected with the noted strain. NZ-366 at 1uM was chosen for student's t-test evaluation but the sample size of N=3 was too small for reliable calculation.

Figure IV-3: Z'factor Analysis.



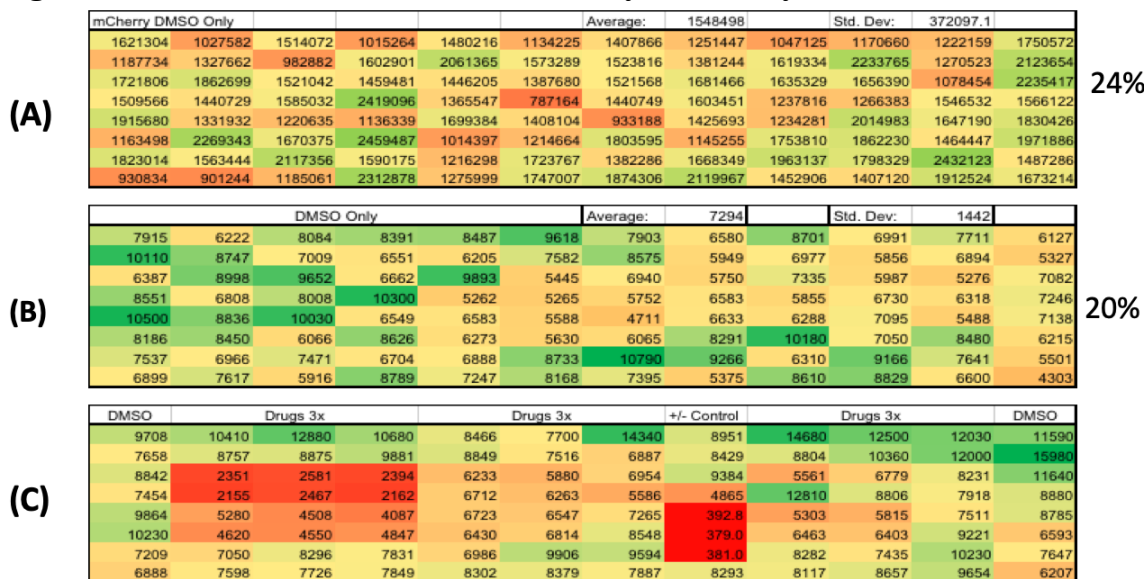
THP-1 cells infected with the noted strain of *Mtb* were tested in triplicate. Error bars represent 1 standard deviation. After determining the optimal parameters for use in the protocol for the luciferase based assay, the Z'-factor was determined -0.88 for mCherry and +0.78 for luciferase. Based on the Z'-factor for each strain the luciferase assay is quantitative while the mCherry assay is not. A Z'factor of +0.50 is the threshold for a reliable high throughput assay.

Figure IV-4: Luciferase Assay Validation.



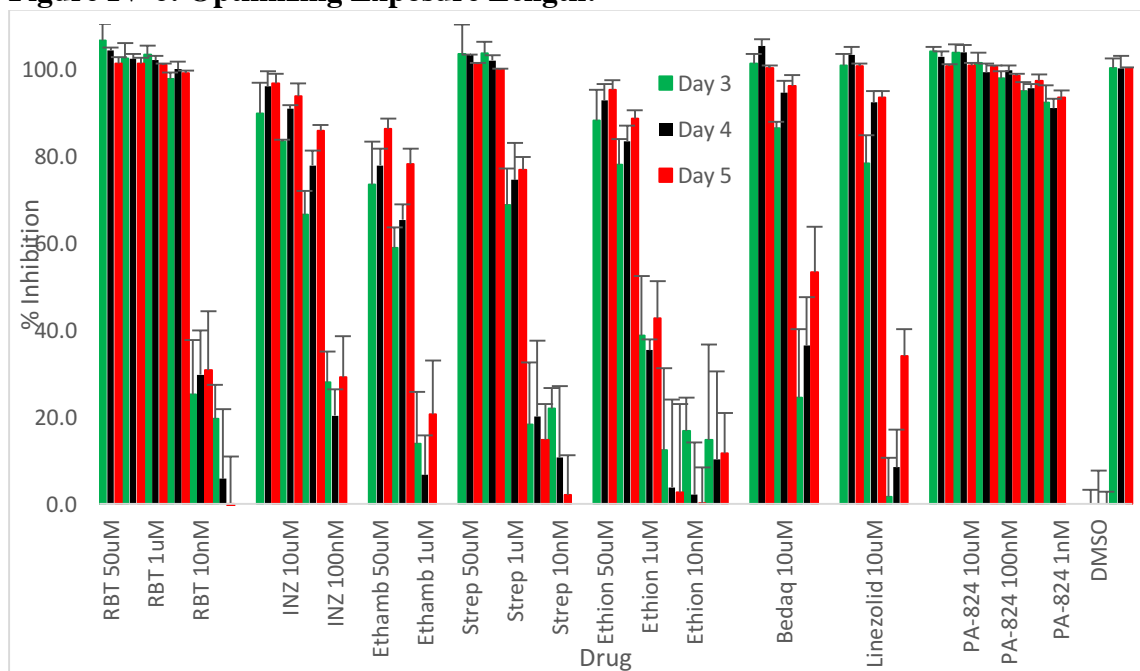
To confirm the large extent in which the data was improved, the assay was run in triplicate on multiple plates the same day, as well as a completely separate plate on a different day with independently cultured human and bacterial cells. Error bars represent 1 standard deviation. The luciferase version of the macrophage infection model has an average Z'-factor of +0.75 and ranges from +0.68 to +0.80.

Figure IV-5: Mc-7000-Lux Intracellular Assay Variability.



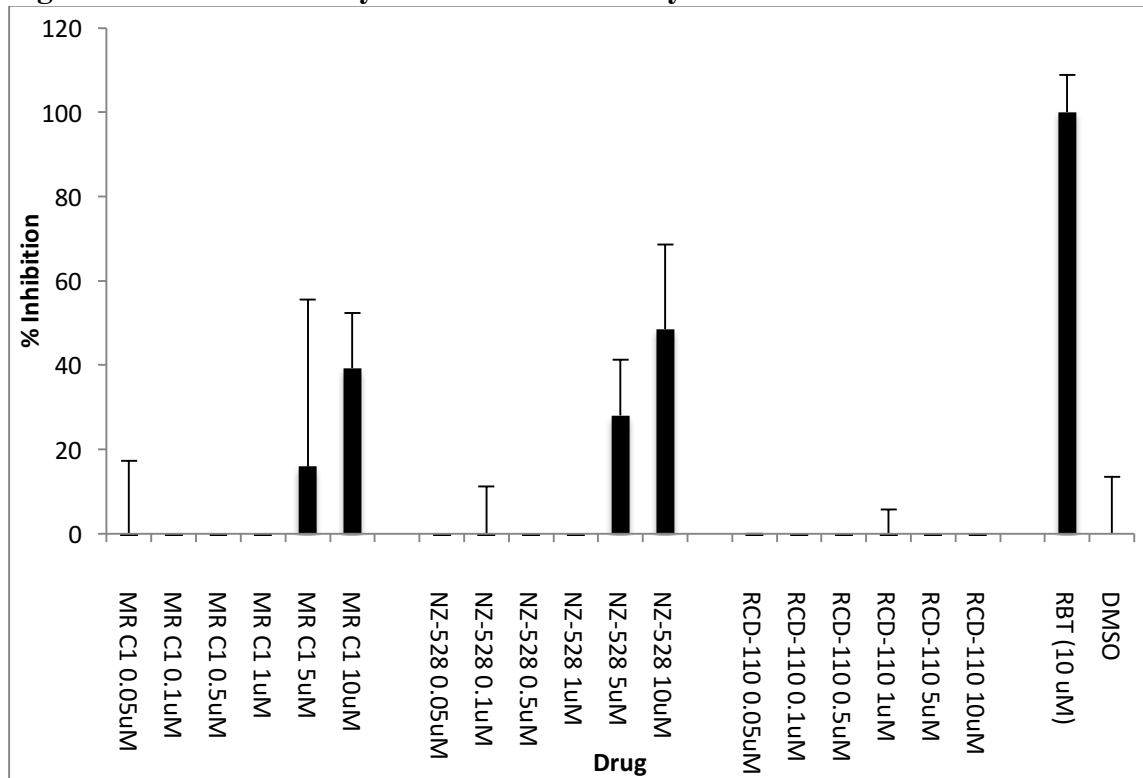
Variability was determined for variations of the assay, and for control conditions. The heat map scales are unique to each table as luminescence and fluorescence readings are not directly comparable. (A) A 96-well plate of differentiated THP-1 was infected as described above using the mCherry reporting strain with DMSO only; no positive kill controls were used. The assay showed an average of 24% variability across the wells of the entire plate with no edge specific or positional effects observed. (B) A 96-well plate of differentiated THP-1 was infected as described above using the luciferase reporting strain with DMSO only; no positive kill controls were used. The assay showed an average of 20% variability across the wells of the entire plate with no edge specific or positional effects observed. (C) A 96-well plate of differentiated THP-1 was infected as described above using the luciferase reporting strain but with drugs in triplicate at a variety of inhibition levels and good range of signal. Wells with lower levels of inhibition correlate with higher amounts of variability.

Figure IV-6: Optimizing Exposure Length.



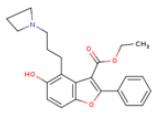
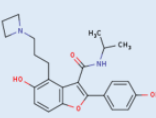
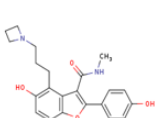
To ensure that sufficient incubation time of *Mtb* with compound occurs, biological triplicate readings at 3,4, and 5 days post-infection were compared. Error bars represent 1 standard deviation. For the range of known anti-tubercular compounds tested, readings can be taken on any of those 3 days and produce quality data.

Figure IV-7: The Necessity of Intermediate Assays.



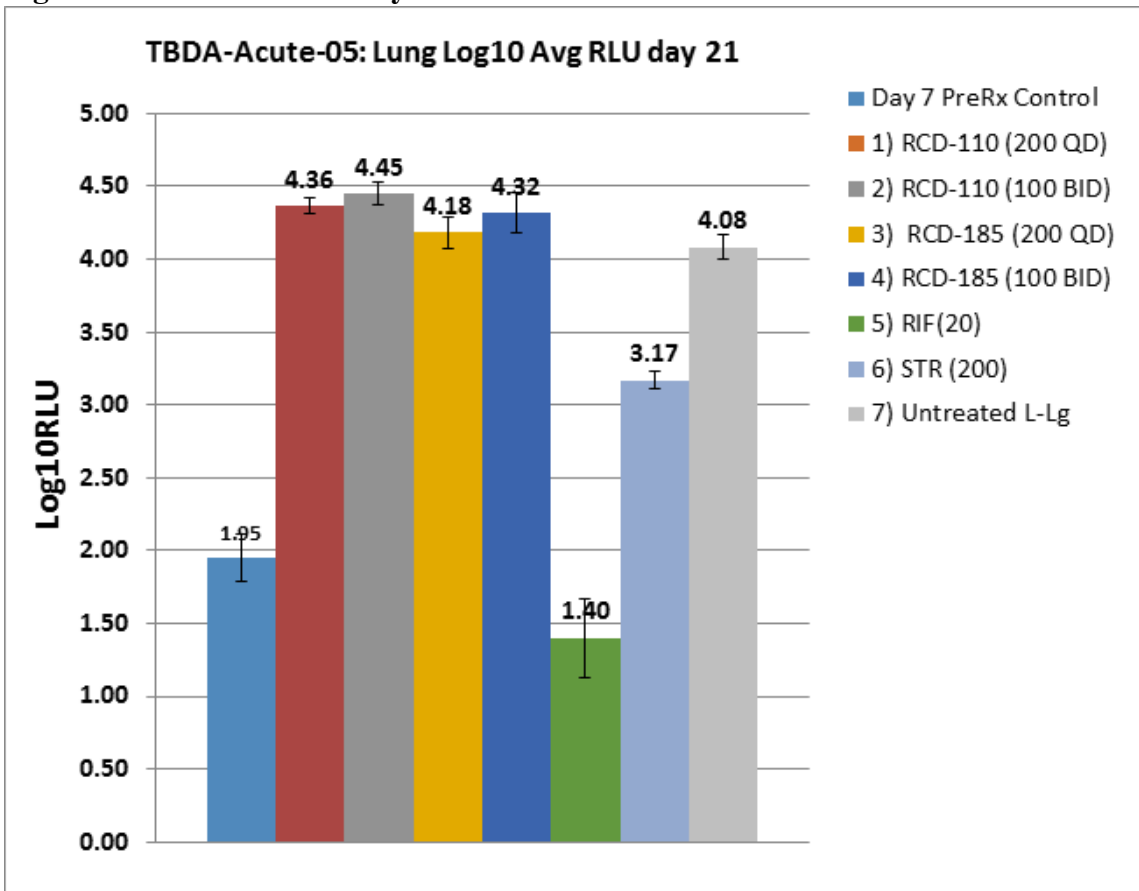
Some research is conducted from screening in liquid culture to *in vivo* testing without an intermediate infected macrophage assay. This assay showed that none of the test compounds exhibited efficacy, especially RCD-110. Standard triplicate THP-1 infected with luciferase reporting Mc²-7000 was used with data collected day 4 post infection. Error bars represent 1 standard deviation.

Figure IV-8: Compound Series Evaluation.

PKS-13 ID	Structure	MIC50 (μM)	IC50 (μM)	Fibroblast Cytotox (IC50) (uM)	THP1 MIC % Inhibition At 10 uM	hERG CHO Human Thallium Influx IC50 (uM)	TAMU PK AUC = ng*min/mL	DDU PK AUC = ng*min/mL	Plasma Stability (Mouse and Human)	MCLint, HCLint (mL/min/g liver)	Kinetic Sol.	Plasma Protein Binding in Mouse/ Human %
RCD-110		0.0018	0.5	10.6	0	18	AUC _{0-24hrs} = 59,880 ng*min/mL C _{500nM} = 100 ng/mL T _{1/2beta} = 30 min.	AUC _{0-24hrs} = 212,878 ng*min/mL C _{500nM} = 485 ng/mL T _{1/2beta} = 4 hours		MLM = 5.2 TAMU MLM = 9.1	103.1 μM	94
RCD-241		0.013	> 10	> 100	43 14% StD.	> 30 Qpatch	AUC _{0-24hrs} = 0.0 ng*min/mL C _{500nM} = 0 ng/mL T _{1/2beta} = N/A Not Detected	Being sent to DDU		MLM = 2 HLM = 4.5	88.4 μM	86
RCD-185		0.0157	1.6	> 100	69 15% StD.	> 30 Qpatch	AUC _{0-24hrs} = 5,160 ng*min/mL C _{500nM} = 58 ng/mL T _{1/2beta} = 1 hour	AUC _{0-24hrs} = 55,042 ng*min/mL C _{500nM} = 241 ng/mL T _{1/2beta} = 1 hrs.		MLM = 1.2 HLM = 0.8 TAMU MLM = 3.2	Testing	54.9

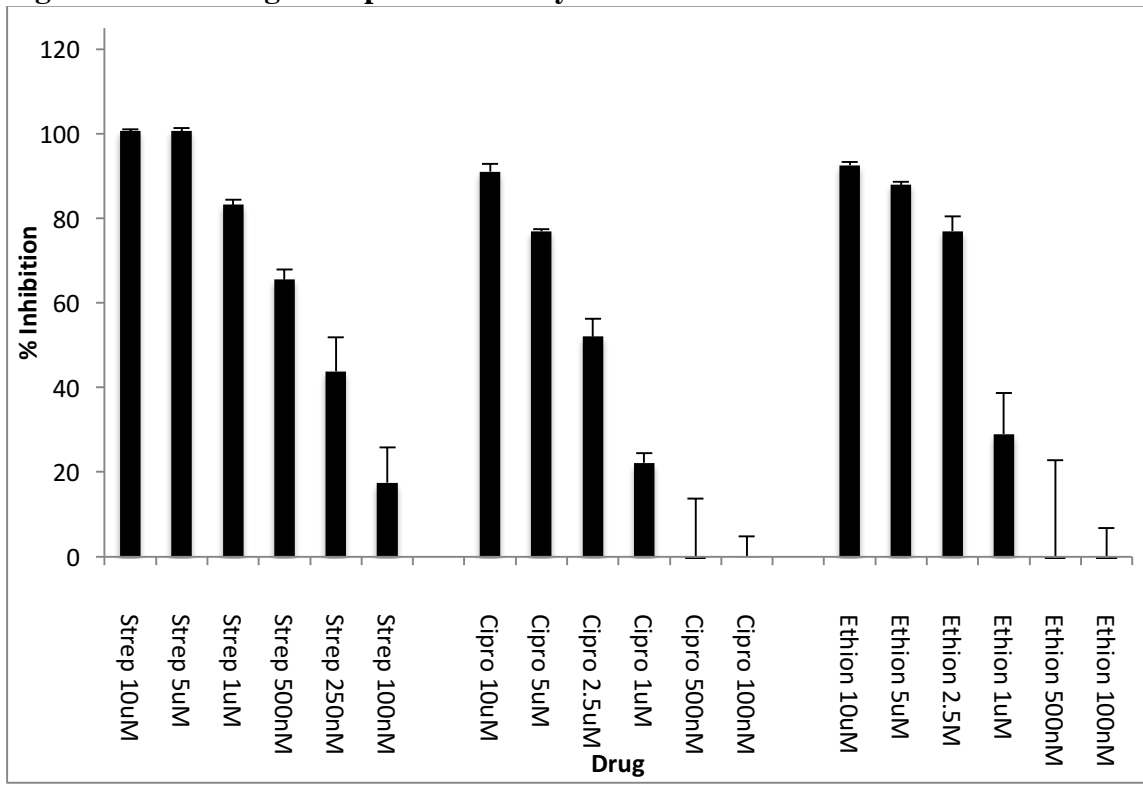
Prior to proceeding to *in vivo* testing, the top compounds are evaluated on a variety of parameters to see which merit further testing. By all parameters, other than macrophage assay results, RCD-110 looked to be a promising therapy.

Figure IV-9: Murine Efficacy.



RLU luminometry data from the BALB/c acute study performed with RCD-110/185. Neither RCD-110 or RCD-185 showed no efficacy in a murine infection model. Data from Greg Robertson at CSU.

Figure IV-10: Using the Optimized Assay.



Improvements in the quality of data from the macrophage infection model are quantitative and reliable in identifying candidates likely to show *in vivo* efficacy. Error bars represent 1 standard deviation. Performed in triplicate using the standard luciferase protocol described previously.

CHAPTER V

CONCLUSIONS

Using the Appropriate Model to Determine Efficacy in Combination Cancer Therapies

In the drug design setting, a project may begin with a compound, a target, or both. In this dissertation two main types of therapies were utilized. Two therapies were used for treating human genetic malfunctions, Menkes disease and cancer, while the other was designed to test the efficacy of compounds used for clearing infection from a pathogen. Regarding human disease genetics, the projects here represent a hereditary disease, Menkes, as well as an acquired cellular malfunction, cancer. Menkes reflects a very specific cause and symptom. Cancer is a broad disease category and treatments get more complex and diverse as technology such as whole genome sequencing and RNA-sequencing become more available and understanding of the disease increases.

For development of the RTI-79 project, it was chosen to broadly go after aggressive drug resistant cancers with poor prognosis and a lack of therapy options. This work focuses on RT therapies as part of a bigger project that also examines traditional chemotherapies. The project evolved with the results of the initial high throughput screens. On one hand, it is a luxury to be able to conduct such large screens, but it is highly unlikely that the RTI compound series would have been designed if it was not for the data obtained by screening resistant lymphoma (G3) with the standard of care therapy it is resistant to combined with a 50,000 compound library. The SAR performed by the medicinal chemists was crucial to developing rifabutin analogs, including RTI-79.

The addition of combination treatment with RT and RTI-79 is positive in that it opened up the general applicability across cancer therapies in combination with RTI-79. By showing that RT can have synergy with RTI-79 the way some ROS producing chemotherapies do is informative towards the mechanism of action (MoA). Additionally, RTI-79 proved to work well in fractionated therapy, and shows that this drug is relevant, functioning in concert with the appropriate standard of care.

While animal trials with chemotherapy continue, the biology should continue to be probed to understand the cancers and conditions in which RTI-79 is effective and how to predict efficacy for a patient. qRT-PCR indicates fluctuating levels of antioxidant response element (ARE) transcripts and RNA-Sequencing should be revisited for a deeper biological understanding. In this situation where the cells are under stress and potentially triggering death, the typically cycling of relevant proteins may be a poor representation of the cells under stress. Proteomics combined with RNA-Sequencing overcomes this limitation.

The model used to perform these tests was tissue culture. Xenograft mouse models and spontaneous canine models will both be used as a precursor to getting into human clinical trials. While canine models are more applicable to humans than mice, a primate model is the closest *in vivo* model to replicate human biology. The fact that RTI-79 has broad activity against many cancers will require some induced and other laboratory generated tumors to be able to gather data on the most effective anticancer application to further develop this new drug.

Advancing Drug Discovery to Mammalian Models

Menkes disease is unique from cancer in that it is hereditary and x-linked, only affecting males (female carriers have mild fur phenotypes). Therapy is also constrained by a typical lifespan of 14 days for affected males. The presentation of Menkes provides for very clear data, in that effective treatment extends life past 2 weeks, in this case to months, possibly a normal life (despite pigmentation abnormalities that seem purely superficial). Unfortunately, effective recovery of systemic copper transport requires a more complex model to be tested. That complex model happens to be roughly 25% of the pups born to a carrier mother. Affected males don't make it to puberty and so a homozygous affected female is not produced.

With Menkes, the problem and likely solution were both identified prior to designing the ultimately effective therapy schedule. The newborn mice had improper and lethal copper trafficking and sequestration. The question was if ES-Cu²⁺ could rescue copper homeostasis in newborn pups. Once it was determined ES-Cu²⁺ did, the dosing schedule and concentration was optimized. While the therapy developed in this project is leaps and bounds above the previous standard of care for Menkes, His-Cu²⁺. Human clinical trials with unfortunate children who are born with Menkes would be next, with a slow titration necessary. Too high of a dose would be lethal, and supports using non-human primates, or another higher order mammal for a safety study.

Currently, all mothers are not screened for all genetic diseases. A mother who had previously conceived a child with Menkes would know it was possible again with future pregnancies. While the treatment we have established is amazing in its ability to provide

affected males with a normal life, I truly see it as a stop-gap measure. Current technology for DNA based screening for genealogy and health are increasing in use and breadth while the cost is plummeting. The next step will be to know a child is going to have Menkes prior to birth and the appropriate therapy based on our findings could be delivered. Ultimately gene editing will correct *ATP7A* in the embryo so that a healthy child with no need for treatment is born.

Using Tissue Culture as a Surrogate for Animal Infection Models

When initially characterizing a disease, or when testing novel therapies, the right complexity of model is required. The most appropriate model will need to produce the required data with the simplest approach. When screening for synergy in G3 cells, it does not make sense to conduct a large screen such as that on animals. In fact, it would be detrimental to getting that data in terms of time and cost. The unnecessary use of animals is not only counterproductive in this example, but it is also unethical to unnecessarily use animals, especially when the end point is terminal and testing chemotherapies would be painful in and of itself.

The macrophage assay is the perfect example of being able to use modern technology to minimize the use of animals. It must be an effective, comparable assay to warrant switching from an animal model. Ultimately, compounds tested in the macrophage assay may continue on to be tested in animals, the next step. A pro-drug such as PA-824 cannot be tested on TB in culture alone, but will work in a human intracellular model. TB infected mice can be partitioned during dissection for localized analysis, but

manipulation of an intracellular environment can be collected with much less noise, from tissue culture. It is also much simpler to treat cells instead of mice.

For research within the United States, American Type Culture Collection (ATCC) and a host of animal providers and contract research organizations (CROs) can provide almost any tissue, cells, or animal model requested. Depending on the extent to which animals will be needed, it may be significantly less expensive and require the use of many fewer animals by ordering them as opposed to maintaining an individual colony. In the case of Menkes mice, the treatment regimen required that a local colony be used so that treatment could start soon after birth without acclimatization needs. The pups also need their mother and the stress of trying to move them together would likely result in the mother abandoning, at best, her progeny.

In Conclusion

As exhibited by this body of work, animals are not the silver bullet for disease treatment research. The macrophage assay is not in lieu of animal studies, but a precursor to prevent predictable failures. Animal models are able to identify potential pitfalls in a proposed therapy that are not realized by using a non-*in vivo* model. When it comes to cancer, the majority of research can be done using tissue culture, with a human cell being the smallest self-contained unit of that disease. With the systemic trafficking deficiency of Menkes, a mouse model was the simplest model at this time. Theoretically an independent intestinal model could be developed to at least test for rescue of the intestinal sequestration phenotype.

Ultimately many human disease therapies will be tested on animals. As technology advances, specifically 3D culturing and *in vitro* organs, animal use will be reduced. An ethical balance has been achieved between curing human disease and the use of animals in research. As technology permits, the use of animals should naturally decrease. The presence of community members on animal welfare boards helps make sure that animal use is justified. So long as technology, in regards to biological research, continues to increase, we are headed to a future where the primary use of animals in research will be to understand the animals and not as a safety screen for humans.